elektronisches dokument
ULB Sachsen-Anhalt

High wave vector spin waves in ultrathin Fe films on W(110) studied by spin-polarized electron energy loss spectroscopy

Dissertation

zur Erlangung des akademischen Grades

doctor rerum naturalium
(Dr. rer. nat.)
genehmigt durch

Martin-Luther-Universität
Halle-Wittenberg

vorgelegt von
Herrn Yu Zhang
geboren am 14.11.1977 in Hebei, China

Gutachter:

1. Prof. Dr. J. Kirschner
2. Prof. Dr. H. J. Elmers
3. Prof. Dr. W. Widdra

Halle (Saale), 02. 2009

Verteidigungsdatum: 15. 07. 2008

urn:nbn:de:gbv:3-000015313
[http://nbn-resolving.de/urn/resolver.pl?urn=nbn%3Ade%3Agbv%3A3-000015313]

Abstract

The high wave vector spin waves in the ultrathin Fe films on W(110) are studied using the spin-polarized electron energy loss spectroscopy (SPEELS). The spin waves are probed along the [001] direction with the in-plane wave vector from 0.3 $Å^{-1}$ to 1.1 $Å^{-1}$. For the 2 monolayers (ML) Fe film measured at room temperature, the spin waves reveal a clear dispersion relation. The spin wave energy reaches to about 170 meV at the Brillouin zone boundary. The SPEEL-spectra for the Fe films between 1 ML and 2 ML demonstrate that the observed spin waves are mainly excited in the double layer regions. For the 1 ML Fe/W(110), the SPEELS measurements are performed at 120 K. The magnetic excitations reveal the lower energy in the range from 20 meV to 60 meV. The SPEELS measurements are also performed for the thicker Fe films (up to 24 ML). The evolution of the spin wave excitations as function of the Fe film thickness is observed.

The spin wave dispersions in the Fe films are discussed within the Heisenberg model. The obtained exchange parameters for 1 ML and 2 ML Fe/W(110) are in good agreement with the results from the existing studies of the magnetic domain walls. From the intensity distribution of the spin waves in the SPEEL-spectra, the lifetime and spatial distribution of the spin waves in 2 ML Fe/W(110) are estimated. The experimental results are also compared with the calculations based on the itinerant electron theory. The thickness dependence of the spin wave stiffness show good agreement with the theoretical calculations. The explanation of spin wave peaks observed for the thick Fe films is proposed based on the comparison between the experimental data and the calculations.

Contents

1 Introduction **1**

2 Magnetic excitations **3**
2.1 Spin waves in the Heisenberg model 3
2.2 Magnetic excitations in the itinerant electron system 11
2.2.1 Stoner excitations 11
2.2.2 Relation between spin waves and Stoner excitations 12
2.3 Experimental techniques in spin wave study 14

3 SPEELS and experimental details **19**
3.1 Ultra high vacuum system 19
3.2 SPEELS 19
3.2.1 Inelastic scattering of electrons 20
3.2.2 SPEEL-spectrometer 23
3.2.3 GaAs photocathode 25
3.2.4 SPEELS measurements 26
3.3 Ultra thin Fe films on W(110) 29
3.3.1 Structure and magnetic properties 30
3.3.2 Preparation and characterization 32

4 Results **37**
4.1 SPEELS measurements for 2 ML Fe/W(110) 37
4.2 SPEEL-spectra for Fe films between 1 ML and 2 ML 43
4.3 SPEELS measurements for 1 ML Fe/W(110) at 120K 46
4.4 Evolution of the SPEEL-spectra for thicker Fe films 47

5 Discussion **53**
5.1 Spin wave dispersions discussed in the Heisenberg model 53
5.1.1 Spin waves in 2 ML Fe/W(110) 53
5.1.2 Spin wave dispersion in 1 ML Fe/W(110) 56
5.1.3 Comparison of the spin wave dispersions in thin films and bulk . 57
5.2 Properties of spin waves in Fe thin films 59
5.3 Comparison between the SPEELS results and calculations 63
5.3.1 Thickness dependence of spin wave stiffness 63
5.3.2 Spin waves in 1 ML Fe/W(110) 64
5.3.3 SPEEL-spectra of 2 ML Fe/W(110) 66

5.3.4 SPEEL-spectra of thicker Fe films 68

6 Conclusions and outlook **73**

Chapter 1

Introduction

Spin waves are of fundamental importance for the understanding of magnetism. Spin waves of high wave vector are dominated by the exchange interaction between the electrons, which is responsible for the spontaneous magnetic order in the nature. In ferromagnetic 3d metals, the description of magnetic excitations is complicated due to the itinerant electron character of these systems. The study of spin waves in such systems will check and improve present spin wave theories, which may in turn help for better understanding of the spin correlation in itinerant electron systems. In the case of low dimensional magnetic systems, magnetic excitations are expected to show different behaviors from those in bulk, and the understanding of the spin wave excitations in thin films is still far from complete.

An ideal system for the study of spin waves is an ultra thin film grown on a single crystal substrate. The epitaxial thin films reveal high purity and nearly perfect crystallographic structure. The spin-polarized electron energy loss spectroscopy (SPEELS) has shown its extraordinary ability in studying spin waves [1, 2] in such a system. In comparison to the inelastic neutron scattering experiments, which are used for probing spin waves in bulk materials, the SPEELS reveals high surface sensitivity and is more suitable for the study of spin waves in the thin films. As compared to the other established surface sensitive methods, such as ferromagnetic resonance and Brillouin light scattering, the SPEELS enables the measurements of high wave vector spin waves up to the Brillouin zone boundary, where the influence of the itinerant electron system to spin waves can be studied.

In the study of magnetic ultra thin films, Fe film on W(110) surface is one of the most extensively studied systems. Various advanced experimental techniques have been applied to study the magnetic properties, structure, film stress and electronic band structure of the Fe films, These techniques include conversion-electron Mössbauer spectroscopy [3, 4], torsion oscillation magnetometry [5], Brillouin light scattering [6], scanning tunneling microscopy [7–15], cantilever methods [16, 17], surface X-Ray diffraction [18, 19], angle-resolved photoelectron spectroscopy [20–22] and so on.

The SPEELS study was also performed on this system by Kirschner *et al.* [1], which for the first time demonstrated the ability of the SPEELS in the study of spin waves. Following the spin wave signature found in Ref. [1], successive studies of spin waves in the Fe thin films [23, 24] have been performed. The excitations appeared as broad peaks at low energies without showing the characteristic dispersion, which is not clearly

understood.

In this work, the spin waves in the ultrathin Fe films grown on W(110) are studied for different film thicknesses. For the first time, the well defined spin wave excitations with a clear dispersion relation are observed for 2 ML Fe/W(110) [25]. The obtained dispersion is discussed in the Heisenberg model and compared with the theory [26]. The properties of spin waves, such as lifetime and spatial distribution, are estimated from the SPEEL-spectra. At low temperature, magnetic excitations are also found in the single monolayer Fe film on W(110), which behave as strongly damped spin waves. For the thicker films, the spin waves also show similar broad peaks as has been observed in the previous studies [24]. Nevertheless, the excitations can be obtained with more details and will be compared with the present spin wave theories for this system [27].

This work is organized as follows. The classical description of the spin waves and Stoner excitations are briefly introduced in Chapter 2. In Chapter 3 the construction and operation of the SPEEL-spectrometer and sample preparation are described. The experimental results are presented in Chapter 4 and then discussed in Chapter 5 based on the Heisenberg model and other theoretical calculations [26–29]. Finally, the conclusions and an outlook are given in Chapter 6.

Chapter 2

Magnetic excitations

The concepts of magnetic excitations in a magnetic ordered system are introduced in this chapter. We distinguish two kinds of magnetic excitations: the spin wave excitation and Stoner excitation. The former is of the collective character and will be discussed in the Heisenberg model. The Stoner excitation, which is the spin-dependent single particle excitation, is explained within a simple electronic band structure. The relation between the spin waves and Stoner excitations is then discussed in the itinerant electron system. The theoretical works on the spin waves for the Fe thin films are also introduced. Finally, the experimental techniques for the measurements of spin waves will be briefly reviewed, as well as the experimental results concer0ning the high wave vector spin waves for both bulk Fe and Fe thin films.

2.1 Spin waves in the Heisenberg model

Spin waves are collective magnetic excitations. They can be described in two different pictures: the classical Heisenberg model based on the localized moment approximation and the itinerant electron model [30]. This section will be focused on the description of the spin waves in the classical Heisenberg model, which gives an intuitive picture of spin waves. The theoretical studies based on the itinerant electron model will be introduced in Sec. 2.2.

In the Heisenberg model, spin waves are treated as the synchronic precession of the spin vectors in the magnetic ordered system. The waveform results from the constant phase difference between the spins. This is schematically shown in Fig. 2.1, where the spin wave is formed by the precessing spins with a constant phase difference between the nearest neighbors. The dispersion relation can be obtained in a classical analogy, which describes the spin wave energy as a function of wave vector. Similar to the other quasi-particles, such as phonons and plasmons, spin waves are quantized [31], and the quanta of spin waves are called magnons. A magnon carries the angular momentum of 1 $\hbar$ and the magnetic moment of 1 gμ_B, which corresponds to a spin flip in the crystal. Due to the integer spin number Magnons are indentified as Bosons .

The wave vector of the spin waves studied in this work is typically from 0.3 Å^{-1} to 1.1 Å^{-1}, which corresponds to the wavelength from 6 Å to 20 Å. For the spin waves with such wavelengths, their energies are dominated by the exchange interaction. The magnetostatic dipolar interaction and magnetic anisotropy energy (MAE) can be

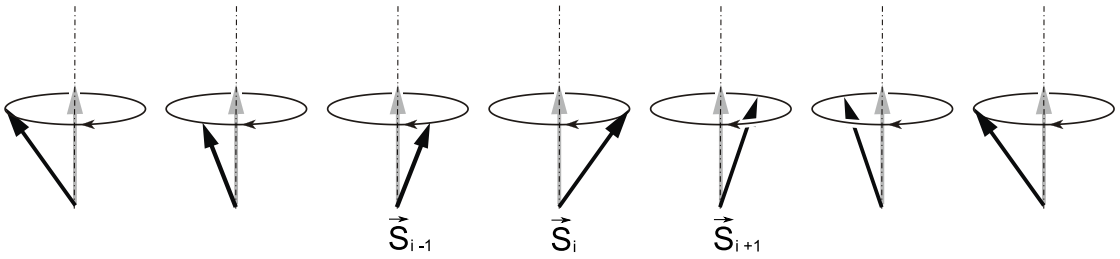

Figure 2.1: The classical picture of spin wave in a 1 dimensional spin chain. The black arrow denotes the spin directions of each individual atom. The propagation of spin wave is from left to right.

neglected [32]. For instance, the energies of the dipolar interaction and MAE in the Fe thin films are about the order of 0.1 meV/atom [33]. This is nearly two orders of magnitude smaller than the exchange energy between the nearest Fe atomic neighbors as shown in Tab. 2.1.

Exchange interaction results from the Pauli principle and the assumption that the electrons with the same spin are identical particles, which require that the total wave function of a many-electron system must be antisymmetric in the case of the exchange of two electrons. The total wave function of electrons can be written as the product of the spatial part and spin part. For a two-electron system, the parallel or antiparallel of the spins of two electrons corresponds to the symmetric or antisymmetric spin wave function, which demands that the spatial one has to be antisymmetric or symmetric accordingly to keep the antisymmetry of the total wave function. The spatial wave functions with different symmetries give rise to the different spatial distributions of the electrons and consequently, different electrostatic energies due to the Coulomb interaction. The energy due to the exchange interaction can be described using the Heisenberg Hamiltonian [34]:

$$\mathrm{H} = -\sum_{\mathrm{ij}} \mathrm{J_{ij}} \vec{\mathrm{S}}_\mathrm{i} \cdot \vec{\mathrm{S}}_\mathrm{j}, \tag{2.1}$$

in which $\mathrm{J_{ij}}$ is the exchange coupling constant between two spins $\vec{\mathrm{S}}_\mathrm{i}$ and $\vec{\mathrm{S}}_\mathrm{j}$. The positive $\mathrm{J_{ij}}$ corresponds to the ferromagnetic coupling.

Originating from the exchange of the electrons, the exchange interaction is determined by the overlap of the wave functions for the electrons in two lattice sites. For the 3d transition metals, the d electrons are relatively localized [34], and the overlap of the wave functions decays very fast with the increase of the distance between two lattice sites. Therefore, the exchange interactions between these electrons are short-ranged. In many cases, one may only consider the exchange interaction between the nearest neighbors, which gives a good description of the magnetic excitations in the system [34]. Table. 2.1 shows the effective exchange constants JS^2 and the spin wave stiffness coefficients calculated for Fe, Co and Ni based on the adiabatic approximation [35]. For Co and Ni, the exchange interaction between the nearest neighbors is the dominating contribution, for which the nearest neighbor approximation is often applied. However,

Table 2.1: Listed are the Heisenberg exchange coupling constants for the nearest, next nearest and third nearest neighbors ($J_N S^2$, $J_{NN} S^2$ and $J_{3rd} S^2$) in bulk Fe, Co and Ni, as well as the spin wave stiffness D for these systems calculated in [35].

	Fe(bcc)	Co(fcc)	Ni(fcc)
$J_N S^2$(meV)	19.5	14.8	2.8
$J_{NN} S^2$(meV)	11.1	1.5	0.1
$J_{3rd} S^2$(meV)	-0.2	1.6	0.4
D(meV Å^2)	250±7	663±6	756±29

in the case of bcc Fe, the exchange interactions between the next nearest neighbors are still significantly large, which can not be neglected. This will be considered in the later discussion of the spin wave dispersion described in the Heisenberg model.

In the following, the spins are treated as classical vectors to derive the spin wave dispersion relation in the Heisenberg Hamiltonian (Eq. 2.1). This classical approach gives the same result as the quantum mechanical description [36]. Here, we only consider the spin moment, and the orbital moment is assumed to be quenched in the crystal [31]. Each atom thus carries the magnetic moment $\vec{\mu}_i = -g\mu_B \vec{S}_i$. It is known that the energy of the magnetic moment $\vec{\mu}_i$ in a magnetic field $\vec{B}$ is given by $-\vec{\mu}_i \cdot \vec{B}$. Similarly, the exchange coupling induced by the neighbors can be taken as an effective field $\vec{B}_i^{effect}$ according to Eq.2.1, which gives

$$\vec{B}_i^{effect} = -\frac{2}{g\mu_B} \sum_j J_j \vec{S}_j. \tag{2.2}$$

The factor 2 comes from the fact that the sum for each pair of neighbors is calculated twice in Eq.2.1. In the effective field the spin $\vec{S}_i$ experiences a torque $\vec{\tau}_i = \vec{\mu}_i \times \vec{B}_i^{effect}$, which make the spin precess. The time dependence of the angular momentum $\hbar\vec{S}$ follows

$$\hbar \frac{d\vec{S}_i}{dt} = \vec{\tau}_i = 2 \sum_j J_j (\vec{S}_i \times \vec{S}_j). \tag{2.3}$$

The mathematical description of spin precession can be obtained by solving Eq. 2.3. The z direction is defined as the spin direction in the ground state. The expansion of the cross product in Eq. 2.3 can be expressed as

$$\hbar \frac{dS_i^x}{dt} = 2 \sum_j J_j (S_i^y S_j^z - S_j^y S_i^z), \tag{2.4}$$

and

$$\hbar \frac{dS_i^y}{dt} = 2 \sum_j J_j (S_j^x S_i^z - S_i^x S_j^z). \tag{2.5}$$

Assuming that the deviations of the spins in the excited state are very small as compared to the value of $\vec{S}_i$, S_i^z and S_j^z are approximated to be S, the value of the spin moment $\vec{S}_i$. Multiplying Eq. 2.5 by i and adding it to Eq. 2.4, we obtain

$$i\hbar \frac{dS_i^+}{dt} = 2S \sum_j J_j (S_i^+ - S_j^+), \tag{2.6}$$

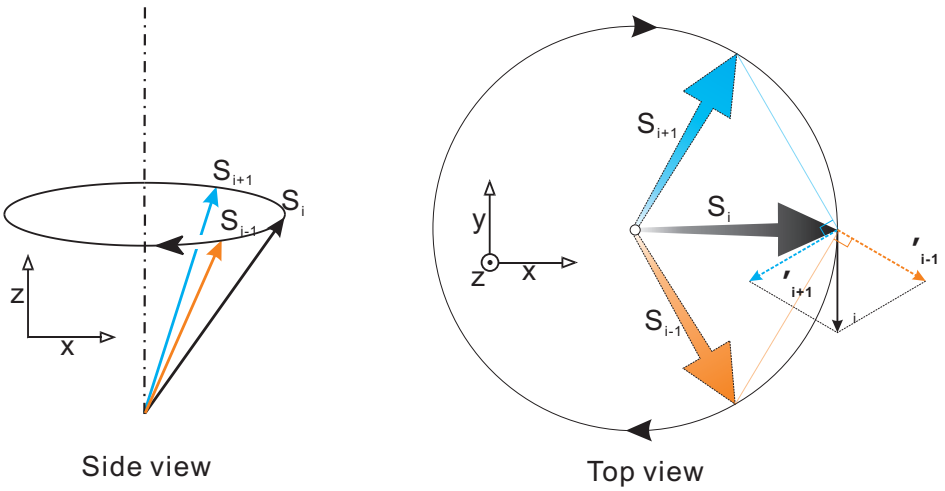

Figure 2.2: The spins $\vec{S}_i$, $\vec{S}_{i-1}$ and $\vec{S}_{i+1}$ in Fig. 2.1 are superimposed and shown in the side view and top view, respectively. The torques experienced by the center spin $\vec{S}_i$ from the neighbors $\vec{S}_{i-1}$ and $\vec{S}_{i+1}$ are denoted as $\vec{\tau}'_{i-1}$ and $\vec{\tau}'_{i+1}$. The total torque on $\vec{S}_i$ is $\vec{\tau}_i$, which is tangent to the circle and causes the precession of spin $\vec{S}_i$.

in which the substitution $S^+ = S^x + iS^y$ is used [31]. Eq. 2.6 describes the motion of each spin $\vec{S}_i$ in the Heisenberg Hamiltonian.

The precession of spins is schematically illustrated in Fig. 2.2, where the three adjacent spins in Fig. 2.1 are superimposed. The z-axis is parallel to the magnetization direction. Due to the exchange interaction, spin $\vec{S}_i$ prefers to be parallel to both $\vec{S}_{i-1}$ and $\vec{S}_{i+1}$. The torques induced by the effective field $\vec{B}_i^{\text{effect}}$ are $\vec{\tau}'_{i-1}$ and $\vec{\tau}'_{i+1}$, respectively. The total torque $\vec{\tau}_i$ is pointing clockwise along the tangent of the circular trajectory. Forced by $\vec{\tau}_i$, $\vec{S}_i$ precesses clockwise with respect to the z direction. Similar to $\vec{S}_i$, other spins also precess with respect to the z direction, but with a phase difference between the two neighboring spins. Consequently, spin wave is formed in the spin chain as shown in Fig. 2.1.

For an infinite slab, Eq. 2.6 can be solved by using the ansatz $S^+ = A_i \exp(i(\vec{Q}_{||}\vec{R}_i - \omega t))$, in which $\vec{Q}_{||}$ and ω denote the in-plane wave vector and frequency of spin waves, respectively. A_i is the amplitude of the spin wave at the position $\vec{R}_i$. Substituting the ansatz expression and dividing both sides of Eq. 2.6 by $\exp(i(\vec{Q}_{||}\vec{R}_i - \omega t))$, one gets

$$\hbar\omega A_i = \sum_j 2J_j S(A_i - A_j e^{i(\vec{Q}_{||}\cdot(\vec{R}_j - \vec{R}_i))}). \tag{2.7}$$

The spin wave dispersion can be derived from Eq. 2.7. As an example, a two-atomic-layer film with the bcc(110) structure is calculated in the Heisenberg model based on the nearest neighbor approximation (NNH). The in-plane wave vector $\vec{Q}_{||}$ is along the [001] direction. This is illustrated in Fig. 2.3 (a), where the centered atom and its 6 nearest neighbors exhibit a bcc(110) structure. The expressions given in the boxes are the exchange contributions from the neighboring atoms, which are summed up in Eq. 2.7. J_N is the exchange constant between the two nearest neighbors. A_1 and A_2 are

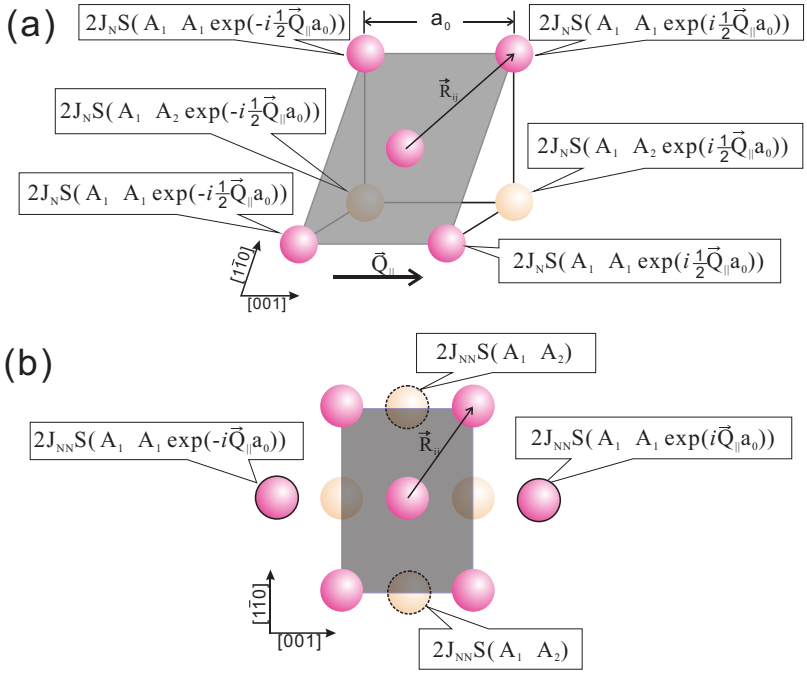

Figure 2.3: The illustration of Eq. 2.7 for a two-atomic-layer film with bcc (110) surface. The red and yellow balls represent the atoms in the first and second layers, respectively. The shadowed plane indicates the surface unit cell. The in-plane wave vector of spin wave, $\vec{Q}_{||}$, is along the [001] direction. $\vec{R}_{ij}$ is the position vector of the neighboring atoms. In Eq. 2.7, the terms related to the exchange interaction between the atomic neighbors are shown in (a) for the nearest neighbors and in (b) for the next nearest neighbors.

the spin wave amplitudes in the first and second atomic layers. After the summation of the six terms in Fig. 2.3, one gets the expression as

$$\hbar\omega A_1 = 4J_NS[3 - 2\cos(\frac{1}{2}\vec{Q}_{||}a_0)]A_1 - 4J_NS\cos(\frac{1}{2}\vec{Q}_{||}a_0)A_2 \tag{2.8}$$

for the first atomic layer from Eq. 2.7. Similarly, for the second layer it is

$$\hbar\omega A_2 = -4J_NS\cos(\frac{1}{2}\vec{Q}_{||}a_0)A_1 + 4J_NS[3 - 2\cos(\frac{1}{2}\vec{Q}_{||}a_0)]A_2. \tag{2.9}$$

Eq. 2.8 and Eq. 2.9 can be combined and rewritten as

$$\hbar\omega \begin{pmatrix} A_1 \\ A_2 \end{pmatrix} = \begin{pmatrix} 4J_NS[3 - 2\cos(\frac{1}{2}\vec{Q}_{||}a_0)] & -4J_NS\cos(\frac{1}{2}\vec{Q}_{||}a_0) \\ -4J_NS\cos(\frac{1}{2}\vec{Q}_{||}a_0) & 4J_NS[3 - 2\cos(\frac{1}{2}\vec{Q}_{||}a_0)] \end{pmatrix} \begin{pmatrix} A_1 \\ A_2 \end{pmatrix}. \tag{2.10}$$

In Eq. 2.10, the spin wave energy $\hbar\omega$ can be taken as the eigenvalue of the coefficient matrix on the right side. In this case, the analytical expression for $\hbar\omega$ can be obtained, provided that non-trivial solutions of A_1 and A_2 exist. This requires

$$\begin{vmatrix} -\hbar\omega + 4J_NS[3 - 2\cos(\frac{1}{2}\vec{Q}_{||}a_0)] & -4J_NS\cos(\frac{1}{2}\vec{Q}_{||}a_0) \\ -4J_NS\cos(\frac{1}{2}\vec{Q}_{||}a_0) & -\hbar\omega + 4J_NS[3 - 2\cos(\frac{1}{2}\vec{Q}_{||}a_0)] \end{vmatrix} = 0. \tag{2.11}$$

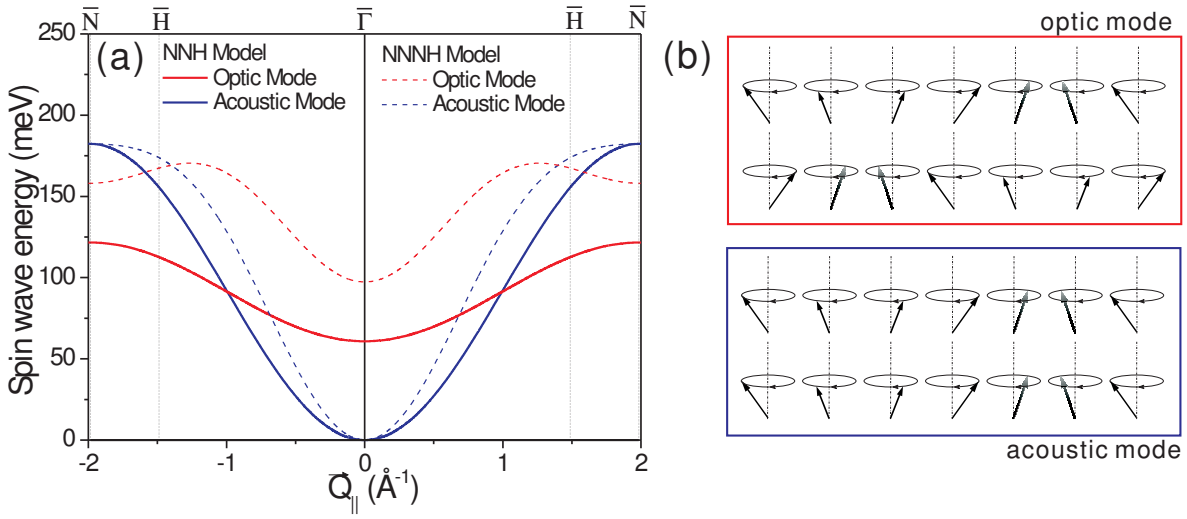

Figure 2.4: (a)The dispersion curves calculated for a two-layer infinite slab of bcc(110) structure in NNH (solid line) and NNNH (dashed line) models. The acoustic and optical modes are shown as blue and red curves, respectively. The solid lines represent the dispersion curves calculated from Eq. 2.12 and Eq. 2.13, and the dashed lines are from Eq. 2.16 and Eq. 2.17. The in-plane wave vector $\vec{Q}_{||}$ is along the [001] direction. As shown in (b) schematically, the precession of the spins in the two layers is in-phase (blue frame) in the acoustic mode and anti-phase (red frame) in the optical modes, respectively.

The solutions of Eq. 2.11 are

$$\hbar\omega = 12\mathrm{J_N S}[1-\cos(\frac{1}{2}\vec{Q}_{||}a_0)] \tag{2.12}$$

and

$$\hbar\omega = 4\mathrm{J_N S}[3-\cos(\frac{1}{2}\vec{Q}_{||}a_0)]. \tag{2.13}$$

They describe the acoustic and optical modes of spin waves in the two-atomic-layer film. The two modes are plotted in Fig. 2.4 (solid lines) for $\mathrm{J_N S}$=7.6 meV and a_0=3.165 Å. By substituting Eq. 2.12 and Eq. 2.13 into Eq. 2.8 and Eq. 2.9, the solutions of A_1 and A_2 can be obtained for the two modes, which show that the spins in the two layers are precessing in-phase in the acoustic mode, and anti-phase in the optical mode. The spin precession in the two modes is schematically illustrated in Fig. 2.4 (b).

As shown in Tab. 2.1, in bcc Fe the exchange interactions between the next nearest neighbors are not negligible. It is necessary to consider the next nearest neighbors for the description of spin waves. Similar to the NNH model, the terms in Eq. 2.7 are summed up for the nearest (Fig. 2.3 (a)) and next nearest neighbors (Fig. 2.3 (b)). The equations for the first and second layers are expressed as

$$\begin{aligned}\hbar\omega A_1 &= 4\mathrm{J_N S}[3-2\cos(\frac{1}{2}\vec{Q}_{||}a_0)]A_1 + 4\mathrm{J_{NN}S}[2-\cos(\vec{Q}_{||}a_0)]A_1 \\ &\quad -4\mathrm{J_N S}\cos(\frac{1}{2}\vec{Q}_{||}a_0)A_2 + 4\mathrm{J_{NN}S}A_2,\end{aligned} \tag{2.14}$$

and

$$\begin{aligned}\hbar\omega A_2 &= -4J_N S\cos(\frac{1}{2}\vec{Q}_{||}a_0)A_1 + 4J_{NN}SA_1 \\ &\quad +4J_N S[3-2\cos(\frac{1}{2}\vec{Q}_{||}a_0)]A_2 + 4J_{NN}S[2-\cos(\vec{Q}_{||}a_0)]A_2. \end{aligned} \quad (2.15)$$

Here J_{NN} is the exchange constant between next nearest neighbors. More terms related to next nearest neighbors are added in comparison to Eq. 2.8 and Eq. 2.9. Eq. 2.14 and Eq. 2.15 are also linear functions of A_1 and A_2. The dispersion relation can be obtained in the same way as used for the NNH model. In the NNNH model, the spin wave dispersions are obtained as

$$\hbar\omega = 12J_N S[1-\cos(\frac{1}{2}\vec{Q}_{||}a_0)] + 4J_{NN}S[1-\cos(\vec{Q}_{||}a_0)] \quad (2.16)$$

and

$$\hbar\omega = 4J_N S[3-\cos(\frac{1}{2}\vec{Q}_{||}a_0)] + 4J_{NN}S[3-\cos(\vec{Q}_{||}a_0)]. \quad (2.17)$$

The two dispersion curves are also plotted as dashed curves in Fig. 2.4 for $J_N S$ = 7.6 meV and $J_{NN}S$ = 4.6 meV. The value of $J_{NN}S$ is set to be 60% of $J_N S$, which is from the ratio for bulk Fe in Tab. 2.1. Due to the exchange interaction from the next nearest neighbors, the acoustic branch is stiffer in the NNNH model than in the NNH model. This is attributed to the additional cosine term $4J_{NN}S[1-\cos(\vec{Q}_{||}a_0)]$ in Eq. 2.16, which has the double frequency as compared to the terms for the nearest neighbors. It can be understood as that the phase difference between the next nearest spins (balls with solid boundary in Fig. 2.3 (b)) is twice as large as that between the nearest ones. For the optical modes, the one in the NNNH model is shifted to higher energy by a constant $8J_{NN}S$ relative to the optical mode in the NNH model in addition to the term $4J_{NN}S[1-\cos(\vec{Q}_{||}a_0)]$. This is due to the exchange interaction of the next nearest neighbors located along the direction perpendicular to the wave vector direction (balls with dashed boundary in Fig. 2.3 (b)), whose spins are always in antiphase to the central spin in the optical mode. However, in the acoustic mode, they are inphase to the central spin and have no contribution to the spin wave energy.

Around the long wavelength limit of the acoustic mode, the dispersion curve can be approximated as a parabola according to the relation, $\lim_{x\to 0}\cos(x) = 1-\frac{1}{2}x^2$. The acoustic mode in the NNNH model (Eq.2.16) can be transformed as

$$\hbar\omega = (1.5J_N + 2J_{NN})Sa_0^2\vec{Q}_{||}^2 = D\vec{Q}_{||}^2, \quad (2.18)$$

where D is the spin wave stiffness coefficient. According to the Bose-Einstein distribution, the thermally excited spin waves are mainly the low energy states at low temperature, which are from the bottom of the acoustic dispersion curve. As the reduction of magnetization can be ascribed to the excitation of spin waves, the temperature dependence of the magnetization reveals the famous $T^{\frac{3}{2}}$ law at low temperature due to the parabolic spin wave dispersion [31].

In the case of a slab with N atomic layers (N>2), N equations can be established for the N layers based on Eq. 2.7. They are linear equations with the variables $A_1 \cdots$

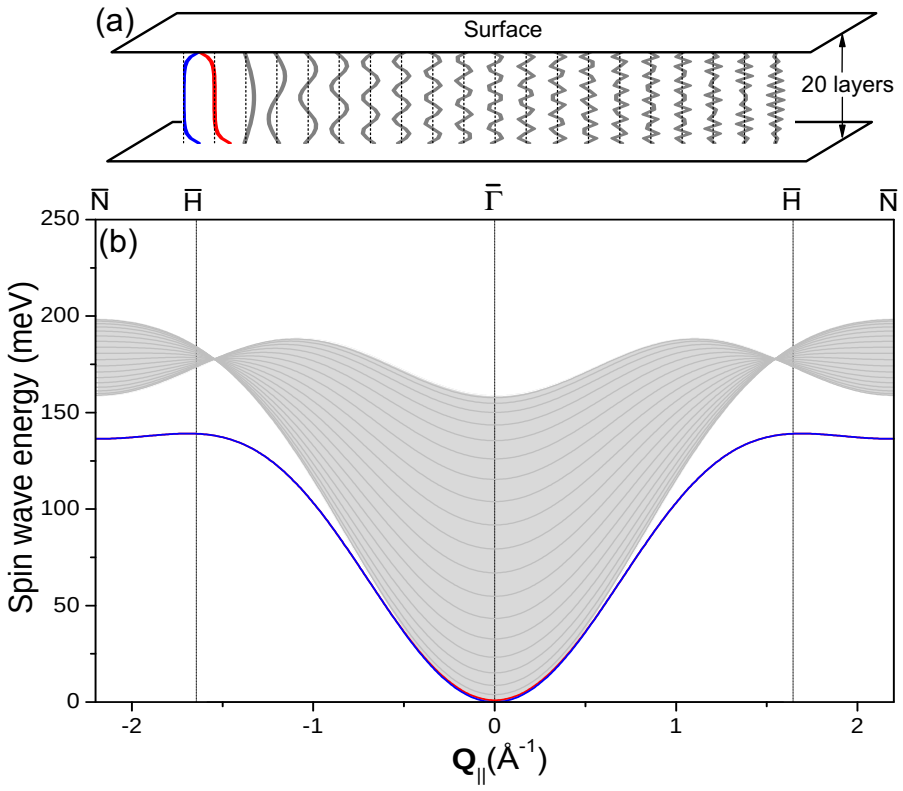

Figure 2.5: The schematic in (a) shows the twenty states of the spin waves with the in-plane wave vector 1 $Å^{-1}$ in a twenty-layer slab. They represent the spin wave amplitudes in each layer. The two states of the surface modes are denoted in blue and red, respectively. (b) shows the calculated spin wave dispersion curves for the twenty-layer slab in the next nearest neighbor Heisenberg model (NNNH). The exchange constants are $J_N S$=6.2 meV and $J_{NN} S$=3.7 meV for the nearest and next nearest neighbors. The lattice constant is a_0=2.866 Å. In the twenty dispersion curves, the two lowest modes in blue and red are the surface modes. The gray region indicates the projection (along the [110] direction) of spin wave band for bulk bcc Fe, which is calculated in the NNNH model with the same exchange parameters.

A_N, which represent the spin wave amplitudes in each layer. Similar to Eq. 2.10, they can be expressed in the form of

$$\hbar\omega \begin{pmatrix} A_1 \\ . \\ . \\ . \\ A_N \end{pmatrix} = \mathbf{M} \begin{pmatrix} A_1 \\ . \\ . \\ . \\ A_N \end{pmatrix}. \tag{2.19}$$

$\mathbf{M}$ is a N×N coefficient matrix for $A_1, \cdots, A_N$. The spin wave energy $\hbar\omega$ is the eigenvalue of the coefficient matrix $\mathbf{M}$. In order to obtain the dispersion relation, the eigenvalues of the matrix $\mathbf{M}$ are numerically calculated for a series of given $\vec{Q}_{||}$. Fig. 2.5 (b) shows the dispersions calculated for a twenty-layer bcc(110) slab using the NNNH model. The in-plane wave vector $\vec{Q}_{||}$ is along the [001] direction. Twenty dispersion curves can be

obtained for this system. The gray region is the projection of the bulk band of the spin waves in the bcc crystal. For any given $\vec{Q}_{||}$, twenty eigenvectors can be obtained associated with the twenty eigenvalues, respectively. Each eigenvector consists of the spin wave amplitudes (A_1, $\cdots$, A_N) in each atomic layer. They reveal the precession amplitudes of the spins in the 20 layers, which are schematically shown in Fig. 2.5 (a) for $\vec{Q}_{||} = 1$ Å^{-1}.

In Fig. 2.5 (a), the eigenvectors in blue and red show high amplitudes at both surfaces, which decay exponentially in the interior of the slab. The dispersion curves related to the two eigenvectors (blue and red dispersion curves in Fig. 2.5 (b)) are evidently out of the the bulk band (gray region) and show relatively lower energies. This indicates that they are the surface modes in the system. The other modes appearing in the gray region are the standing wave modes in bulk, which show quantized wave numbers in the direction perpendicular to the surface [27, 37].

2.2 Magnetic excitations in the itinerant electron system

Spin waves described in the Heisenberg model are not damped. The lifetime of spin waves is infinite at the temperature of zero Kelvin. However, according to the spin wave theory based on the itinerant electron model, spin waves strongly decay into another kind of spin-dependent excitations, the Stoner excitations.

2.2.1 Stoner excitations

In the itinerant electron system, Stoner excitations are the electron-hole pair excitations with electrons and holes in the bands of opposite spins. There are two configurations for the Stoner excitations, which are the majority-hole with minority-electron state and minority-hole with majority-electron state, respectively. The former state is illustrated as the excited state T(Q,E) in Fig. 2.6(a), where a single electronic band structure of a weak ferromagnet is shown with the exchange splitting of U. Similar to the spin wave excitations, this kind of Stoner state corresponds to a spin flip of a majority electron in the system. However, instead of the dispersion relation, the relation of energy E and momentum Q for the Stoner excitations shows a continuum in the energy-momentum space. For the band structure shown in Fig. 2.6(a), the Stoner continuum for the majority-hole, minority-electron states is described by the gray region in Fig. 2.6(b). The gray scale represents the density of the Stoner states. The state T(Q,E) shown in Fig. 2.6(a) corresponds to the green dot in the continuum.

In this simple electronic band structure, the minority band is empty except for the part near the Brillouin zone center, while the majority band is not completely filled. Hence, some of the "majority-hole with minority-electron" states are not available. This produces the region of low intensity in the Stoner continuum. Because the band splitting is uniform over the Brillouin zone, the energy distribution of the Stoner excitations converge to one point at Q=0. This corresponds to the Stoner state with the minority hole locates vertically under the majority electron in Fig. 2.6(a). The energy of these states is equal to the band splitting U. In reality, however, the band structures in $3d$

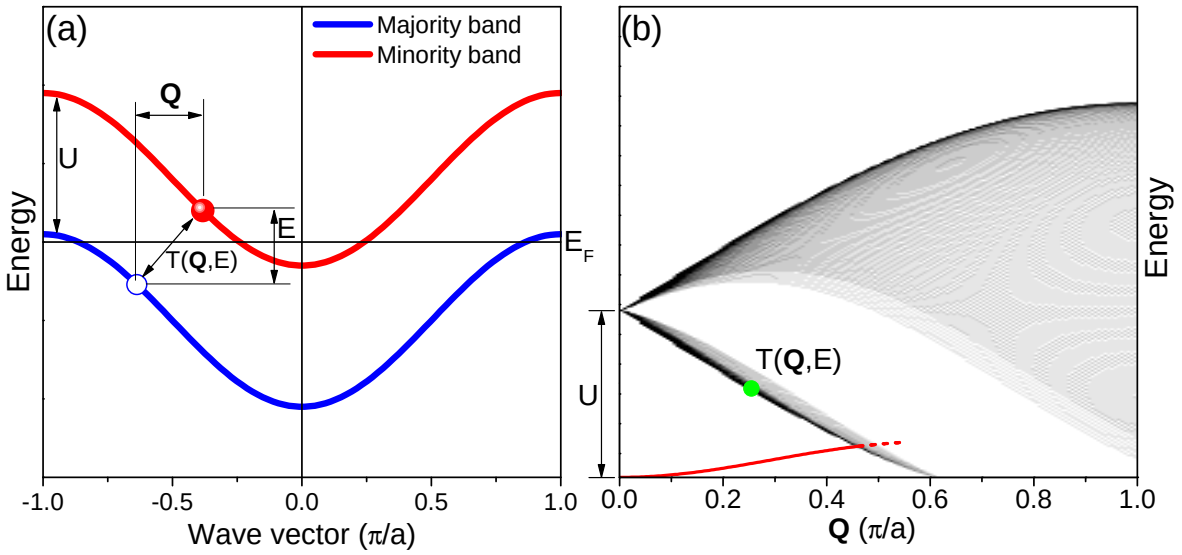

Figure 2.6: The schematic illustration of Stoner excitations of the majority-hole with minority-electron states in a weak ferromagnet. (a) shows a simple band structure with the band splitting U. The Stoner excitation T(Q,E) is the state with a majority hole (blue circle) under the Fermi level and a minority electron (red spheres) above the Fermi level. (b) shows the Stoner continuum for the simple electronic band structure in (a). The gray scale schematically represents the density of the Stoner states. The red line represents the dispersion of spin waves. In the intersection between spin wave dispersion and the Stoner continuum, spin waves strongly decay into the Stoner excitations.

transition metals are much more complicated. There are more than one electronic bands, and the band splitting is not uniform throughout the Brillouin zone either. The Stoner continuum in a real metal may be quite different from the one shown in Fig. 2.6(b). At Q=0, Stoner excitations (majority-hole, minority-electron) reveal a broad peak with the maximum centering between 2 eV and 2.5 eV in the study of bcc Fe using the spin-polarized electron energy loss spectroscopy [38–40]. Nevertheless, the band splitting in the 3*d* magnetic metals can be qualitatively estimated as demonstrated in the study of Stoner excitations [38–41].

2.2.2 Relation between spin waves and Stoner excitations

Spin waves and Stoner excitations have been described in two different pictures so far, the localized spin picture and the itinerant electron picture. It was firstly pointed out by Slater [42] in 1937 that discrete energy levels can be found under the Stoner continuum. They are the correlated states of the electron-hole excitations, which can be taken as the spin wave excitations in the itinerant electron model. The theory of the spin wave states in a metal was developed by Herring and Kittel [43, 44], in which these excitations coexist with the Stoner excitations in the system [45]. The $T^{\frac{3}{2}}$ law dependence of the magnetization on temperature has been found at low temperature as well [43]. For the spin waves with any finite energy, they decay into the Stoner excitations in the itinerant electron system, which give spin waves the finite lifetimes [45]. The decay of

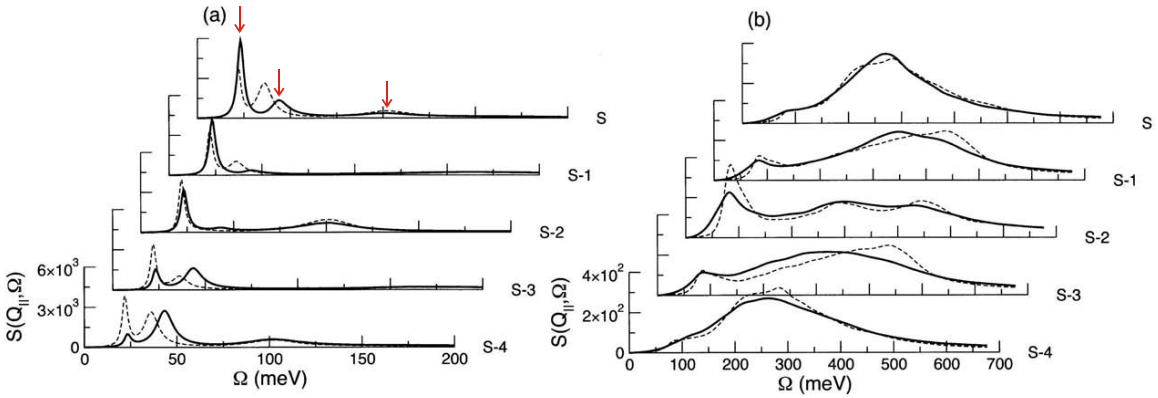

Figure 2.7: The spectral density functions calculated for a 5 ML Fe slab on W(110) [27], which are calculated for Q = 0.2 $(2\pi/a_0)$= 0.44 Å^{-1} (a) and Q = 0.6 $(2\pi/a_0)$= 1.32 Å^{-1} (b) along the [001] direction. The spectra are calculated for each individual layer in the film. S denotes spectrum for the surface layer. The solid curves are the spectral density function for the 5 ML Fe slab on W(110), and the dashed curves are calculated for the free standing 5 ML Fe slab. The red arrows indicate the three distinct spin wave modes, which are strongly broadened due to the decay of the spin waves into the Stoner excitations.

spin waves becomes severe in the intersection of the spin wave dispersion and the Stoner continuum, which is indicated in Fig. 2.6 (b). In this region, the dispersion and lifetimes of the spin waves are strongly modified [45]. Therefore, the complete description of the spin waves in a metal has to consider the itinerant property of electrons.

Theoretical calculations considering the itinerant property of the electrons have been established to describe the spin waves in the 3*d* metals [29, 35, 46–48]. One important approach is based on the adiabatic approximation, which assumes that the time scale of the precession of the magnetic moments is sufficiently larger than the characteristic time of the motion of electrons. Therefore, the fast motion of itinerant electrons can be decoupled from the slow motion of the spins. The adiabatic approximation is adopted to calculate the change of electronic energy due to the precession of the magnetization. Within this method, the exact spin wave stiffness can be obtained for the long wavelength limit [35]. The spin wave stiffness coefficients for Fe, Co and Ni shown in Tab. 2.1 were calculated based on this approach [35]. However, the spin waves with high wave vectors strongly decay into the Stoner excitations, which can not be described in this method. The spin wave dispersion calculated using this method can be only compared to the other adiabatic calculations, but not to the experimental results [35].

Another theoretical approach is to include all magnetic excitations into a spectral density function [26–29, 37, 48–52]. Based on the description of the electronic band structure, the so-called transverse susceptibility are calculated, which depends on both the spin wave wave vector and frequency. It can be understood as the magnetic response of the system to an applied transverse magnetic field [27]. The spectral density function $S(Q_{||},\Omega)$ is obtained from the imaginary part of the transverse susceptibility. In this method, the strong damping effect due to the Stoner excitations is naturally included in the calculation, which enables to obtain a line width of the spin wave

excitations in the spectrum [27]. The spin waves described in this theory are in semi-quantitative agreement with the measurements using the inelastic neutron scattering experiments [47, 53–55]. Recently, calculations based on this approach have been also performed for the spin waves in the ultrathin Co films, which is in a good agreement with the experimental results [2, 50].

Theoretical studies based on this approach have been carried out for the Fe thin films on W(110) by Costa, Muniz and Mills [26–29]. Fig. 2.7 shows the spectral density functions $S(Q_{||},\Omega)$ for a 5 ML Fe film with the reduced wave vector $Q = 0.2$ $(2\pi/a_0)$ and $Q = 0.6$ $(2\pi/a_0)$ along the [001] direction [27]. They are calculated for both the free standing Fe film (dashed curves) and the film grown on the W(110) surface (solid curves). The spectra marked by the symbol S are the spectral density of the spin waves for the topmost Fe atomic layer. For $Q = 0.2$ $(2\pi/a_0)$, three modes can be distinguished in the spectral density function, which are indicated by the red arrows in Fig. 2.7 (a). This multi-peak structure can be understood as an array of Heisenberg-type eigenmodes, which are broadened by the strong damping [27, 37]. According to the Heisenberg model, 5 modes are expected in this system. Due to the strong damping effect, only three modes remain in the spectrum, while the other two modes are washed out. Among the three remaining modes, the mode with the lowest energy is less damped as compared to the other two, which is the dominating feature in the spectrum. This damping effect is even stronger for the spin waves with higher wave vector. This can be seen in Fig. 2.7 (b) for $Q = 0.6$ $(2\pi/a_0)$. There is no distinct excitation peaks, but a single broad profile in the spectra, which is attributed to the overlap of all strongly damped modes [27].

However, the spectral density functions in Fig. 2.7 show very weak Stoner excitation background in the spectra. This is attributed to the assumption applied in the calculation that the magnetic moment in the sample rotates rigidly as it fluctuates in response to spin wave excitation [27]. Therefore, these spectra density functions does not fully represent the excitations obtained in the SPEELS experiments, in which the Stoner excitations usually show up prominently. To introduce the Stoner excitations in the spectra, one needs to allow the moment to distort in shape as well as direction [27]. The spectral density functions in Fig. 2.7 already provide a good description for the spin wave excitations [37], which can be compared with the spin wave feature in the experimental spectrum.

2.3 Experimental techniques in spin wave study

There are several well established experimental techniques for the study of spin waves, such as the inelastic neutron scattering (INS), Brillouin light scattering (BLS), ferromagnetic resonance (FMR) and the spin-polarized electron energy loss spectroscopy (SPEELS). Recently the spin wave excitations have been also observed by means of the spin-polarized scanning tunneling microscopy (SP-STM) [56].

In the scattering techniques, such as INS, BLS and SPEELS, the energy and momentum of spin waves can be obtained from the inelastically scattered neutrons, photons and electrons, respectively. Due to the weak interaction between the neutrons and matter, INS is widely used in the spin wave measurements for bulk materials. In the

scatterings, the magnetic moment of the neutrons can interact with the fluctuation of the magnetization [31]. Due to this interaction, neutrons can be scattered by the spin waves and Stoner excitations. The kinetic energy of the incident neutrons is typically of hundreds of meV, whose wave length is comparable to the lattice constant of the crystal investigated. The spin waves studied by INS cover a large part of the Brillouin zone.

In BLS, light can be coupled with the change of the magneto-optic constants due to the presence of spin waves [57]. The creation or annihilation of spin waves causes a frequency shift of the light, which is typically in the range of GHz [58]. Because of the small penetration depth of the light, which is of the order of 1 μm [59], the BLS is suitable for the study of surfaces and thin films. The spin waves probed by the BLS are typically of the wave vector from 10^{-6} to 10^{-2}Å^{-1} [57]. For the Fe films on W(110), the surface spin wave mode (Damon-Eshbach mode) of the energy 30 GHz (0.12 meV) has been observed [6], which can be used to study the magnetic anisotropy.

SPEELS is also a scattering technique, in which an electron beam with two opposite spin polarizations is applied. The intensity spectrum of the scattered electrons is measured as a function of their energy. The magnetic excitations, such as the Stoner excitations and spin waves, are excited through the exchange interaction between electrons. In this technique, the wave vector of the magnetic excitations can be measured up to the Brillouin zone boundary [2]. In some SPEELS experiments [39, 40], additional spin analysis of the scattered electrons is performed, which is referred to as the "complete experiments". The full spin information of the electron before and after scattering can be obtained in these experiments. However, it will be shown that the spin analyzer is not necessary for the measurements of spin wave excitations(Sec. 3.2.1). A detailed description of this method will be given in the next chapter (Sec. 3.2).

In the FMR experiments, samples are placed into a microwave cavity, where the microwave loss is measured as a function of the applied magnetic field. The losses of the power of reflected or transmitted microwave are detected in the resonance between the precession of the magnetic moment and the rf-microwave. The spin waves studied in FMR are around the long wave length limit [60]. The spin wave energy is dominated by the magnetic anisotropy energy. Therefore, FMR has been widely applied in the study of the magnetic anisotropy for the magnetic thin films [58].

In the SP-STM experiments, the conductivity dI/dU between the tip and sample is measured as a function of the potential bias U, where I is the tunneling current. When U is large enough, the tunneling electrons have enough kinetic energy to overcome the energy of certain excitation in the sample, and the tunneling current is enhanced due to the increase of the number of final states [56]. This causes a step in dI/dU and a peak in d^2I/dU^2 spectrum, whose position corresponds to the energy of the excitation. However, this technique can not give the information of excitations with the in-plane wave vectors.

For the study of high wave vector spin waves in bulk Fe, only INS has been widely applied in the last 30 years [54, 55, 61–66]. Fig. 2.8(a) shows the spin wave dispersions measured for a single crystal sample of Fe^{54} isotope(4% Si) at room temperature by Mook and Nicklow [54]. The spin waves can be observed up to about 100 meV. Above this energy the spin wave intensity decreased dramatically, which had been also observed in the later studies [54, 62, 65]. It is attributed to the intersection of the

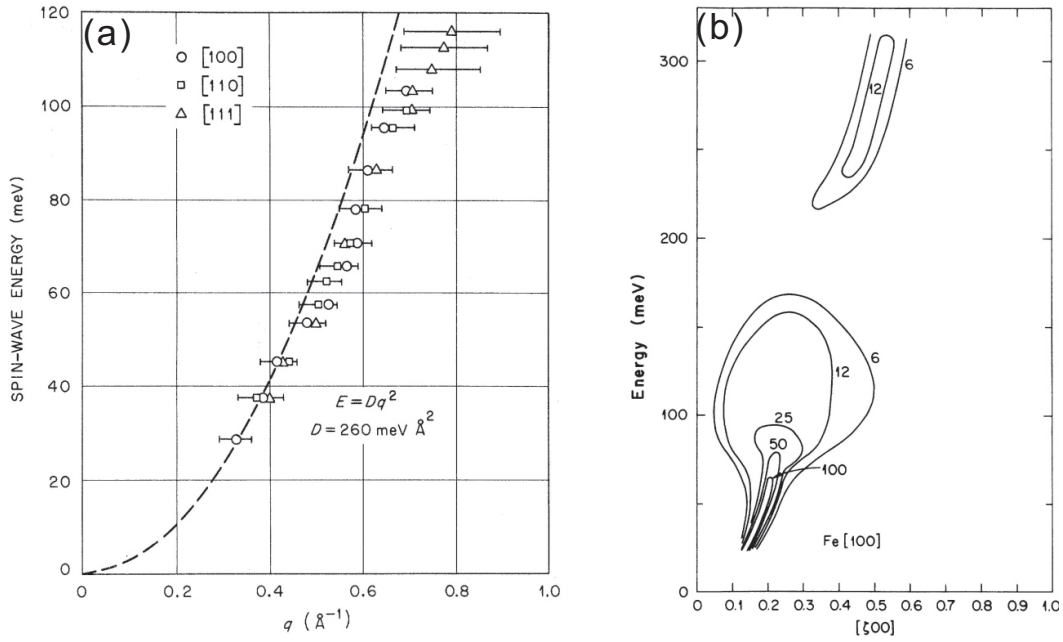

Figure 2.8: The spin wave dispersions measured by INS. (a) shows the spin wave dispersions along the [100], [110] and [111] directions, which are obtained from a single crystal ^{54}Fe(4 at.% Si) at room temperature [54]. The dispersion relations are very similar in the three directions. The spin wave stiffness D=260 meVÅ^2 was obtained from the measurements. (b) shows the spin wave intensity contours measured by INS in Fe^{54}(∼10% Si) at 77K [55]. It shows that the spin wave intensity reduces significantly where the spin wave energy is higher than 100 meV.

spin wave dispersion curve and the Stoner continuum as illustrated in Fig. 2.6. In bulk Fe, spin waves show quite similar dispersion relations along the directions, [100], [110] and [111] [54]. The dispersion relation can be described using an empirical relation $E = Dq^2(1 - \beta q^2)$, in which D is the spin wave stiffness. The factor β and the fourth power term enable a good fit in the high energy range. The D values for bulk Fe obtained from the INS experiments vary from 230 meVÅ^2 to 280 meVÅ^2 [54, 62, 65]. Similar values are also found in the theoretical studies, such as the work based on the adiabatic approximation as shown in Tab. 2.1 [35].

The INS experiments had been also performed to study the spin waves behavior above the Curie temperature [62, 63], and the spin wave dispersion in high energy range [55]. To description of the spin wave spectra, the theoretical calculations based on the itinerant electron theory had been established, which show a good agreement with the experimental results [47]. Fig. 2.8(b) shows the contour of the spin wave intensity along the [100] direction. The energy distribution of the spin wave excitations are broadened throughout the Brillouin zone. The spin wave dispersion was measured up to 300 meV, in which the intensity drop at 100 meV was also observed. The study of spin wave in the bulk Fe shows that the spin waves are strongly damped in bulk Fe, and the itinerant electron theory has to be applied to give a complete description for the spin waves of high wave vectors [27].

The measurements of spin waves in ultra thin Fe films had been concentrated in the

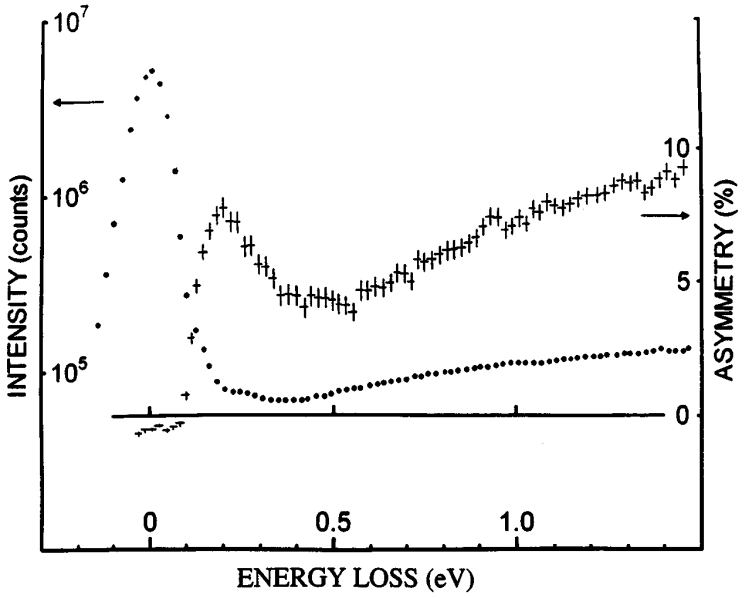

Figure 2.9: Spin wave excitations observed for the first time in SPEEL-spectrum. The SPEELS intensity (dots) and asymmetry spectra (crosses) are measured for 5 ML Fe/W(110). The incident energy is 29 eV relative to the Fermi level. With an incident angle of 55 degree, the wave vector transfer is about 0.62 $Å^{-1}$. The peak in the asymmetry spectrum at about 0.2 eV is attributed to the spin wave excitations, while the increase of the asymmetry after 0.5 eV is due to the Stoner excitations.

very small wave vector region, until the signature of the high wave vector spin waves was observed by Kirschner *et al.* using the SPEELS [1]. The experiment was performed on a 5-atomic-layer Fe film on the W(110) substrate. The results are shown in Fig. 2.9. The dot symbols denote the average intensity $(I_\uparrow+I_\downarrow)/2$ for $I_\uparrow$ and $I_\downarrow$, where $I_\uparrow(I_\downarrow)$ is the loss intensity when the spin of the electron beam is parallel (antiparallel) to the spin of majority electrons in the sample [1]. The cross symbols represent the asymmetry of the two intensity spectra, which is defined as $(I_\downarrow\text{-}I_\uparrow)/(I_\uparrow+I_\downarrow)$. In the asymmetry spectrum, the pronounced peak at the energy loss of about 0.2 eV is attributed to the spin wave excitations. The asymmetry increases gradually again for the energy loss larger than 0.5 eV, which is due to the Stoner excitations [1]. This is the first time that spin wave signature is observed in the SPEELS experiments. Using a new SPEEL-spectrometer with a higher resolution [67], the first measurement of the spin wave dispersion up to the Brillouin zone boundary was realized by Vollmer *et al.* on an fcc Co film on Cu(100) [2]. The subsequent studies were carried out concerning the spin waves in the fcc Co films for different thicknesses [68, 69] and a hcp 8 ML Co/W(110) system [70]. The maximum energy of the spin waves observed at the Brillouin zone boundary is 250 meV for the fcc Co film, and about 400 meV for the hcp Co film, respectively. The spin wave dispersions observed in both systems can be well described by the nearest neighbor Heisenberg model [2, 71], in which the product of the exchange constant J and the spin moment S is obtained as $JS \approx 15$ meV for both systems. The spin wave dispersion and spectra obtained in the SPEELS experiments can be also well described by the spin wave theory in an itinerant electron model [37, 50].

Although the signature of the high wave vector spin waves in SPEELS was observed in the 5 ML Fe/W(110) system, it was difficult to obtain a dispersion relation from the asymmetric and strongly broadened excitation peaks. According to the theoretical predictions, the distinct spin wave peaks are expected in the spectrum in the low wave vector range as shown in Fig. 2.7 (a) [27], although they are significantly damped. Experimentally, a dispersion was only observed in the system of 3 ML Fe/1 ML Co/Cu(100). However, the spin waves in the pure Fe thin films always show broad peaks showing no explicit dispersion relation [23, 24, 72]. This obvious discrepancy between the theory [27] and experimental results [24] motivated us to perform systematic studies of the spin wave excitations in the Fe thin films on W(110).

Chapter 3

SPEELS and experimental details

In the first part of this chapter, the construction of the ultra high vacuum (UHV) system used in this work is introduced. The construction and operation of the spin-polarized electron energy loss spectroscopy (SPEELS) are described in the second part. The preparation and characterization of the Fe films will be described in the third part.

3.1 Ultra high vacuum system

The experiments are performed in a UHV system consisting of three chambers, which is shown in Fig. 3.1. The SPEEL-spectrometer is mounted in the SPEELS chamber (blue cylindrical chamber). Samples are prepared in the analysis chamber (red). They can be transferred between the analysis chamber and the SPEELS chamber by the manipulator (yellow). The transfer of the sample is always along the main axis of the system, which is the central axis of the SPEELS and analysis chamber, as denoted in Fig. 3.1. The samples are prepared by the molecular beam epitaxy (MBE) method and characterized using the surface analysis techniques, such as Auger electron spectroscopy (AES), low energy electron diffraction (LEED), magneto-optic Kerr effect (MOKE), and medium energy electron diffraction (MEED). The cathode chamber (green) is directly connected with the SPEELS chamber. In this chamber, a GaAs photocathode, which serves as the polarized electron source, is prepared. It will be transferred into the SPEEL-spectrometer before the SPEELS measurements.

In a typical SPEELS-measurement, the Fe film is prepared and magnetized in the analysis chamber. Meanwhile, in the cathode chamber, the GaAs photocathode is prepared by the deposition of Cs in an oxygen atmosphere (2×10^{-8} mbar), which is then transferred to the SPEELS chamber. After the sample is transferred and placed at the scattering position in the SPEEL-spectrometer, the SPEELS measurement is started. The base pressure in the SPEELS chamber is better than 4×10^{-11} mbar during the measurements.

3.2 SPEELS

In the electron energy loss spectroscopy (EELS) study, the electron beam with defined incident energy are shot onto the sample surface. Along a certain direction, the scat-

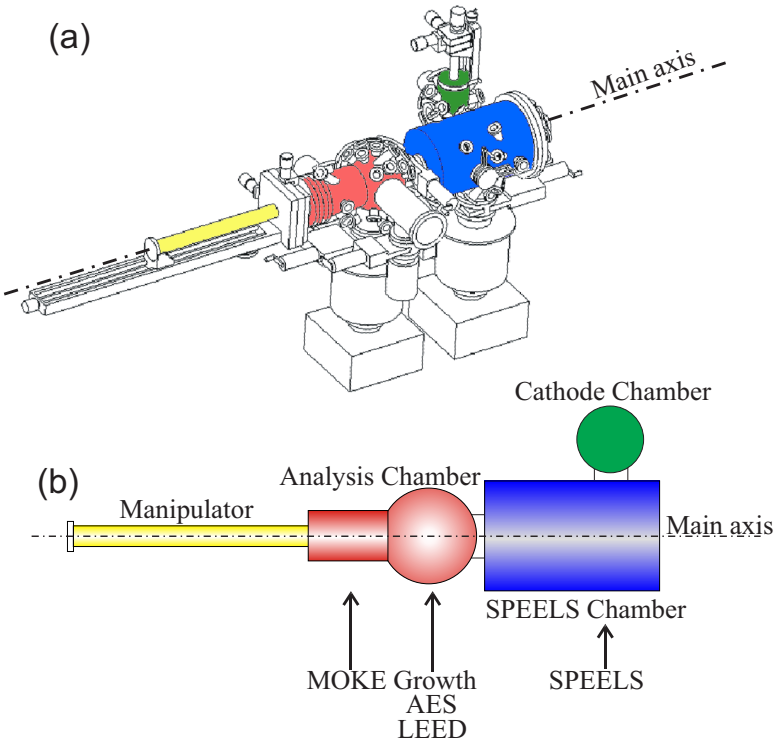

Figure 3.1: (a) The 3D drawing of the UHV system used in this work. (b) Top view of the UHV system. Colors indicate different parts of the UHV system, which are the manipulator (yellow), the analysis chamber (red), the SPEELS chamber (blue) and the cathode chamber (green), respectively. Samples can be transferred between the analysis chamber and the SPEELS chamber by the manipulator. The GaAs photocathode is transferred between the cathode chamber and SPEELS chamber for the photocathode preparation and the SPEELS measurements. The sample positions for different measurements are all on the main axis, indicated in (b).

tered electrons are recorded as a function of their energies. The energy distribution of the scattered electrons provides the information of the elastic and inelastic scattering processes experienced by the electrons at the sample surface. In the latter case, the excitations of the electrons, atoms and molecules are involved, which may also lead to the excitations of quasi-particles, such as phonons, plasmons and magnons.

In the following subsections, the scattering processes of the electrons on the sample surface will be firstly introduced. Then the construction, operation and performance of the SPEEL-spectrometer are briefly described. The description of the SPEELS experiment is given in the third subsection, in which an example of the SPEELS spectra will be also presented.

3.2.1 Inelastic scattering of electrons

For the inelastically scattered electrons, they lose or gain energy by creating or annihilating excitations at the surface. Assuming that an electron only experiences one scattering event during the scattering, the energy E of the excitations is given by $E = E_i - E_f$, in

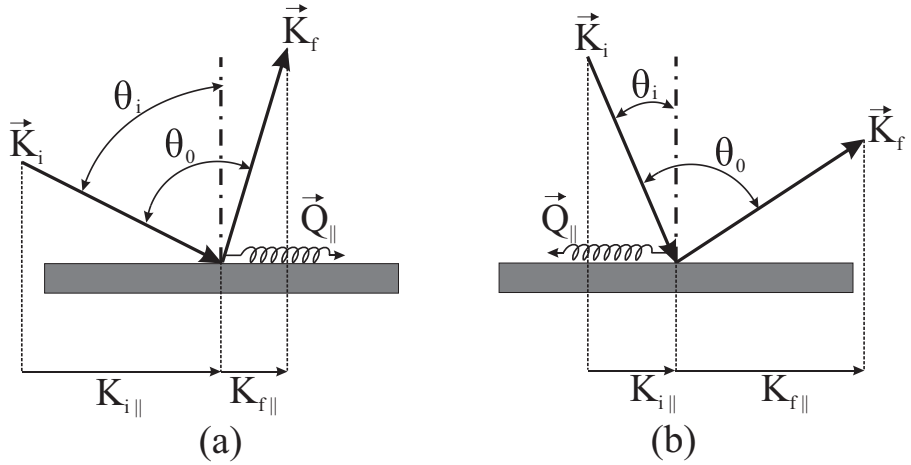

Figure 3.2: The geometry of the SPEELS-experiment for the positive (a) and negative (b) in-plane wave vector, $\vec{Q}_{||}$. θ_0 is the angle between incident and outgoing direction, and θ_i is the angle of incidence. $\vec{K}_i$ and $\vec{K}_f$ denote the wave vectors of the incident and outgoing electrons, whose in-plane components are $K_{i||}$ and $K_{f||}$.

which E_i and E_f denote the incident and final energies of the scattered electrons. As the in-plane momentum of the electrons is conserved during the scattering process, the in-plane wave vector of the excitation is given by

$$\vec{Q}_{||} = -\Delta K_{||} = K_{i||} - K_{f||} = \vec{K}_i \sin(\theta_i) - \vec{K}_f \sin(\theta_0 - \theta_i), \tag{3.1}$$

which is illustrated in Fig. 3.2. $\vec{Q}_{||}$ is the in-plane wave vector of the excitation, which can be either positive or negative as shown in Fig. 3.2(a) and (b), respectively. $\Delta K_{||}$ is defined as the change of the wave vector parallel to the surface. The wave vectors of incident and outgoing electrons are represented by $\vec{K}_i$ and $\vec{K}_f$. Their in-plane components are $K_{i||}$ and $K_{f||}$, respectively. θ_i and θ_0 are the incident angle and the angle between the two beams. Here we confine our discussion in the first Brillouin zone, so the reciprocal lattice vector $\vec{G}_{||}$ does not appear in Eq. 3.1.

The inelastic mean free path (IMFP) of the electrons depends on both the kinetic energy of the electrons and the material. The energy dependence of IMFP can be described by a "universal curve". Due to the excitation of the valence band electrons, the IMFP shows a broad minimum (< 10 Å) at about 50 eV [73]. In the lower energy region, an increase of IMFP is shown in the universal curve. However, it only increases slightly at low energies in $3d$ transition metals, where the IMFP of electrons is also spin dependent [74–76].

The IMFP in Fe is about 4.5 Å and 6 Å for the minority and majority electrons with the energy of about 9 eV relative to the Fermi level [74]. Due to the short inelastic mean free path of the low energy electrons, they are extremely surface sensitive.

The inelastic scattering mainly results from the dipolar and impact scattering processes. The former process refers to the scattering of electrons by the electric dipolar field. It can be described using the classical dielectric dipolar theory, and the detailed microscopic description of the electrons and the sample surface is not necessary [77]. The dipolar scattering mainly happens for the scattered electrons close to the specular

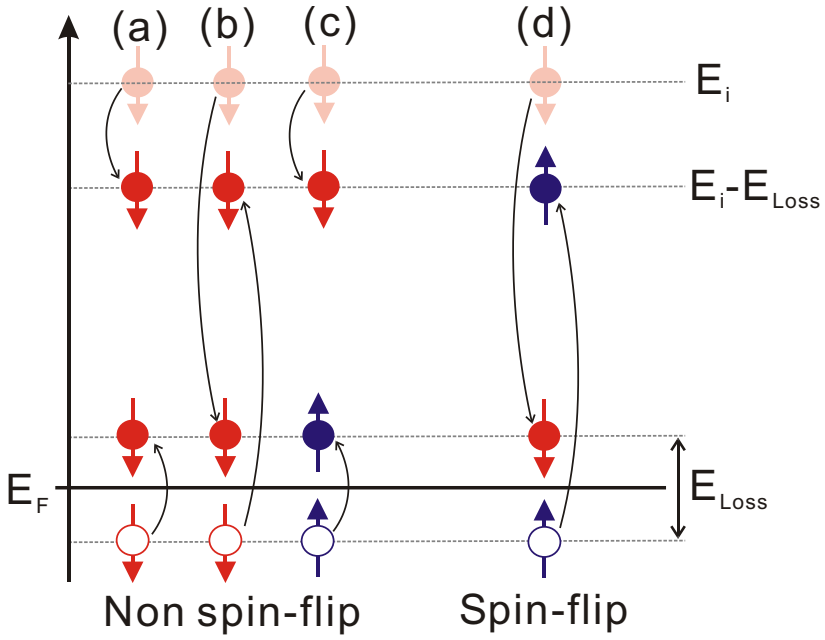

Figure 3.3: The illustration of the inelastic exchange scattering processes for the incidence of spin down electrons. The solid balls represent the electrons with up (blue) and down (red) spins. The circles denote the holes left in the system. E_F and E_i are the Fermi energy and incident electron energy, respectively. E_{Loss} is the energy loss of electrons in the scattering process. (a) and (b) show that the incident spin down electrons are scattered by the same spin down electrons without and with the exchange of electron. (c) and (d) show the scattering by the spin up electrons without and with the exchange of electrons. The spins of the outgoing electrons are not changed in (a), (b) and (c), which are indicated as non spin-flip processes. Only in (d), the spin of electron is flipped as compared to the spin orientation of the incident electron.

direction. In this work the SPEELS measurements are all performed in off-specular geometry. In this case the obtained spectra are mainly due to the impact scatterings. In contrast to the dipolar scattering, an impact scattering occurs very close to the sample surface or even inside the sample. The inelastic scattered electrons are usually distributed over a large range of angle. At present, the impact scattering is still poorly described by the theory due to lack of the details about the interaction between the electrons and the sample surfaces [77].

In the impact scattering processes, the incident electrons exchange with the electrons in the sample. Fig. 3.3 shows the scattering processes in a ferromagnet for the incidence of spin-down electrons (with spin parallel to the spin of minority electrons in the sample). The energy of the incident electrons is E_i. After scattering, the outgoing electrons have the energy of E_i-E_{Loss}. Meanwhile, the electrons in the sample are excited above the Fermi level and leave holes in the system. For examples in (a) and (b), incident electrons interact with the spin down electrons in the sample, and experience either the non-exchange process (a) or exchange process (b). (c) and (d) show the case that the incidence of spin down electrons are scattered by the spin up electrons with the non-exchange and exchange processes, respectively. In (a), (b) and (c), the outgoing

electrons show the same spin orientation as that of the incident electrons, which are non spin-flip processes. In (d), the spin of the outgoing electron is antiparallel to the incident spin, and looks as if the incident spin is flipped after the scattering. Case (d) is thus marked as the spin-flip process. However, it should be pointed out that the apparent spin-flip is due to the exchange of electrons instead of the real spin reversal [39]
.

In the case of the creation of a magnon, the angular momentum of a ferromagnetic system is reduced by 1 $\hbar$. Due to the angular momentum conservation in the scattering, the spin momentum of the outgoing electron must be increased by 1 $\hbar$ as compared to the incident electron. This can be only accomplished by the spin down electron with the spin flip, from down to up, as illustrated in Fig. 3.3 (d). As spin up electrons can not increase their spin momentum, it is thus forbidden for the spin up electrons to create spin waves in ferromagnetic system.

3.2.2 SPEEL-spectrometer

The SPEEL-spectrometer consists of two main parts, the electron energy monochromator and the energy analyzer, as shown in Fig. 3.4. The monochromator is composed of two connected cylindrical electric deflectors. The deflection angles are 90° and 180°, respectively. The cathode is located in front of the 90°-monochromator as indicated by the green ellipse in Fig. 3.4. The monochromator is fixed during the SPEELS measurements.

A circularly polarized leaser beam (red line) with the wavelength of 830 nm is applied to in the creation of spin-polarized electrons. The laser is reflected by a mirror and finally focused onto the surface of the GaAs photocathode. The final direction of the laser beam is parallel to the main axis. According to the selection rules [78], the emitted electrons will have their spins parallel or antiparallel to the incident direction of the laser beam (also the main axis), depending on the polarization of the light. Only the electrons with the proper energy may pass through the 90° and 180° deflectors, and finally be focused onto the sample surface. During the flight of the electrons, their spin momenta are conserved, which are kept parallel or antiparallel to the main axis. Meanwhile, the magnetization of the sample is also along the main axis. Hence, the spins of electrons can be controlled to be parallel or antiparallel to the magnetization by changing the polarization of the light.

The analyzer is a 146° cylindrical deflector. It can be rotated about the main axis. The angle between the monochromator and the analyzer can be adjusted from 80° to 280°. Next to the exit slit of the deflector is the channeltron, which works in the counting mode at a high potential of about 2400 V. There is no further spin detector connected to the analyzer. During the measurements, the energy distribution of the scattered electrons is scanned by the analyzer under a direction. The spectral intensity is the number of pulses generated by the electrons in a time unit (usually second).

In a SPEELS measurement, the sample is positioned at the scattering center as shown in Fig. 3.4, which has been magnetized in remanent state along the main axis. No external magnetic field is applied during the measurement. The manipulator can be freely rotated around the main axis, which offers the measurements for different in-plane wave vector transfers as derived from Eq 3.1. The scattering space is surrounded

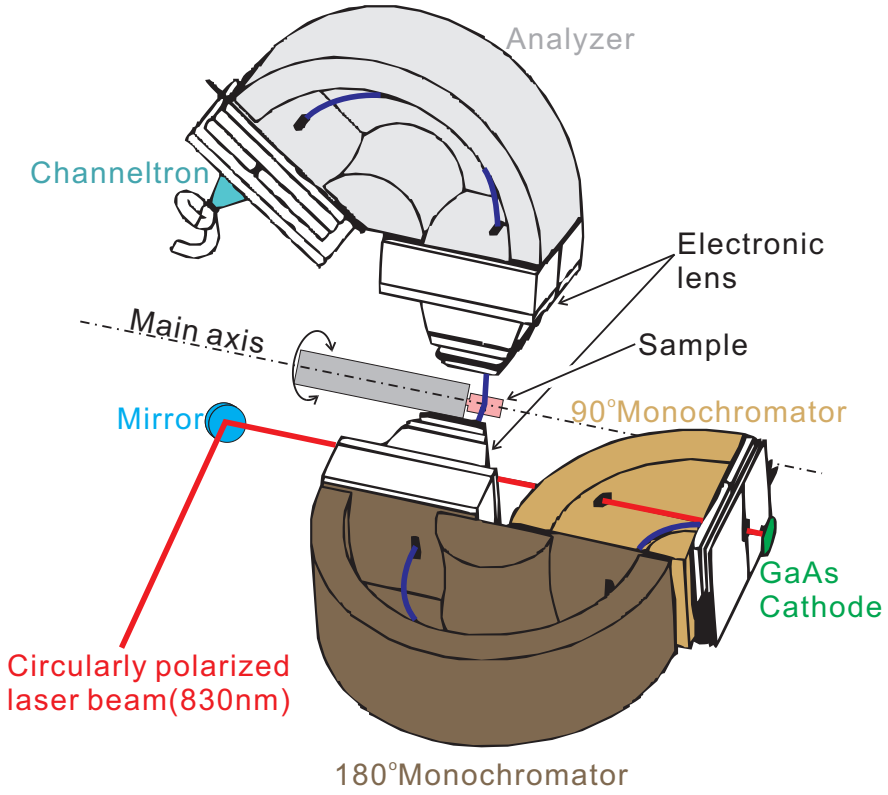

Figure 3.4: The 3D drawing of the SPEEL-spectrometer. A circularly polarized laser beam (red line) is shining on the GaAs photocathode (green ellipsis). The trajectory of the emitted electrons are denoted by the blue curves. The black dash-dot line indicates the main axis of the spectrometer, which is same as the one shown in Fig. 3.1. The analyzer and the sample can be rotated about the main axis. In the measurements, the angle between the analyzer and monochromator is fixed at 80°. The sample is rotated with respect to the main axis in order to measure the spin waves with different in-plane wave vector transfers.

by metal sheets (not shown in the graph). These shields keep the homogeneity of the electric field in the scattering cage.

After scattering, most of the incident electrons are conducted away through the sample, while only a small percentage (around 5%) is scattered off. Hence, the sample current can be taken as a rough estimate for the intensity of incident electron beam. This sample current is typically from 2 nA to 20 nA in this work. The intensity of the scattered electrons strongly depends on the experimental geometry. In off-specular geometry, the electrons received by the channeltron varies in the range of 1∼1000 per second. When the analyzer is approaching the specular direction, the number of collected electrons is even higher.

The incident electron energy in the SPEELS measurements is defined as the kinetic energy of the electrons with respect to the vacuum energy level. In most of experiments of this work, the incident energy is 4 eV. To probe the spin waves with high wave vector transfers, the incident energy of 6.75 eV was applied. The energy resolution of the electron beam is estimated from the full width at half maximum (FWHM) of the

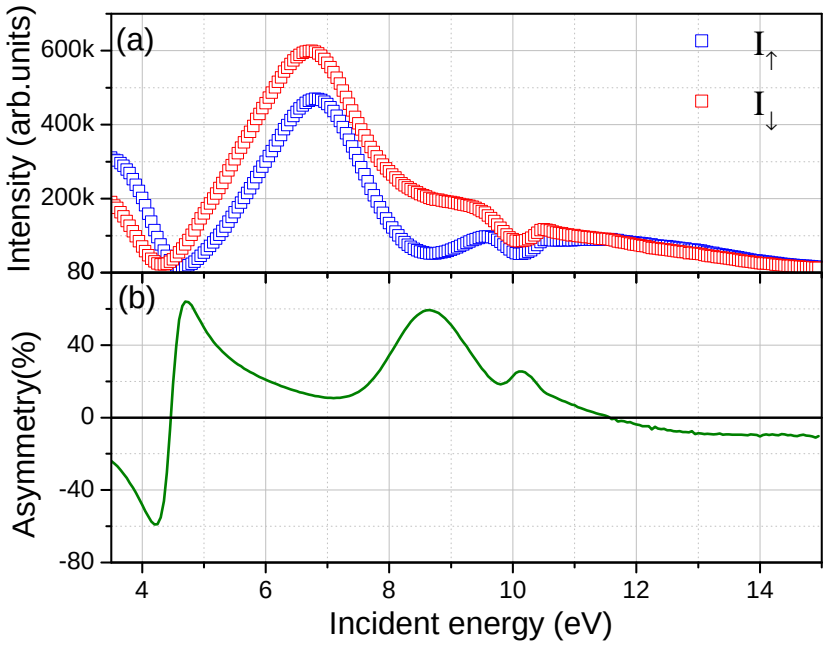

Figure 3.5: (a) The intensities of the elastically scattered electrons in the specular geometry as function of the incident energy for the incident spins parallel ($I_\uparrow$) and antiparallel ($I_\downarrow$) to the spin of majority electrons. (b) The asymmetry of the two intensity curves, A = ($I_\downarrow$-$I_\uparrow$)/ ($I_\downarrow$+$I_\uparrow$). The highest asymmetry of 64% is at the incident electron energy of 4.7 eV, from which the polarization of the incident electron beam can be estimated (see text).

energy distribution of the specularly scattered electrons. It is typically from 15 meV to 20 meV for most of the SPEEL-spectra. The resolution of the in-plane momentum transfer has been estimated from the angular distribution of the electron intensity in specular geometry [71]. The angular distribution showed a Gaussian peak with the FWHM of about 2°. This corresponds to a resolution of better than 0.05 $Å^{-1}$ for the incident energy of 4 eV.

3.2.3 GaAs photocathode

A strained GaAs cathode is employed as the source of highly spin-polarized electrons. Due to the spin-orbit interaction, the p valence band in the GaAs is split. The polarization of the photoemission is obtained by the selective excitation of the electrons in the split p bands using a polarized light with proper energy [78]. For an unstrained GaAs cathode, the theoretical polarization of the photoemission is 50%. Higher polarization can be achieved by introducing strain into the cathode surface, which removes further the degeneracy of p band [78]. Prior to the application of the GaAs cathode, its surface is covered with Cs in the oxygen atmosphere (2×10^{-8} mbar). The workfunction at the surface is lowered by this treatment, so that more photo-electrons may overcome the workfuction barrier and leave the GaAs surface. In the SPEELS measurements, the photoemission current is typically between 1 μA and 6 μA.

To estimate the polarization of the electron beam, the intensity of the specular beam

reflected from a clean W(110) surface is measured as a function of incident energy. In Fig. 3.5 (a), $I_\uparrow$ and $I_\downarrow$ are intensity spectra obtained for the incident spin parallel and antiparallel to the spin of majority electrons. Due to the strong spin-orbit interaction experienced by the incident electrons in W(110), $I_\uparrow$ and $I_\downarrow$ show a large difference depending on the incident energy. The asymmetry of $I_\uparrow$ and $I_\downarrow$ is defined as $A=\frac{I_\downarrow - I_\uparrow}{I_\downarrow + I_\uparrow}$ shown in Fig. 3.5 (b). The largest asymmetry is about 64% at 4.7 eV. For a partially polarized electron beam, the measured asymmetry is the product of the beam polarization P and the factor S (Sherman function [79]), where S gives the ideal asymmetry in the case of a totally spin-polarized electron beam is applied. Its values is not larger than 1. If we take S = 1 at 4.7 eV, which is the theoretical maximum for S, the lower limit of the spin polarization is estimated to be P = A/S = 64%/1 = 64%. On the other hand, one can assume that the largest value of S for the tungsten surfaces is never larger than 80% as demonstrated in previous studies [80–82]. If we take S = 0.8 at 4.7 eV, the electron polarization is P = A/S = 64%/0.8 = 80%. As an estimation, we chose the average of the two values obtained above, which is 72±10%, as the spin polarization of the electron beam.

3.2.4 SPEELS measurements

For the Fe films studied in this work, the geometry of the electron scattering in the SPEELS measurements is illustrated in Fig. 3.6. The spin waves are probed along the [001] ([00$\bar{1}$]) direction on Fe(110), which corresponds to the $\bar{\Gamma}\bar{H}$ direction in the reciprocal space as shown in Fig. 3.6 (c). The magnetization of the Fe film is aligned along the [1$\bar{1}$0] direction. During the measurement of the spin wave dispersion, θ_0, the angle between incident and outgoing electron beams, is fixed at 80°. The spin waves of different wave vectors can be measured by rotating the sample about the main axis as shown in Fig. 3.6 (a). It corresponds to varying the θ_i in Eq. 3.1 individually. Different in-plane wave vector transfers ($\Delta K_{||}$) can be realized according to Eq. 3.1. The spin of the incident electrons is oriented parallel or antiparallel to the spin of majority electrons in the Fe film. The corresponding intensity spectra are indicated as $I_\uparrow$ and $I_\downarrow$, respectively. The energy of spin wave excitations is less than 0.2 eV, which is very small as compared to the incident energy of 4 eV. Thus, the SPEEL-spectrum obtained for certain θ_i can be taken as the constant wave vector scan. As a good approximation, $\Delta K_{||}$ is calculated by replacing $\vec{K}_\mathrm{f}$ with $\vec{K}_\mathrm{i}$ in Eq. 3.1. The error of $\Delta K_{||}$ in this procedure is less than 0.02 $\mathrm{\AA}^{-1}$, which is within the wave vector resolution of the experiments.

Prior to the SPEELS measurements, the incident energy of the electron beam is calibrated. In this procedure, the electron beam is directed perpendicularly to the sample surface with the energy of 4 eV, which is estimated from the pass energy of the 180° monochromator and the potential difference between the monochromator and the sample. The electric current received by the sample is then measured as a function of a negative potential applied on the sample. This applied potential is to prevent the electrons from reaching the sample surface. As the negative potential varies from -5 V to -3 V, a sudden increase of the sample current can be observed at a certain potential. This indicates that electrons can overcome the potential barrier and start reaching the sample surface. It also means that the vacuum level of the sample is now same as that of the incident electrons. Based on this critical potential point, the potential

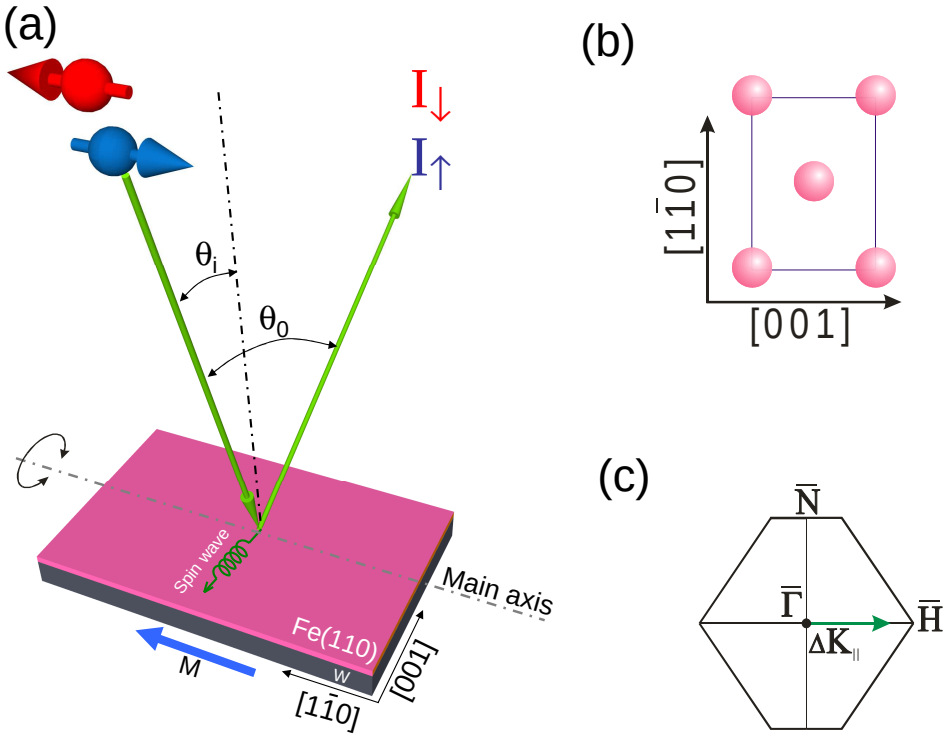

Figure 3.6: (a) The scattering geometry of SPEELS experiments. The spectrum of $I_\downarrow$ or $I_\uparrow$ are obtained with the spin of the incident electrons parallel (red) or antiparallel (blue) to the magnetization direction ($[1\bar{1}0]$) of the Fe film. The spin waves is probed along the [001] or $[00\bar{1}]$ direction. θ_i is the incident angle. θ_0 denotes the angle between incident and outgoing electron beams. In the experiments, the sample is rotated about the main axis to measure the spin waves with different in-plane wave vector transfers, $\Delta K_{||}$. For the Fe(110) surface, the unit cell in the real space and the first Brillouin zone are shown in (b) and (c), respectively. $\Delta K_{||}$ is denoted by the green arrow in (c).

applied on the sample is then precisely increased by a positive 4 V. It assures that the incident electron energy is strictly 4 eV with respect to the vacuum level of the sample. The uncertainty of the incident electron energy is about ±0.1 eV, which is due to the uncertainty in the determination of the critical potential point.

SPEEL-spectra are the scans of electron energy with a certain energy step, which is usually between 3 meV and 6 meV. At one energy point, the polarization of the incident electrons is fixed in one direction, e.g., parallel to the spin of majority electrons. The analyzer counts the scattered electrons for one second. The number of the electrons is recored in $I_\uparrow$. After that, the spin of the incident electrons is switched to the opposite direction by switching the polarity of the laser beam. The analyzer collects the electrons for another second for $I_\downarrow$. The same process is repeated for each energy point in the scanning energy range. It is usually necessary to repeat a number of scans and sum them up, in order to achieve a satisfying signal-to-noise ratio. Finally, two intensity spectra, $I_\downarrow$ and $I_\uparrow$, are obtained for the two opposite spin polarizations of the incident electrons.

As an example, the energy loss spectra obtained in the SPEELS measurement for

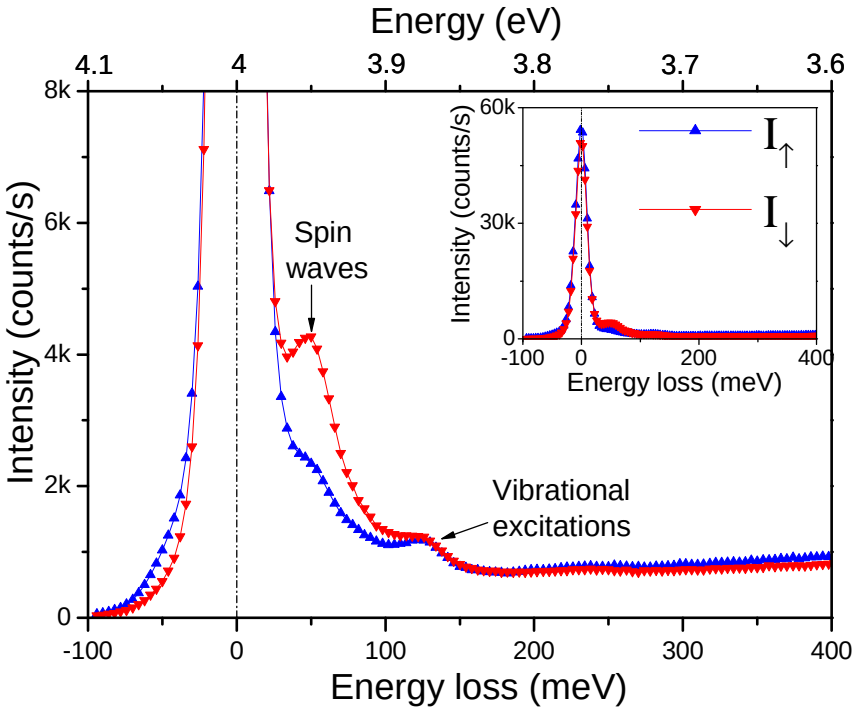

Figure 3.7: The SPEEL-spectra measured for 2 ML Fe/W(110) with the in-plane wave vector transfer of 0.5 $Å^{-1}$. The incident energy is 4 eV, and the energy resolution is FWHM≈20 meV. The $I_\uparrow$ (blue) and $I_\downarrow$ (red) are recorded with the spin of incident electrons parallel and antiparallel to the spin of majority electrons in the sample. The top axis shows the kinetic energy for the electrons with respect to the vacuum level. The features of the spin wave excitations and vibrational excitations can be observed in the spectra as indicated by the arrows. The inset reveals the full scale of the elastic peak.

2 ML Fe/W(110) are shown in Fig. 3.7. The incident electron energy is 4 eV with the energy resolution of about 20 meV. The in-plane wave vector transfer $\Delta K_{||}$ is 0.5 $Å^{-1}$. The intensity spectra, $I_\uparrow$ and $I_\downarrow$, are recorded with the spin of incident electrons parallel and antiparallel to the spin of majority electrons in the sample as illustrated in Fig. 3.6 (a). In the energy loss spectrum, the elastically scattered electrons show a peak at zero energy loss. The positive region shows the intensity of electrons that loose energy during the scattering on the surface. The inset of Fig. 3.7 shows that the peak of the elastically scattered electrons is the dominating feature in the spectrum. Because the position of the elastic peak indicates the incident energy, and usually much more pronounced than the other inelastic features in the spectrum, the elastic peak serves as the energy reference in the spectrum. The top x-axis of Fig. 3.7 shows the real kinetic energy of the electrons detected.

In Fig. 3.7, two kinds of excitations can be specified in the low energy energy loss region. One locates at about 50 meV, where the peak in the $I_\downarrow$ spectrum is much higher than that in $I_\uparrow$. This peak is ascribed to the spin-dependent excitations. As it will be shown in the next chapter, this peak is due to the spin wave excitations. The spin-dependent excitations may also show small peaks in the $I_\uparrow$ spectrum, which

can be attributed to the incomplete polarization of the incident electron beam and the magnetic state of the sample (Sec. 3.2.3, Sec. 3.3.1). It is interesting that a small gap between the $I_\downarrow$ and $I_\uparrow$ spectra can be observed in the energy gain part (negative region in Fig. 3.7). In this energy gain region, the $I_\uparrow$ spectrum is higher than the $I_\downarrow$ spectrum, which is attributed to the annihilation of the thermal excited spin waves. In this case, only the incidence of spin up electrons (whose spin is parallel to that of majority electrons) can destroy spin waves by compensate a spin flip in the system. Therefore, this process can be only found in the $I_\uparrow$ spectrum. As the intensity of the annihilation process is much lower than the creation process for the high wave vector spin waves studied in this work[1], we focus our attention on the spin wave peaks in the energy loss region.

There is another excitation showing almost same peak height at about 120 meV in both $I_\uparrow$ and $I_\downarrow$ spectra. It is attributed to the vibrational excitations of hydrogen atoms adsorbed on the sample surface [83]. As their scattering processes are mediated by the electric dipolar interaction, the electrons with different spins are not distinguishable. Hence, the energy loss peak due to the vibrational excitations are of the same intensity in both spectra[2].

3.3 Ultra thin Fe films on W(110)

Ultra thin Fe films on W(110) single crystal have been the subject of many studies in the last few decades [3–22, 85]. Many advanced techniques, such as the spin-polarized STM, Mössbauer spectroscopy, and angular resolved photoelectron spectroscopy, have been applied in the studies. In this section, the results selected from the previous studies are briefly reviewed, concerning the structure, morphology and magnetic properties of the Fe films on W(110). For the interest of this study, we mainly focus on the results for the Fe films prepared at room temperature. In the last part, the preparation and characterization of the Fe films studied in this work are also presented and compared with the previous results.

In this work, the word "monolayer" (ML) is defined as the unit of film thickness. It means an atomic layer with the atomic density same as that of W(110) surface, 1 ML=1.41×10^{15} atoms per cm^2. Due to the relaxation in the thicker films (>1.5 ML), the thickness denoted by ML is numerically larger than the real coverage of Fe on the surface. Assuming that the first Fe atomic layer is still pseudomorphic, and the higher layers are all relaxed [10], the real coverage can be estimated by $\theta = 0.82(\mathrm{D}-1)+1$. The factor 0.82 comes from the fact that the surface atomic density of W(110) is 82% of that of Fe(110). θ is the real thickness of the Fe film in real atomic layers, and D is

[1]For high wave vector spin waves studied in this work, the probability ratio of the spin wave annihilation and creation is mainly determined by the Boltzmann factor $\exp(-\hbar\omega/\mathrm{k}_B\mathrm{T})$ [59]. At room temperature, the intensity ratio varies from 0.25 to 0.14 for the spin wave energy from 30 meV to 70 meV. The peak of the annihilation process will be relatively higher for low energy spin waves. In this case, the excitation peaks are close to the elastic peak, which is difficult to be resolved.

[2]When the scattered electrons are measured close to the specular direction, the dipolar scattering may be interfered with the exchange process on a ferromagnetic surface, which causes a spin-dependent feature[84]. As our measurements are done in far off-specular geometry, the asymmetry due to this effect is not observed.

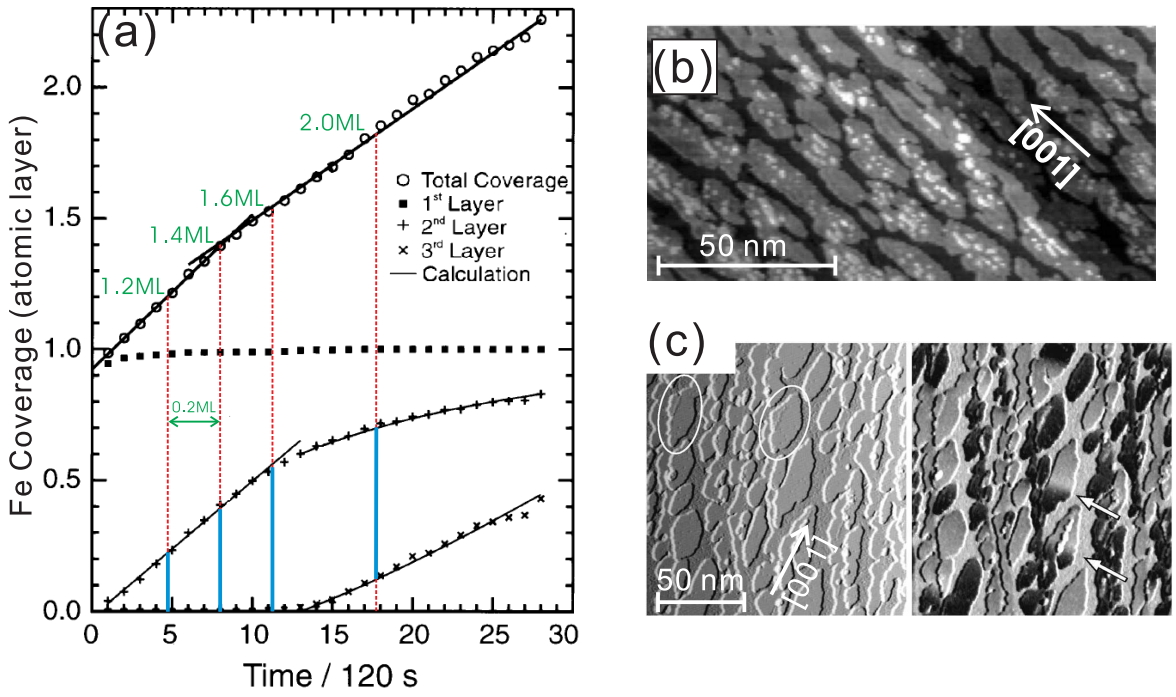

Figure 3.8: (a) The variation of the coverages for the first, second and third Fe atomic layers grown on W(110), which is taken from the STM study in Ref. [10]. The thicknesses of 1.2 ML, 1.4 ML, 1.6 ML and 2.0 ML, are indicated by the red lines in (a), which will be discussed in Sec. 4.2. The length of the blue bars indicates the coverage of the double layer patches. (b) is the STM image taken from Ref. [10] for an Fe film of about 1.7 ML. The distribution of the first layer (dark), the second layer (gray) and the third layer (white) can be observed directly. (c) shows the STM image (left) and the simultaneously recorded dI/dU map (right) taken from Ref. [12] for the Fe film of 1.6 ML, which are measured at 15 K using a spin-polarized STM. The dislocation lines are observed in the double lay patches as indicated by the two ovals in the left image. The domain walls are marked by the arrows in the right dI/dU map.

the amount of Fe deposited in the unit of ML.

3.3.1 Structure and magnetic properties

Structure

Despite of the large lattice mismatch (9.4%, η=(a_W-a_{Fe})/a_W) between Fe (a_{Fe} = 2.866 Å) and W (a_W = 3.165 Å), the first Fe monolayer (ML, 1 ML=1.41×10^{15} atoms per cm^2) is pseudomorphic on W(110). The relaxation starts at 1.2 ML [17, 18]. The STM study also demonstrates that the relaxation happens below the coverage of 1.5 ML [10]. As the result of the relaxation, the one dimensional dislocation lines are formed along the [001] direction in the double layer islands, which aslo serve as the nucleation sites for the third atomic layer [10]. Fig. 3.8 (c) shows the STM topography of the 1.6 ML Fe film. The dislocation lines can be seen in the left image of Fig. 3.8 (c) as indicated by the two white ovals. When the third layer islands start to coalesce at about 1.8 ML, the two dimensional dislocation networks appear in the third layer islands [9, 10]. For a

4 ML Fe film, the two dimensional dislocation network is observed with the modulated structure of 36 Å in the [001] direction and 51 Å in the [1$\bar{1}$0] direction [19]. The two dimensional dislocation network can be observed up to the thickness of 11 atomic layers[9]. It was reported that the first ML is not affected by the relaxation of the adlayers. The interface between the strained and relaxed layers lies between the first and second atomic layers [10].

Due to the large lattice mismatch, the inter-layer distances in the Fe films are different from that in bulk. For 1.7 ML Fe/W(110), the inter-layer distance between the first Fe ML and the W surface shows a contraction of 8% comparing to the layer spacing in bulk W. The spacing between the first two Fe atomic layers is about 11% smaller than that of bulk Fe [18].

Morphology

For the Fe films prepared at room temperature, isolated small islands are initially formed on the substrate in the sub-monolayer coverage. They begin to coalesce at about 0.6 ML [5, 9, 10]. The second ML starts to grow when the first ML has already covered almost 90% of the substrate [10]. Around 1.5 ML, the nucleation of the third atomic layer can be observed, and the third atomic layer islands start to coalesce at the film thickness of about 1.8 atomic layers [10]. Fig. 3.8(a) shows the coverages of the first three atomic layers during the growth of Fe film, which is obtained from the time-resolved STM study [10]. The film thicknesses of 1.2 ML, 1.4 ML, 1.6 ML and 2.0 ML are marked by the red dashed lines. The coverage of the double layer regions is denoted as blue bars.

The growth of the second layer islands is not isotropic. The islands are elongated in the [001] direction as shown in Fig. 3.8 (b) and (c) [10, 12]. At the coverage of 1.7 atomic layers (Fig. 3.8(b)), the islands are about 20-100 nm long and 7-20 nm wide.

Magnetic properties

The magnetic properties of the Fe thin films on W(110) are closely related to the film structure, morphology. For the Fe films less than 1 ML, due to the coalescence of the discrete monolayer islands at 0.6 ML, a sudden increase of the magnetization along [1$\bar{1}$0] is observed in the MOKE measurements [5]. The Curie temperature (Tc) of the Fe film at this coverage is about 190 K, and it increases to about 220 K when the first monolayer is nearly complete [3, 8].

For the film thickness between 1 and 2 atomic layers, the double layer islands show out-of-plane magnetization at low temperature [15, 86, 87]. The islands are coupled via magnetostatic interaction and show the antiferromagnetic ordering. At 15 K, this order can be observed up to 2.1 atomic layers using the spin-polarized STM [12]. The right image in Fig. 3.8(c) shows the dI/dU map of 1.6 ML Fe/W(110) measured by the spin-polarized STM [12]. The magnetic domains showing up and down magnetizations can be distinguished. The domain walls can be observed in the double layer islands (marked by the arrows), which are identified as the Bloch walls with the wall width of 7$\pm$1 nm [12].

At room temperature, the double layer islands in the 1.5 ML Fe film reveal a superparamagnetic behavior with the out-of-plane anisotropy [86, 88]. The magnetic property of the Fe film can be easily influenced by the surface contamination. The exposure of 1 Langmuir residue gas will switch the anisotropy from the out-of-plane to the in-plane [1$\bar{1}$0] direction [88]. The magnetization in the film also experiences

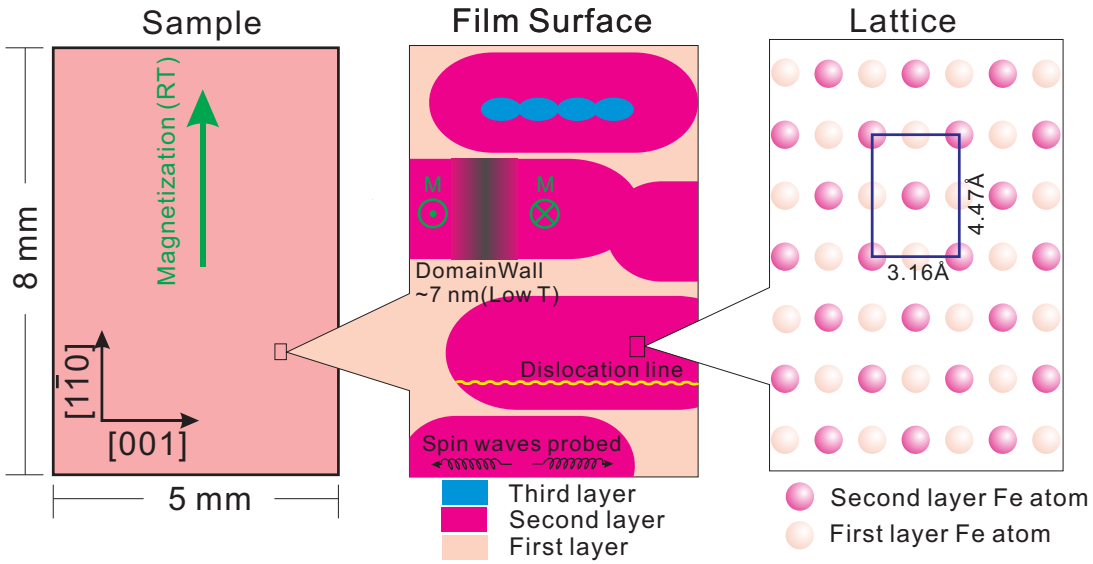

Figure 3.9: The schematic illustration of the surface morphology, magnetic properties and probing direction of the spin waves for a 2 ML Fe film. From left to right, the graphs are zoomed in step by step, showing the dimensions of the macroscopic sample, the double layer Fe patches and the atomic lattice. The directions of the domain wall, dislocation lines, and the propagation of spin waves are shown in the middle graph.

the same reorientation when the film thickness reaches about 2 ML [87, 89]. As the thickness of the Fe film increases further, the magnetization remains along the in-plane [1$\bar{1}$0] direction. Another magnetization reorientation happens at the thickness of about 40 ML, where the easy axis switches from the [1$\bar{1}$0] to [001] direction [90].

For the 1 ML and 2 ML Fe films, the temperature dependence of the magnetization around Tc can be described by the two dimensional Ising model [7, 91]. Ising like critical behavior is also observed in the study of the susceptibility of the film near the Curie temperature [92], in which the Tc of 2 ML Fe/W(110) is determined to be around 450K.

The morphology and magnetic properties of the 2 ML Fe film are summarized and schematically shown in Fig. 3.9. Along the [001] direction, the double layer Fe islands are elongated, and dislocation lines are formed. In addition, the spin waves are probed along this direction as well. The magnetization easy axis is along the [1$\bar{1}$0] direction at room temperature, and the domain wall is also along the same direction at low temperature [12].

3.3.2 Preparation and characterization

The substrate used in this work is a single W(110) crystal with the dimension of 8 mm×5 mm×0.3 mm (l×w×h). The [1$\bar{1}$0] direction of the tungsten crystal is parallel to the main axis of the spectrometer, as has been shown in Fig. 3.6. In order to clean the tungsten surface, the crystal is treated by cycles of annealing to 1600 K in an oxygen atmosphere (5×10^{-8} mbar), and a subsequent flash up to 2200 K. The chemical

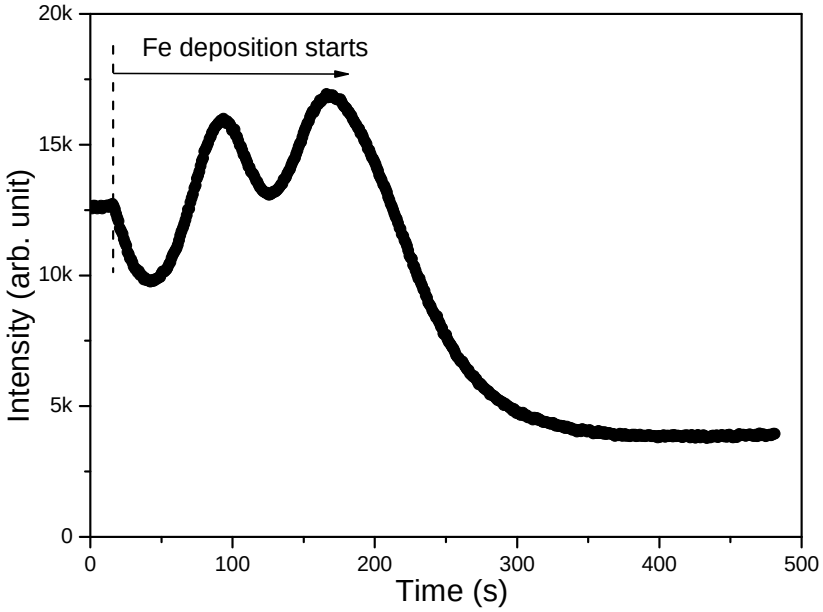

Figure 3.10: The MEED intensity measured during Fe deposition on W(110) at 115 K. The two peaks suggest the layer-by-layer growth of the first two Fe layers on the substrate, with which the depositing rate can be estimated.

purity of the surface is checked by the Auger electron spectroscopy. The cleaning process is repeated until no carbon is detected. Finally, the LEED shows typical pattern of a clean bcc (110) surface as demonstrated in Fig. 3.12).

Before each deposition of Fe, the tungsten substrate is flashed to about 2000 K to remove the adsorption or Fe adlayers. The Fe is deposited with a deposition rate of about 0.7 ML/min at room temperature. The pressure is not higher than 8×10^{-11} mbar during the deposition. For the preparation of 1 ML Fe/W(110), the sample is annealed up to about 900 K, which makes the Fe atomic layer smooth and homogeneous. A slight annealing (at 450 K for about 30 seconds) is also applied on the 24 ML Fe film in order to improve the surface quality. The Fe films of other thicknesses are not annealed after the deposition of Fe.

The deposition rate is firstly calibrated by the MEED oscillations at the temperature of 115 K, as shown in Fig. 3.10. During the deposition of Fe, the intensities of the diffraction spots are monitored. In the case of a layer-by-layer growth, the spot intensity may show oscillations with the period equal to the time of one layer growth [93]. As has been introduced previously, the growth mode of Fe on W(110) is quite complicated for the first several atomic layers. The growth of Fe at low temperature shows only two peaks in the MEED measurement. The deposition rate of Fe is calculated from the two oscillations, which is also checked by the MOKE measurements.

The MOKE measurements are performed in the longitudinal geometry with the magnetic field applied along the $[1\bar{1}0]$ direction. Fig. 3.11 (a) shows the hysteresis loops for the Fe films of different thicknesses. The square hysteresis loop for the 1 ML Fe film is obtained at the temperature of 120 K. At room temperature the MOKE measurement for the Fe film of 1.6 ML shows no hysteresis loop. This agrees with the previous studies, in which the double layer islands in the film of about 1.5 ML

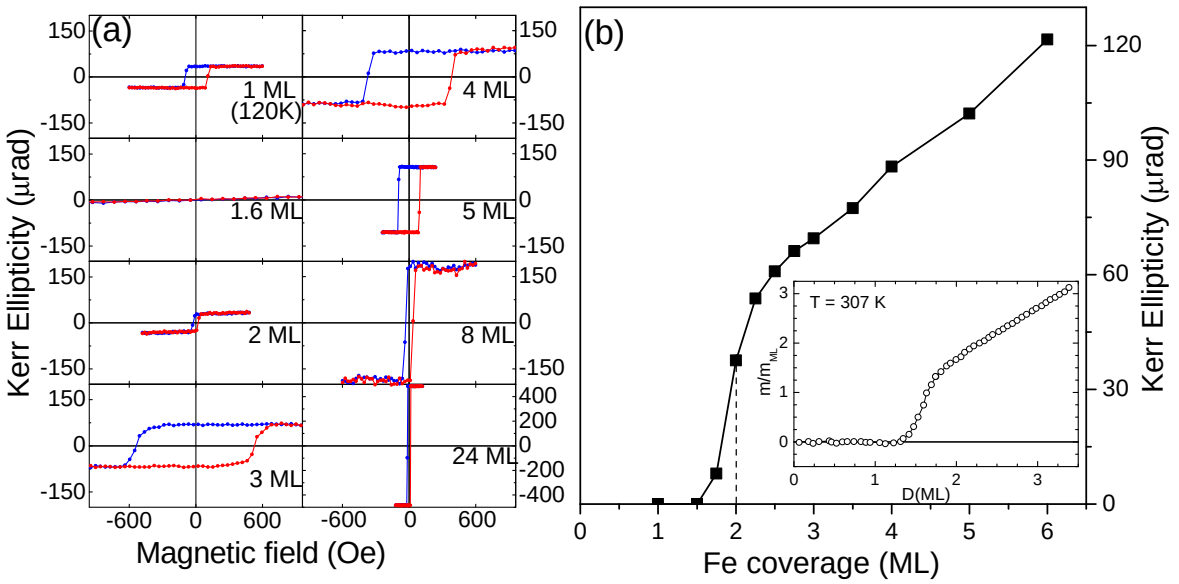

Figure 3.11: (a) shows the magnetic hysteresis loops measured by longitudinal-MOKE along the $[1\bar{1}0]$ direction. The hysteresis loop for 1 ML Fe film is measured at 120 K. Thicker films are all obtained at room temperature. (b) Kerr ellipticity versus the Fe film thickness measured by MOKE. At room temperature, the magnetization appears when the film is at about 2 ML thick. This is in good agreement with that observed in Ref. [89] as shown in the inset of (b). Note that the unit of Fe thickness in the inset graph is defined as the bulk Fe(110) surface. The appearance of the magnetization occurs at D = 1.64, which corresponds to 2 ML in our definition.

are proposed to be with the perpendicular anisotropy, and in the supperferromagnetic state at room temperature [88, 94]. The square hysteresis loops for the films thicker than 3 ML indicate that the magnetizations in these films are almost saturated in the remanent state.

The Kerr ellipticity at zero field is plotted as a function of the film thickness in Fig. 3.11 (b). The sudden increase of the Kerr signal occurs at about 2 ML. Then the Kerr ellipticity increases almost linearly as the film becomes thicker. The thickness dependence of magnetization in the Fe film has been studied using the torsion oscillation magnetometry (inset of Fig. 3.11 (a)) in the previous study [89]. Our results from the MOKE measurements are in good agreement with the previous study, in which the appearance of the magnetization is also at about 2 ML[3]. The uncertainty of the film thickness due to the preparation is estimated to be within 10%.

Obviously, the Kerr ellipticity for the 2 ML Fe film deviates from the linear relation and shows a lower value, which indicates that the magnetization in 2 ML Fe is not saturated at the zero magnetic field. This may be attributed to some small islands in the 2 ML Fe film, which are still in the supperferromagnetic state with the perpendicular anisotropy.

The hysteresis loop for 3 ML Fe shows the largest coercivity among these samples.

[3]The Fe thickness in the inset is in unit of a bulk Fe(110) atomic layer. D=1.64 corresponds to 2 ML in our definition.

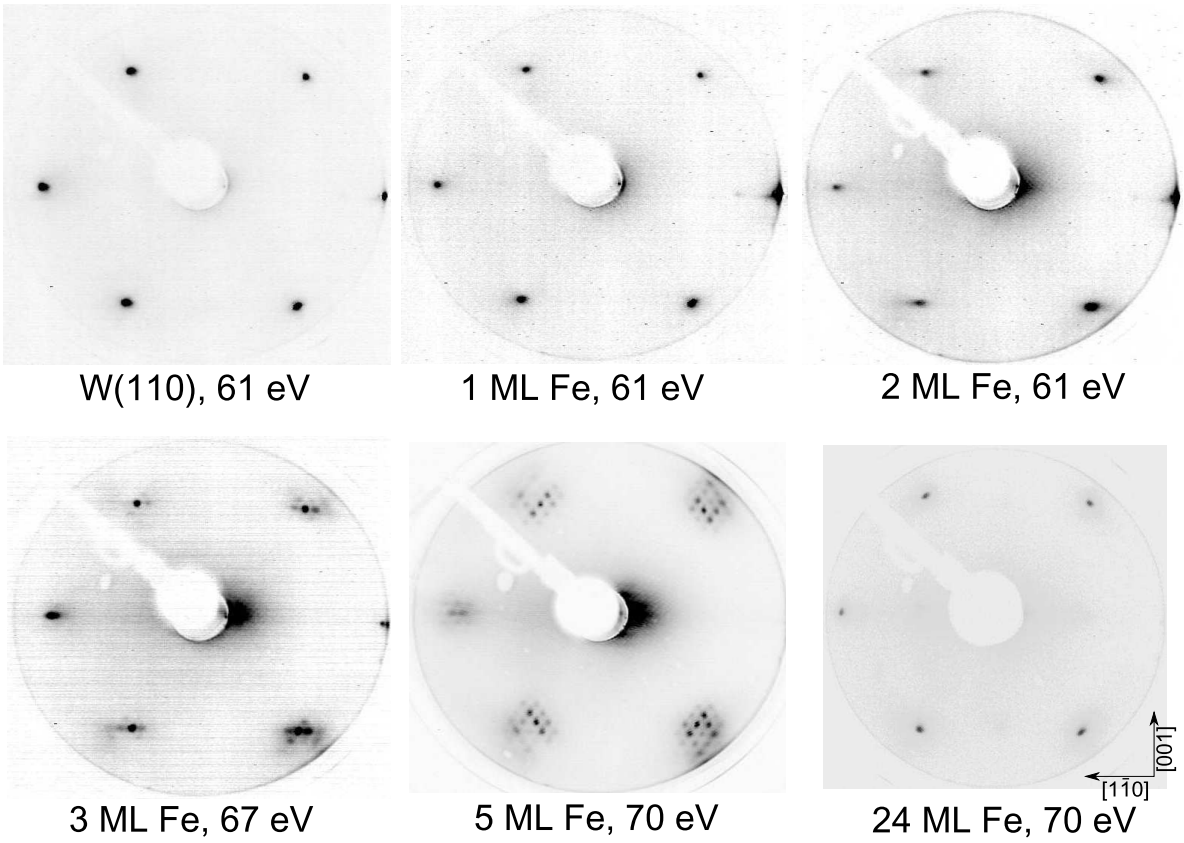

Figure 3.12: The LEED images of the Fe films on W(110) for different thicknesses. These results are in very good agreement with the previous studies [85].

The coercivity drops down fast as the film thickness increases. This observation may be attributed to the pinning of the domain walls at the boundaries between the regions of different thicknesses [16]. In these regions, the domain wall energies are different due to the influence of surface and interface [16]. During the switch of magnetization, the propagation of domain walls may be stopped at the region boundaries due to the difference of energy. This energy difference decreases fast as the films become thicker. Hence, the coercivities due to the domain wall pinning become smaller in thicker films.

The thickness calibration of Fe film is also checked by comparing the LEED patterns to the previous study [85]. The LEED patterns for the Fe films of different thicknesses are shown in Fig. 3.12, which are in quite good agreement with the study in Ref. [85]. The (1×1) bcc-Fe(110) diffraction patterns for the 1 ML and 2 ML Fe samples confirm the pseudomorphic structure of the Fe films. The pattern for the 3 ML Fe film shows the satellite spots, which indicate the formation of two dimensional dislocation networks in the film [9, 10]. The typical satellite spots due to the dislocation networks can be observed in the LEED pattern for the 5 ML Fe film. For the 24 ML Fe film, the LEED image shows clear (1×1) bcc (110) pattern again, which indicates that the dislocations on the surface already disappear, and the Fe(110) surface is of a good quality.

Chapter 4

Results

In the first part of this chapter the SPEEL-spectra for 2 ML Fe film on W(110) measured at room temperature are presented. Pronounced spin-dependent excitations are observed showing a clear dispersion relation for the in-plane wave vector transfer from 0.3 $Å^{-1}$ to 1.5 $Å^{-1}$. The films of lower Fe coverage (0.8 ML to 1.6 ML) are studied as well. The results are presented in the second section for comparison. In these films the spin wave excitations are observed to be very similar to those in the 2 ML Fe film.

The SPEELS experiments for 1 ML Fe/W(110) are performed at low temperature of about 120 K. It will be shown that the spin-dependent excitations exhibit broad peaks in the spectra, which suggests a strong decaying of the magnetic excitations.

In the last section of this chapter, the experimental results for the Fe films thicker than 2 ML are presented. The spin wave excitations show asymmetric and broad peaks in the spectra, which are similar to that observed previously [24]. More details can be observed in the spectra of low wave vectors, which enables us to compare our experimental results with the theoretical calculations [27].

4.1 SPEELS measurements for 2 ML Fe/W(110)

Fig. 4.1 (a) shows the SPEEL-spectra measured for 2 ML Fe film. The incident electron energy is 4 eV. The in-plane wave vector transfer ($\Delta K_{||}$) is 0.6 $Å^{-1}$, as determined by the scattering geometry according to Eq. 3.1. In the $I_{\downarrow}$ spectrum, a pronounced spin-dependent peak can be observed at the energy loss of 66 meV. This peak is attributed to the spin wave excitations. The excitation also shows a clear dispersion relation. As has been discussed in Sec. 3.2.1 for the scattering of electrons, the spin waves can be only created by the spin down electrons. Therefore, the spin wave features only exist in the $I_{\downarrow}$ spectrum. One can also observe a small peak at the same energy in the $I_{\uparrow}$ spectrum. It results from the incomplete polarization of the incident electrons, which is about 72%. In the spin up electron beam, the small percent of the spin down electrons, about 14%, can also create spin waves, which cause the peak in the $I_{\uparrow}$ spectrum. In addition, the magnetization of 2 ML Fe film is not completely saturated in the remanent state, indicated by the MOKE measurements shown in Fig. 3.11. As some magnetic domains are not aligned along the $[1\bar{1}0]$ direction in the SPEELS measurement, the spin up electron beam is not fully polarized with respect to the magnetization in these domains. The spin polarization of the electron beam could be much lower than 72%.

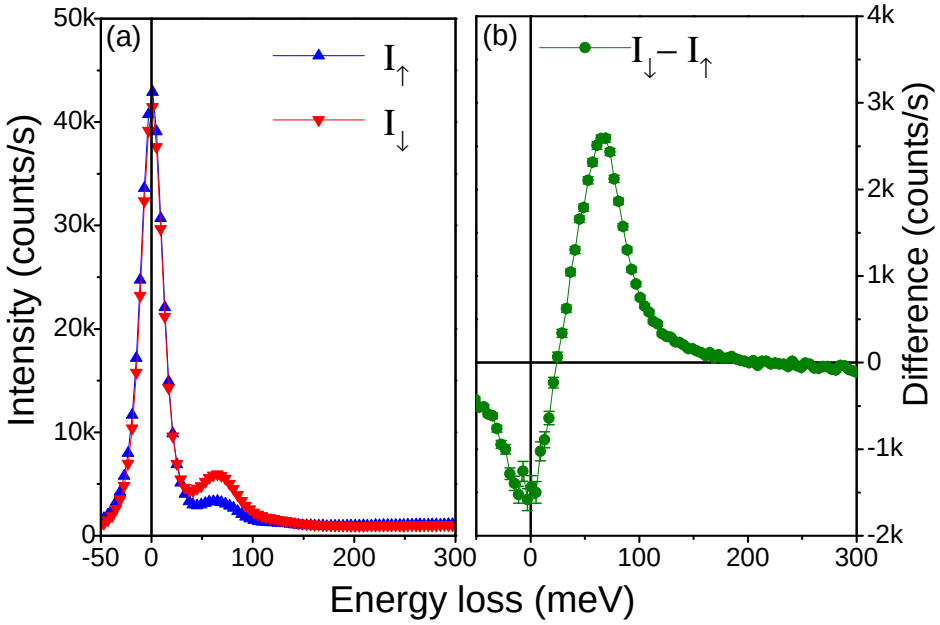

Figure 4.1: (a) The SPEEL-spectra for 2 ML Fe/W(110) with the in-plane wave vector transfer of $\Delta K_{||} = 0.6$ Å^{-1}. The incident electron energy is 4 eV, and the energy resolution is FWHM≈20 meV. The intensity spectrum $I_\uparrow$ ($I_\downarrow$) is obtained using the electrons with the spin parallel (antiparallel) to the spin of majority electrons in the Fe film, which is denoted by the blue up-triangles (red down-triangles). The difference spectrum ($I_\downarrow$-$I_\uparrow$) is shown in (b).

Therefore, when electron beam is spin up state along the $[1\bar{1}0]$ direction, additional spin waves can be excited in these regions, and gives rise to the spin wave peak in the $I_\uparrow$ spectrum. The spectra shown in this work are not calibrated by the spin polarization of the incident beam.

Fig. 4.1 (b) shows the difference spectrum ($I_\downarrow$-$I_\uparrow$). In the difference spectrum, those peaks induced by the non-spin-dependent excitations, such as the vibrational peaks, are almost canceled out. Only the spin wave peak is maintained and becomes the dominating feature. The spin wave excitation show a quite well defined peak. As the background in the high energy loss region is quite small, the spin wave energy and the full width at half maximum (FWHM) can be directly obtained from the peak in the difference spectrum without further fitting procedures[1]. The area under the excitation peak is regarded as the spin wave intensity[2].

Due to the exchange process and spin-orbit interaction in the scattering, the elastic peaks in the $I_\uparrow$ and $I_\downarrow$ spectra are usually not equal. This results in a pronounced peak in the difference spectrum at zero energy loss (see 4.1 (b)). The spin wave peak will be overlapped with this peak, when its energy is low (<30 meV). In this case,

[1]The fitting procedures using the Gaussian or Loretzian distributions have been also performed. The energies and FWHMs obtained in the fittings are close to the values that are measured directly. The difference is smaller than the experimental errors.

[2]This quantity is obtained by integrating the area under the excitation peak in the difference spectrum. The part of the spectra showing negative intensity is neglected.

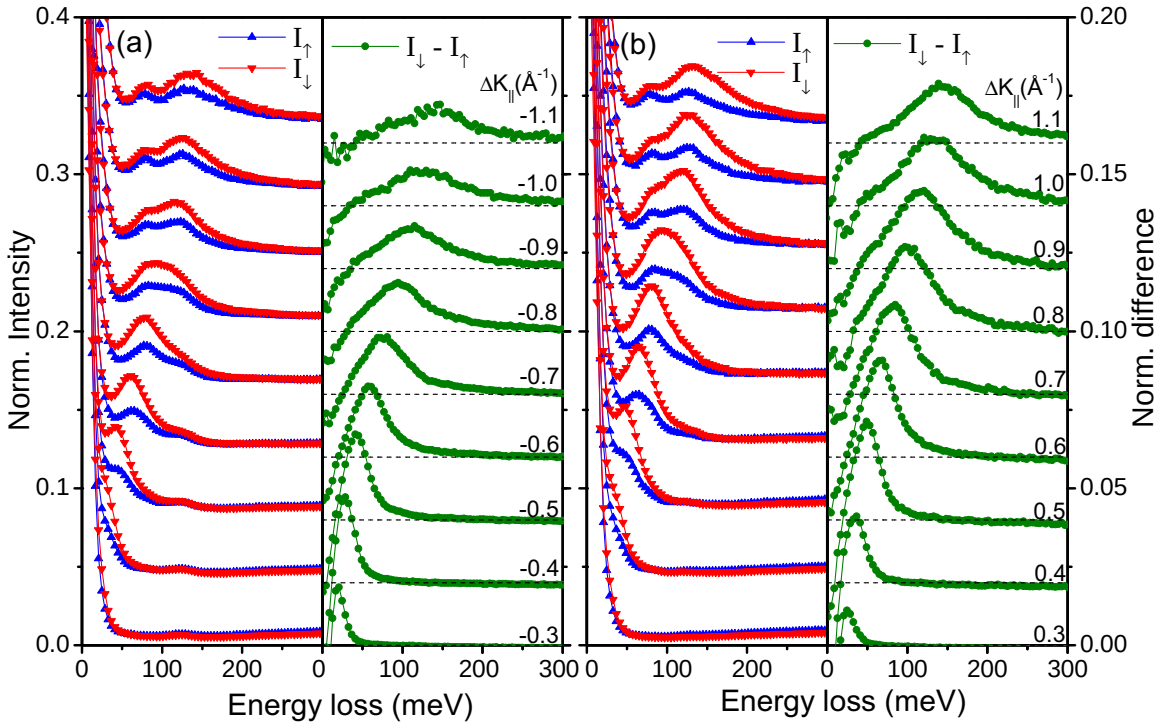

Figure 4.2: The normalized SPEEL-spectra $I_\uparrow$ (blue up-triangle), $I_\downarrow$ (red down-triangle) and their difference, $I_\downarrow$-$I_\uparrow$ (green dot) for 2 ML Fe film. The incident electron energy is 4 eV with the energy resolution FWHM≈20 meV. The wave vector transfer $\Delta K_{||}$ is from -1.1 Å^{-1} to -0.3 Å^{-1} in (a) and from 0.3 Å^{-1} to 1.1 Å^{-1} in (b). For each $\Delta K_{||}$, the $I_\uparrow$ and $I_\downarrow$ spectra are normalized with respect to the elastic peak maximum in ($I_\uparrow$+$I_\downarrow$). The difference spectrum, $I_\downarrow$-$I_\uparrow$, is obtained from the normalized $I_\uparrow$ and $I_\downarrow$ spectra. To show clearly the spectra all together, the spectra are presented in a waterfall form, in which an artificial offset is set between each spectrum.

the direct measurements of the spin wave energy, FWHM and the peak area will large errors. The errors can be estimated by the following procedure [68]. The $I_\uparrow$ spectrum is artificially scaled, so that the elastic peaks in $I_\uparrow$ and $I_\downarrow$ have the exactly same intensity. The two elastic peaks are cancelled out in the new difference spectrum. The spin wave peak is assumed to be less modified by the elastic peaks, and close to its original shape in the new difference spectrum. The spin wave energy, FWHM and the peak area obtained from the new difference spectrum are compared with the values from the direct measures. The difference of the values obtained from the two methods is indicated by error bars.

The dispersion relation of the spin waves is obtained by measuring the excitation peaks for a series of $\Delta K_{||}$. The results for 2 ML Fe film are shown in Fig. 4.2. The $I_\uparrow$ and $I_\downarrow$ (blue and red triangles) spectra and the difference spectra (green dots) are presented for $\Delta K_{||}$ changing from -1.1 Å^{-1} to -0.3 Å^{-1}(a) and from 0.3 Å^{-1} to 1.1 Å^{-1} (b), respectively. The experimental scattering geometries for the negative and positive $\Delta K_{||}$ have been illustrated in Fig. 3.2.

The SPEEL-spectra show that the intensity of the spin wave excitation drops more

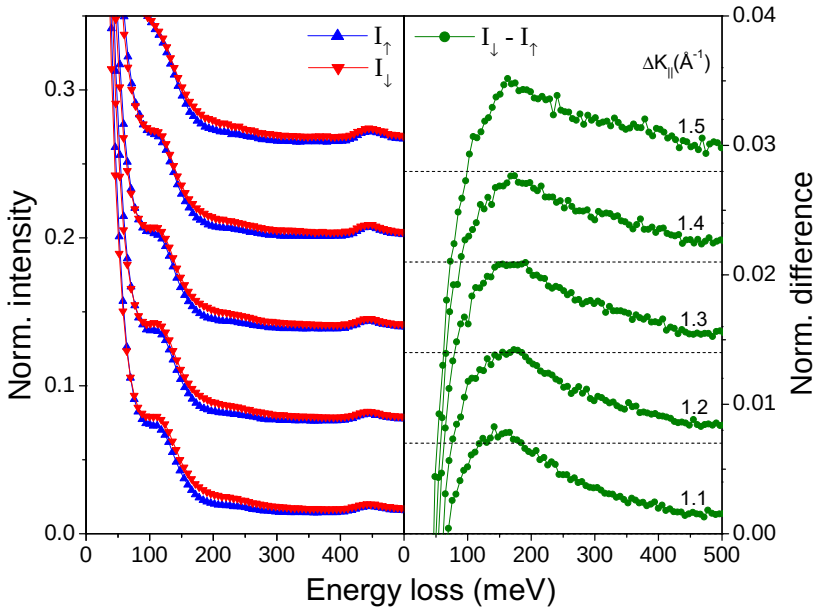

Figure 4.3: The normalized SPEEL-spectra $I_\uparrow$, $I_\downarrow$ and the difference spectra for 2 ML Fe film with in-plane wave vector transfer $\Delta K_{||}$ from 1.1 $Å^{-1}$ to 1.5 $Å^{-1}$. The incident electron energy is 6.75 eV, and the energy resolution is FWHM $\approx$ 45 meV.

than one order of magnitude (see Fig. 4.5 (b)) as the $|\Delta K_{||}|$ increases from 0.3 $Å^{-1}$ to 1.1 $Å^{-1}$. In order to show all excitation peaks clearly for different $\Delta K_{||}$, the intensity spectra are normalized using the following procedure. For a certain $\Delta K_{||}$, the maximum of the elastic peak in the $(I_\uparrow+I_\downarrow)$ spectrum is taken as the normalization factor. For this $\Delta K_{||}$, the $I_\uparrow$, $I_\downarrow$ spectra and their difference spectrum are divided by this factor. The normalized $I_\uparrow$, $I_\downarrow$ and difference spectrum are shown in Fig. 4.2 for each $\Delta K_{||}$.

The dispersion behavior can be observed directly from the excitation peaks in the normalized $I_\downarrow$ spectra in Fig. 4.2. It is more clear in the difference spectra, where the spin wave peak shifts from about 30 meV to 150 meV as $\Delta K_{||}$ increases from 0.3 $Å^{-1}$ to 1.1 $Å^{-1}$. The clear dispersion relation reveals the collective character of the observed spin-dependent excitations [45], and is taken as the evidence of the spin waves excitations [2]. According to the Heisenberg model discussed in Sec. 2.1, one would expect two spin wave modes, the acoustic and optical modes, in 2 ML Fe film. The spectra with large energy loss up to 600 meV were checked. However, the spin wave peaks in the spectra show clearly the single peak feature.

In the normalized $I_\uparrow$ and $I_\downarrow$ spectra in Fig. 4.2, one may notice two other excitation peaks at about 78 meV and 125 meV, which show little spin asymmetry. They become more and more pronounced in the spectra for high $\Delta K_{||}$. They may be attributed to the vibrational excitations of the hydrogen atoms adsorbed on the surface [83]. In the measurement of a series of spectra with different $\Delta K_{||}$, it usually takes at least 4 hours (the vacuum better than 4×10^{-11} mbar). To estimate the influence of the contamination during the SPEELS measurement, the first spectrum in the experiment was repeated at the end of the experiment. The change of spin wave peak position and width is very small, and is taken into account in the experimental errors. The influence of the adsorbate in the experiments is neglected in the discussions.

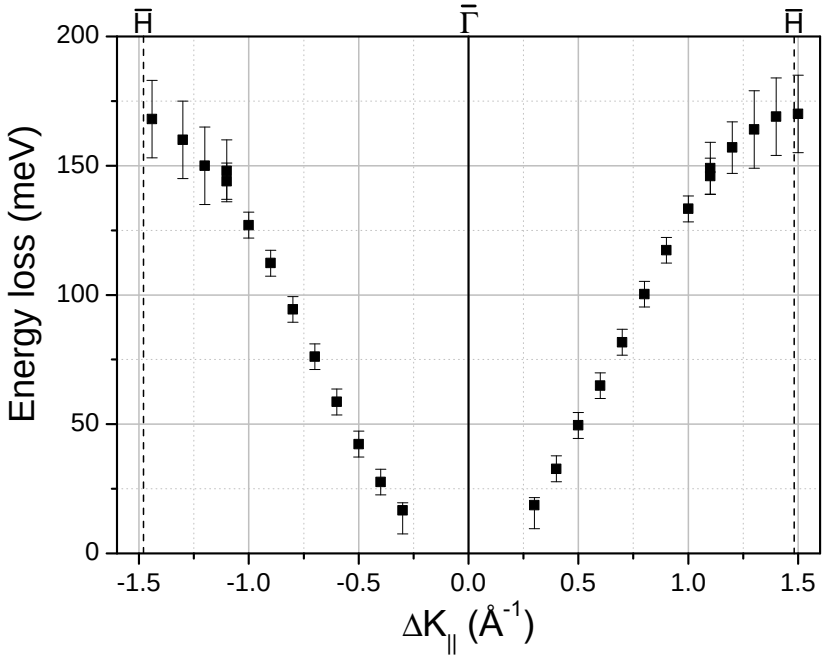

Figure 4.4: The experimentally determined spin wave dispersion in the 2 ML Fe film. Black squares denote energy positions of the spin wave peaks in the difference spectra shown in Figs. 4.2 and 4.3.

In the reciprocal space, the surface Brillouin zone boundary along the [001] direction locates at 1.49 $Å^{-1}$ for the pseudomorphic 2 ML Fe film on W(110). With the scattering angle of $\theta_0 = 80°$, this magnitude of wave vector can not be achieved using the incident electron energy of 4 eV. The measurements for higher $\Delta K_{||}$ are completed by using the electrons of a higher energy, i.e. 6.75 eV. The results for the $\Delta K_{||}$ from 1.1 $Å^{-1}$ to 1.5 $Å^{-1}$ are shown in Fig. 4.3. The spin wave peak position increases further from about 150 meV to 170 meV. For 1.1 $Å^{-1}$, the peak positions are consistent for the incident energies of 4 eV and 6.75 eV. The normalized difference spectra in Fig. 4.3 indicate that the heights of the spin wave peaks are about 1 percent of the elastic peaks for the incident energy of 6.75 eV. For the incident energy of 4 eV, this ratio is about ten times higher, which indicate that the cross section of spin wave excitations strongly depends on the incident energy. It is similar to the our previous observation on the Co films [23, 24, 70]. The theoretical studies indicate that the probability of an exchange scattering event that is necessary for the spin wave excitations, reduces for higher incident energy of the electrons [95]. However, the detail of the scattering event is still not understood at the moment, which is an issue under investigation.

The dispersion curve in the entire Brillouin zone is obtained by plotting the position of the excitation peak as a function of $\Delta K_{||}$. Fig. 4.4 shows the clear dispersion of the spin waves in 2 ML Fe film, which consists of two excellently symmetric branches in the positive and negative wave vector regions. The large uncertainty of the energy for the high $\Delta K_{||}$ data point is due to the low intensity and the broad energy distribution. One may also noticed that the branch in the negative wave vector region is slightly lower than one in the positive region. It may be due to the uncertainty of the elastic

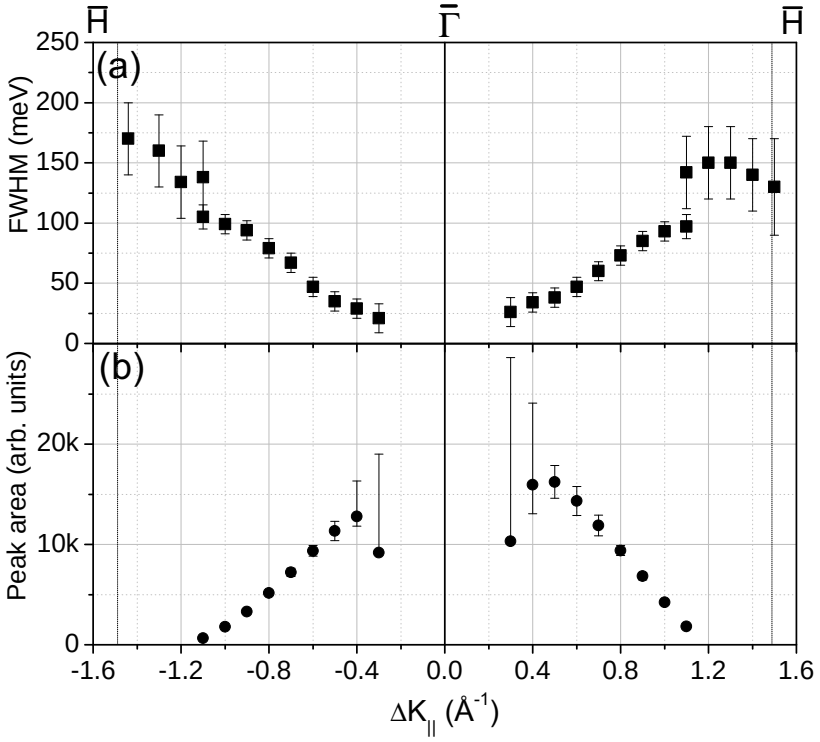

Figure 4.5: The widths (a) and peak areas (b) of the spin wave peaks in the difference spectra for 2 ML Fe film, as shown in Fig. 4.2 and Fig. 4.3. They are obtained from the direct measurements of the excitation peaks in the difference spectra.

peak positions, which determine the zero energy point. As the small shift is still in the experimental errors, it is not discussed in this work.

The peak widths (FWHM) of the spin wave excitations in the 2 ML Fe film are plotted versus $\Delta K_{||}$ in Fig.4.5 (a). The FWHMs for the spectra measured with the incident energy of 6.75 eV are estimated by fitting the spectra with a Loretzian function and a background described by a second order polynomial. Because of the uncertainty of the fitting procedure, the FWHMs for high wave vectors show large errors. The widths of the excitation peaks are numerically smaller than the corresponding excitation energies shown in Fig. 4.4. The FWHM increases from 20 meV to 170 meV, as $\Delta K_{||}$ increases from 0.3 $Å^{-1}$ to 1.5 $Å^{-1}$. This obvious broadening of the excitation peaks is attributed to the decay of the spin waves in the itinerant electron system [27]. It should be noted that the excitation peak obtained in the measurement is the convolution of the spin wave peak and the response function of the SPEEL-spectrometer. Assuming that the spin wave peak is the convolution of a Lorentzian and a Gaussian distribution, the intrinsic width of the spin wave peak can be estimated (see Sec. 5.2).

Fig. 4.5 (b) shows the wave vector dependence of the peak area of the spin wave excitation. This quantity strongly depends on the intensity of the incident electron beam. As the measurements for the high wave vectors are performed with a different electron beam intensity, the results are not shown for comparison. A small intensity difference between the data for the positive and negative $\Delta K_{||}$ is attributed to the different intensities of the incident electron beams in the two experiments. Because the

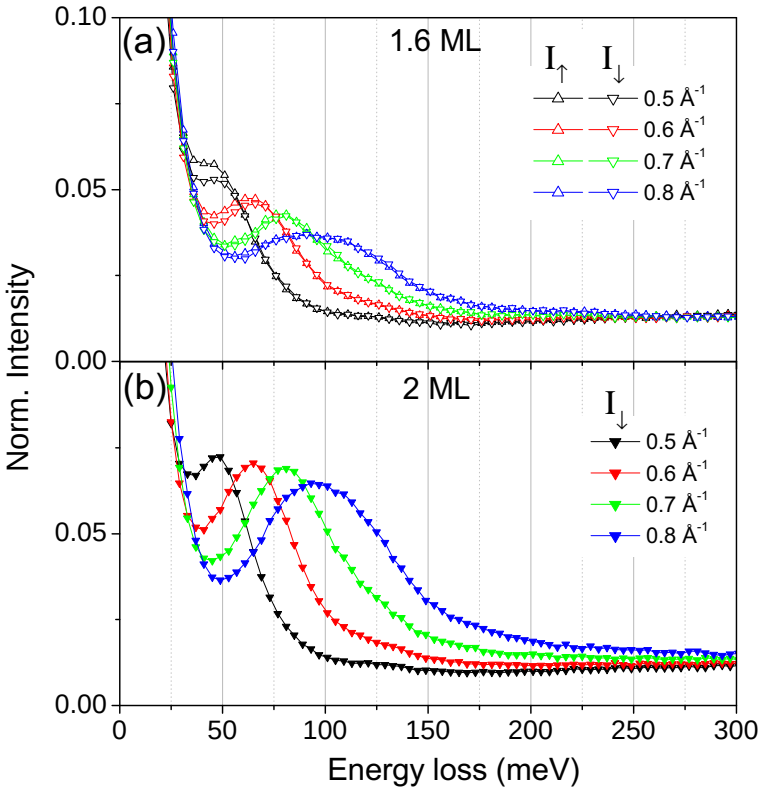

Figure 4.6: Comparison between the normalized SPEELS spectra for 1.6 ML Fe/W(110) and 2 ML Fe/W(110). (a) Normalized $I_{\uparrow}$ (open up-triangle) and $I_{\downarrow}$ (open down-triangle) spectra for 1.6 ML Fe/W(110) with $\Delta K_{||}$ from 0.5 $Å^{-1}$ to 0.8 $Å^{-1}$. The incident electron energy is 4 eV with FWHM $\approx$ 20 meV. For comparison, (b) shows the $I_{\downarrow}$ (filled down-triangle) spectra for 2 ML Fe/W(110) with the same $\Delta K_{||}$.

spin wave peaks of low $\Delta K_{||}$ ($\pm$0.3 $Å^{-1}$ and $\pm$0.4 $Å^{-1}$) are close to the elastic peaks, they are overlapped with a large negative difference caused by the elastic peak. The direct measures of the peak areas show relatively low intensities, and the errors are large. Despite of these data, the spin wave intensity drops quickly as $\Delta K_{||}$ increases. The intensity for $\Delta K_{||}$=1.1 $Å^{-1}$ is almost one order of magnitude smaller than that for low wave vectors ($\Delta K_{||}$=0.4 $Å^{-1}$). This reduction of the spin wave intensity has been also observed in the SPEELS studies of the spin waves in Co thin films, which indicates the decrease of the scattering cross section of the spin wave excitations at high $\Delta K_{||}$ [70, 71].

4.2 SPEEL-spectra for Fe films between 1 ML and 2 ML

The SPEELS results for the Fe films of 0.8 ML, 1.2 ML, 1.4 ML, 1.6 ML and 2.0 ML, are presented in this section. Spin wave excitations can be identified in the $I_{\uparrow}$ and $I_{\downarrow}$ spectra. It will be shown that the spin wave intensity is proportional to the area of the double layer regions, which proves that the observed spin wave signal is probed in these

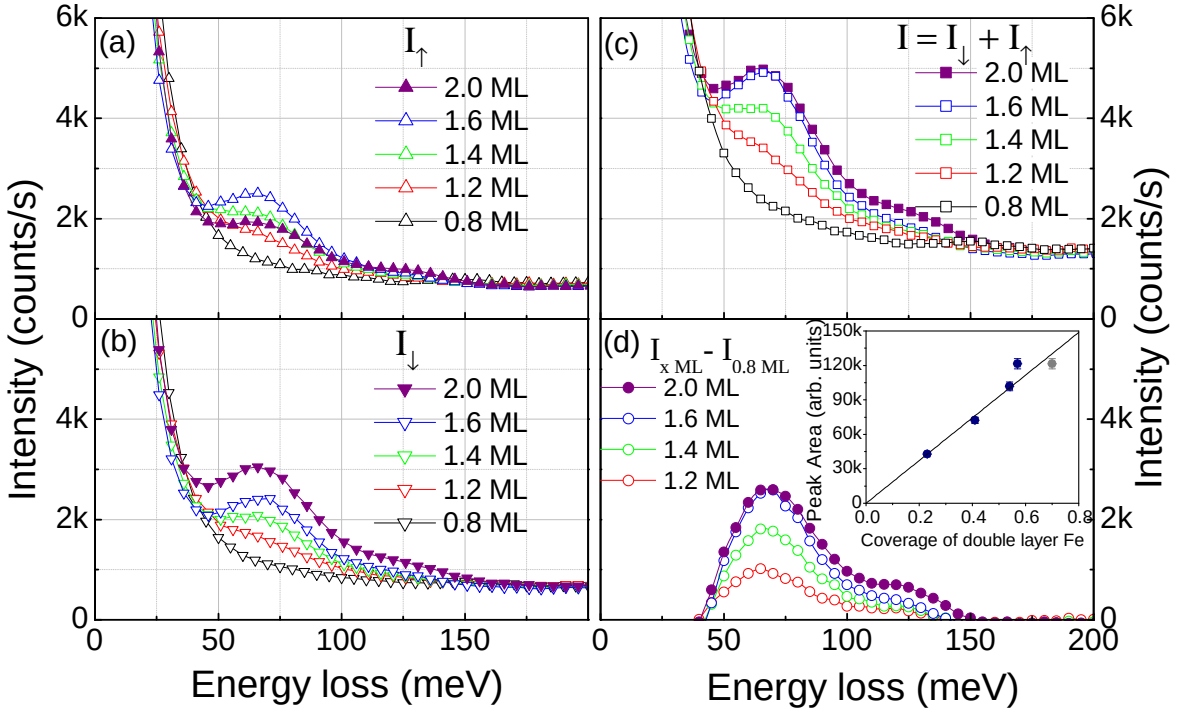

Figure 4.7: The SPEEL-spectra, $I_\uparrow$ (a) and $I_\downarrow$ (b), measured for 0.8 ML, 1.2 ML, 1.4 ML, 1.6 ML and 2.0 ML Fe on W(110). The incident energy is 4 eV with the resolution FWHM $\approx$ 20 meV, and the wave vector transfer in the experiments is fixed at 0.6 Å^{-1}. The total intensity spectrum ($I_\uparrow$+$I_\downarrow$) are shown in (c). (d) gives the spin wave peaks in the total intensity spectra $I_{x\ ML}$ (x> 0.8) by subtracting the spectrum $I_{0.8\ ML}$, which is taken as the background. The inset of (d) shows the linear relation between the spin wave peak areas and the coverage of the double layer regions (blue dots). The gray dot is the point representing the peak area for 2 ML Fe versus the total coverage of both the double layer and triple layer regions.

regions.

There is no external magnetic field applied on the sample during the SPEELS measurements. Therefore, the remanent magnetization of the Fe film defines a quantization axis for the spin of the incident electron. This is necessary for the observation of the spin wave signals in the difference spectrum. However, it has been shown in Fig. 3.11 that the Fe films thinner than 1.6 ML do not show remanent magnetization along [1$\bar{1}$0] at room temperature. The Fe film could be in a superparamagnetic state with the out-of-plane anisotropy [8, 86, 88][3]. In such a system, the probability of the spin wave excitations is same for the spin up and spin down electrons. The $I_\uparrow$ and $I_\downarrow$ spectra for these samples should show no difference for the spin wave excitations.

Fig. 4.6 (a) shows the normalized $I_\uparrow$ and $I_\downarrow$ spectra for the 1.6 ML Fe film with the in-plane wave vector transfers from 0.5 Å^{-1} to 0.8 Å^{-1}. Before and after the SPEELS

[3]Due to the contamination during the SPEELS experiments, some double layer Fe islands may finally switch to the an in-plane anisotropy [86, 88]. However, the MOKE measurement after the SPEELS measurements shows no remanent magnetization for the film. Therefore, the probability of the spin wave excitations is also same for both the spin up and spin down electrons.

measurements, the magnetic property of the sample was checked by MOKE, which confirmed that the sample showed no remanent magnetization. Pronounced excitation peaks with almost the same intensities can be observed in both $I_\uparrow$ and $I_\downarrow$ spectra for all $\Delta K_{||}$. They also show clear dispersion behavior as $\Delta K_{||}$ increases. The normalized $I_\downarrow$ spectra for 2 ML Fe/W(110) shown in Fig. 4.6 (b) are also plotted in Fig. 4.6 (b) for comparison. The positions and widths of the excitation peaks for the 1.6 ML Fe film are in very good agreement with the spin wave peaks observed on 2 ML Fe film. It strongly indicates that the excitation peaks for 1.6 ML are due to the spin wave excitations.

To confirm that, the SPEELS measurements were performed on the Fe films with the thickness varying from 0.8 ML to 2 ML. During the experiments, the SPEELS spectra were measured with a constant in-plane wave vector transfer, $\Delta K_{||} = 0.6$ Å^{-1}, while the film thickness was increased step by step from 0.8 ML to 2.0 ML. Before measuring the spectra for the 2 ML Fe film, the MOKE measurement was performed in order to align the magnetization to the $[1\bar{1}0]$ direction.

The $I_\uparrow$ and $I_\downarrow$ spectra measured for the Fe films of the thicknesses 0.8 ML, 1.2 ML, 1.4 ML, 1.6 ML and 2.0 ML, are presented in Fig. 4.7 (a) and (b). In Fig. 4.7 (a) and (b), an excitation peak becomes higher and higher at the energy of about 68 meV, as the film thickness increases from 0.8 ML to 2 ML. When the film thickness is less than 1.6 ML, the intensities of the excitation peak in both $I_\uparrow$ and $I_\downarrow$ spectra are almost the same. Once the film thickness reaches 2 ML, the excitation peak in the $I_\downarrow$ spectrum becomes much higher than that in the $I_\uparrow$ spectrum. Now, the spin-dependent excitation peak turns out to be as same as the spin wave peak observed in Fig 4.1 for 2 ML Fe/W(110). The evolution of the excitation peak with respect to the film thickness demonstrates that the excitation peaks observed in the films of 1.2, 1.4 and 1.6 ML Fe/W(110) are same as that observed on 2 ML Fe film, which is due to the spin wave excitations. Furthermore, a linear relation is observed between the spin wave intensity and the coverage of the double layer regions in the Fe films.

The coverages of the monolayer, double layer and triple layer regions on the surface for the thicknesses from 1.2 to 2 ML can be estimated from the STM study in Ref. [10] as shown in Fig. 3.8 (a). The corresponding film thicknesses are indicated by the red dashed lines, and the coverages of the double layer regions are marked by the thick blue bars. Tab. 4.1 shows the coverage of each region obtained from Fig. 3.8 (a). Due to the nucleation of the triple layer islands for the 2 ML film, the area of the double layer regions only increases slightly in comparison to that in the 1.6 ML film. It will be shown that this effect is also observed in the change of spin wave intensities.

The total intensity spectrum ($I = I_\uparrow + I_\downarrow$) is calculated for each film, which is shown in Fig. 4.7(c). The spectrum for the 0.8 ML Fe film, $I_{0.8\ ML}$, is treated as the background, and the spin wave peaks for the other films are obtained by subtracting $I_{0.8\ ML}$ from the spectra $I_{x\ ML}$ ($x > 0.8$), as shown in Fig. 4.7(d). The intensity of the spin wave peak at about 68 meV increases with the Fe coverage. On the right side of the spin wave peak, a small shoulder at about 120 meV is observed. It is attributed to the hydrogen vibrational excitations. By fitting the spin wave peaks at 68 meV with the Lorentzian distribution, the areas are obtained and also shown in Tab. 4.1.

In the inset of Fig. 4.7 (d), the area of the spin wave peak is plotted versus the coverage of the double layer islands for each thickness (blue dots). A clear linear relation is observed for the film thickness between 1.2 ML and 1.6 ML. It is straightforward to

Table 4.1: The coverage of monolayer (ML), double layer (DL) and triple layer (TL) patches measured from Fig. 3.8 (a) for the Fe films of 1.2 ML, 1.4 ML, 1.6 ML and 2.0 ML on W(110). The areas of the spin wave peaks are obtained from the spectra shown in Fig. 4.7 (d).

		1.2 ML	1.4 ML	1.6 ML	2.0 ML
Relative coverage of each regions	ML	0.75±0.01	0.58±0.01	0.45±0.01	0.30±0.01
	DL	**0.23±0.01**	**0.41±0.01**	**0.54±0.01**	**0.57±0.01**
	TL	0	0	0	0.13±0.01
Peak area (a.u.)		44679	76785	107886	118117

assume that the spin wave intensity is proportional to the coverage of the regions, where the spin waves are excited. The linear relation in the inset of Fig. 4.7 (d) thus demonstrates that the observed spin waves are excited in the double layer regions. The deviation of the last point, which corresponds to the film thickness of 2 ML, is ascribed to the non-linear increase of the double layer regions. However, if we consider the triple layer regions, as indicated by the gray data point in the graph, the linear relation is again fulfilled.

It also implies that the spin wave peaks in the SPEEL-spectra for 2 ML Fe consist of the contribution from the triple layer regions. It will be shown in Sec. 4.4 that the spin wave energies in the 3 ML Fe film are relatively lower than that in the 2 ML Fe film. Hence, in Fig. 4.7 (d), the spin wave peak for 2 ML Fe film is not enhanced too much in height, but becomes broader as compared to the peak for 1.6 ML Fe film.

4.3 SPEELS measurements for 1 ML Fe/W(110) at 120K

The STM images shown in Fig. 3.8 indicate that the 1.6 ML Fe film is composed of the monolayer and double layer regions [10, 12]. It is interesting that the magnetic excitations in the monolayer regions do not appear in the spectrum for the 1.6 ML Fe film. This may be attributed to the low Curie temperature of the 1 ML Fe film on W(110), which is about 220 K [3, 5]. For the measurement at room temperature, the well-defined spin waves unlikely exist in these regions [96]. To investigate the magnetic excitations in the monolayer regions, the 1 ML Fe film is prepared and cooled down to 120 K for the SPEELS measurements. It will be shown that the magnetic excitations observed are much softer than the spin wave excitations observed in the 2 ML Fe film.

The SPEELS experiments are performed at the low temperature of 120 K with $\Delta K_{||}$ from 0.3 $Å^{-1}$ to 1.0 $Å^{-1}$. The normalized intensity spectra and difference spectra are shown in Fig. 4.8. The magnetic excitations can be observed on the shoulder of the elastic peak in the $I_{\downarrow}$ spectra, where they cause noticeable gaps between the $I_{\downarrow}$ and $I_{\uparrow}$ spectra. These excitation peaks are more clear in the difference spectra, especially for $\Delta K_{||}$ <0.7 $Å^{-1}$. The magnetic excitations reveal a dispersion relation by shifting the peaks from about 20 meV to 60 meV as $\Delta K_{||}$ increases from 0.3 $Å^{-1}$ to 1.0 $Å^{-1}$. Furthermore, for the low wave vectors ($\Delta K_{||} < 0.5$ $Å^{-1}$), these difference spectra show

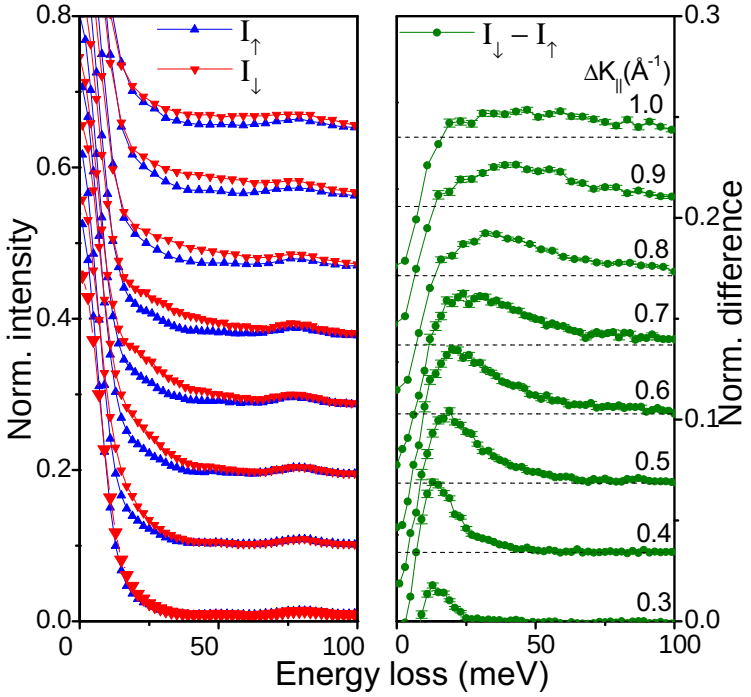

Figure 4.8: The normalized $I_{\uparrow}$ (blue up-triangle), $I_{\downarrow}$ (red down-triangle) spectra and their difference (green dot) for 1 ML Fe/W(110) with $\Delta K_{||}$ from 0.3 Å^{-1} to 1.0 Å^{-1} at 120 K. The incident energy is 3.8 eV with the energy resolution FWHM $\approx$ 15 meV.

very small background as compared to the excitation peaks observed, which is similar to the difference spectra observed for 2 ML Fe. The calculation based on the itinerant electron theory reveals that the spin waves with low wave vectors have a narrow energy distribution in the spectra, which is dramatically broadened in the high wave vector region [29]. The excitation spectra in Fig. 4.8 qualitatively resemble this behavior.

The energy positions of the excitation peaks in the difference spectra are plotted in Fig. 4.9 (a), where the dispersion behavior can be clearly observed. The highest energy of the excitations in 1 ML Fe/W(110) is around 60 meV for $\Delta K_{||}$ = 1.0 Å^{-1}. This is almost three times smaller than those observed on 2 ML Fe film. The FWHM of the excitation peaks in the difference spectra are shown in Fig. 4.9 (b). The peak width increases monotonically with $\Delta K_{||}$. The values of the peak widths are even larger than the corresponding excitation energies, which indicates the strong decay of the magnetic excitations.

4.4 Evolution of the SPEEL-spectra for thicker Fe films

The SPEELS measurements are also performed for the Fe films thicker than 2 ML. The normalized SPEEL-spectra for the 5 ML and 24 ML thick Fe films are shown in Fig. 4.10 and Fig. 4.11, respectively. Pronounced magnetic excitations can be observed in the SPEELS spectra for both films. For $\Delta K_{||}$ from 0.35 Å^{-1} to 0.7 Å^{-1}, pronounced

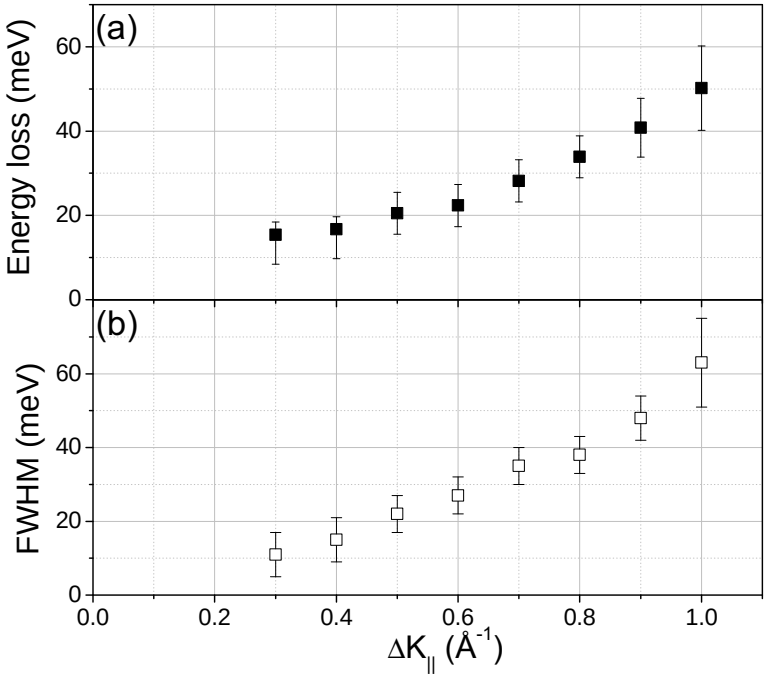

Figure 4.9: (a) The dispersion relation of the magnetic excitations in 1 ML Fe/W(110) obtained by taking the energy positions of the peak maxima in the difference spectra in Fig. 4.8. (b) The FWHM of the excitation peaks measured directly from the excitation peaks in difference spectra in Fig. 4.8.

excitation peaks can be observed between 20 meV and 80 meV in the difference spectra. They show a continuous energy shifting as $\Delta K_{||}$ increases, which indicates the dispersion behavior. The SPEELS spectra observed for the two Fe films show similar features at those in the 2 ML Fe film. There is a very small background as compared to the pronounced excitation peak in the spectrum for low $\Delta K_{||}$ (< 0.5 Å^{-1}). The pronounced excitation peaks mainly distribute in the energy loss range smaller than 100 meV. It is unlikely that the Stoner excitations contribute such pronounced peaks that locate at the energy lower than 200 meV and show the energy distribution as narrow as 100 meV. Moreover, it will be shown in the later section (Sec. 5.3.4) that the profile of the excitation peak agrees with the theoretical prediction for the spin waves in this system. Base on these considerations, we attribute the magnetic excitations observed in the thick Fe films to the spin wave excitations.

The spin wave peaks in the 5 ML Fe film also show different features in comparison to those in the 2 ML Fe film. The energy of the excitation peak position is found to be relatively lower than that in the 2 ML Fe film for the same $\Delta K_{||}$. This difference is about 20 meV depending on $\Delta K_{||}$. Secondly, the excitation peaks are strongly broadened and asymmetric as shown in Fig. 4.10. The typical "tail" can be observed in the normalized difference spectra of $\Delta K_{||} = 0.7$ Å^{-1} in Fig. 4.10. By comparing the experimental data to the theoretical calculations [27], the broadening of the peak may be attributed to the high energy modes of the spin waves (Sec. 5.3.4). They correspond to standing wave modes in the Heisenberg model, which are shown in the gray area in Fig. 2.5.

The normalized SPEELS spectra for 24 ML Fe film are shown in Fig. 4.11. The

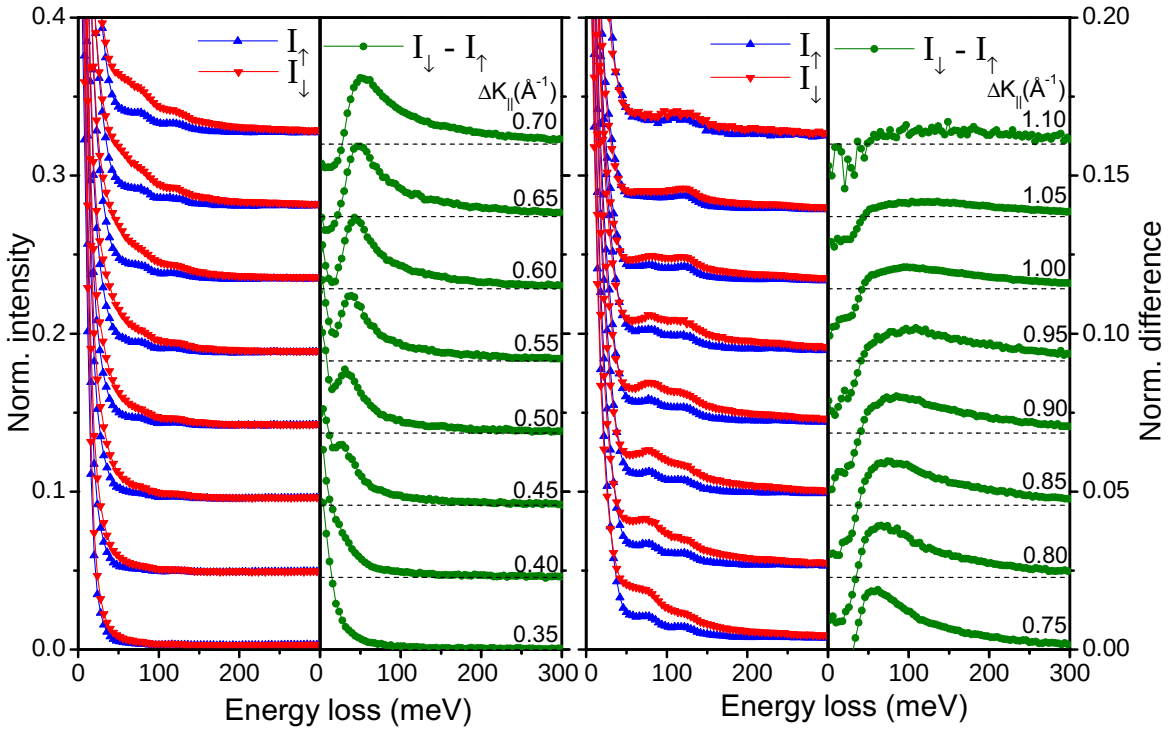

Figure 4.10: The normalized spectra $I_\uparrow$ (blue up-triangle), $I_\downarrow$ (red down-triangle) and their difference (green dot) for 5 ML Fe film. The incident electron energy is 4 eV with the energy resolution FWHM≈18 meV. The in-plane wave vector transfer $\Delta K_{||}$ varies from 0.35 $Å^{-1}$ to 1.1 $Å^{-1}$.

shapes of spin wave peaks are quite similar to those in 5 ML Fe film. However, it can be noticed that the ratio of the tail part with respect to the elastic peak is relatively higher for the 24 ML film than the 5 ML film. This can be seen in the normalized spectra for $\Delta K_{||} = 0.35$ $Å^{-1}$. In comparison to the small gap between the $I_\uparrow$ and $I_\downarrow$ spectra for 5 ML Fe/W(110), the gap is considerably large for the 24 ML Fe film.

The dependence of the peak maxima on the $\Delta K_{||}$ are plotted in Fig. 4.12 for both 5 ML and 24 ML Fe. The maxima of the spin wave peaks range from 20 meV to 130 meV in 0.35 $Å^{-1} \leq \Delta K_{||} \leq 1.1$ $Å^{-1}$. For the smaller wave vectors, i.e. $\Delta K_{||} < 0.45$ $Å^{-1}$, the excitation peaks are strongly influenced by the elastic peaks, whose energies are marked with larger errors. The energies of the excitations for the 5 ML Fe film are averagely 10 meV smaller than those for the 24 ML Fe film.

In order to show the thickness dependence of the spin wave excitations, the SPEELS spectra measured for the Fe films of the thicknesses from 2 ML to 24 ML are presented in Fig. 4.13. The in-plane wave vector transfers are 0.5 $Å^{-1}$ and 0.7 $Å^{-1}$, respectively. In Fig. 4.13, the dashed lines indicate the peak positions for 2 ML Fe film. Taking this line as a reference, one observed that the spin wave energies in thicker Fe films are all lower than that in the 2 ML Fe film. The most significant energy drop is in the 5 ML thick film. For thicker films, the peaks shift slightly back to higher energy. This has been shown in Fig. 4.12, where the spin wave energy in the 24 ML Fe film is about 10 meV higher than that in the 5 ML film. However, it is known that the morphology

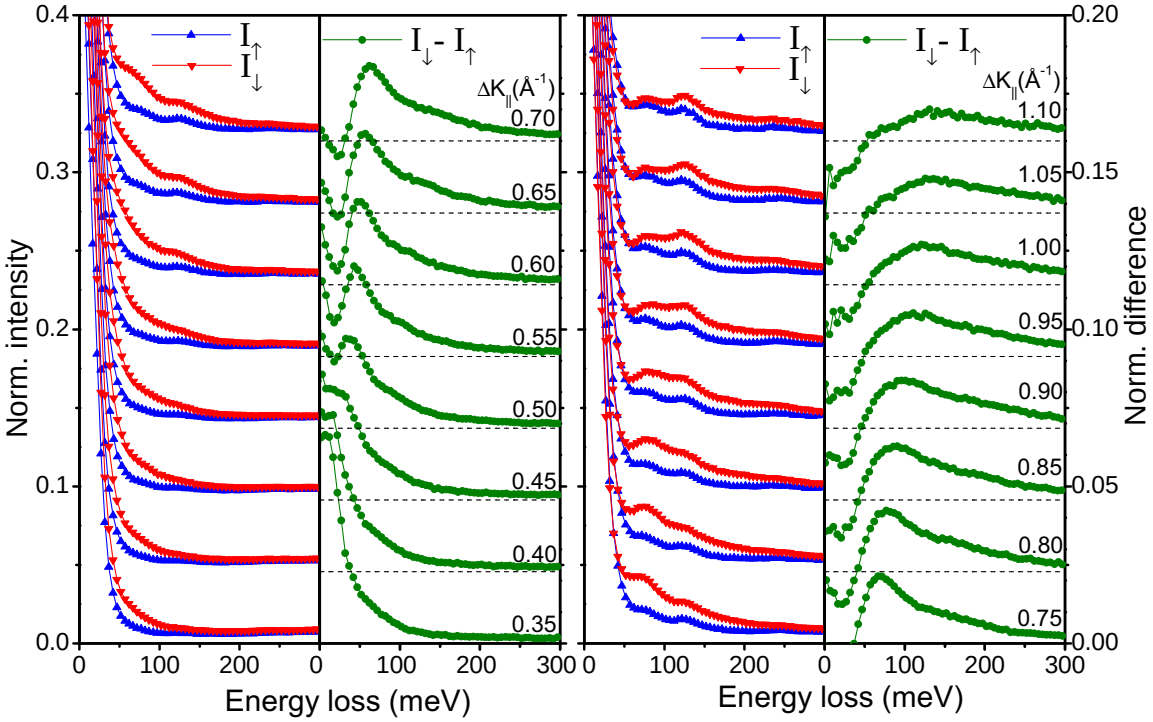

Figure 4.11: The normalized spectra $I_{\uparrow}$ (blue up-triangle), $I_{\downarrow}$ (red down-triangle) and their difference (green dot) for 24 ML Fe film. The incident electron energy is 4 eV with the energy resolution FWHM≈20 meV. The in-plane wave vector transfer $\Delta K_{||}$ varies from 0.35 $Å^{-1}$ to 1.1 $Å^{-1}$.

of 3 ML film is not homogeneous. The film consists of double, triple and even thicker layer regions according to the previous studies [9, 10]. The intermediate energy of the excitations in the 3 ML film is ascribed to the overlap of the spin wave excitations in the double layer and thicker layer regions. On the other hand, the spin wave peaks become more and more asymmetric as the thickness varies from 2 to 24 ML. For the spectra of 0.5 $Å^{-1}$, one may notice that the difference spectra become higher and higher in the energy range from 100 to 200 meV. For other low wave vectors, this feature can be also observed as has been demonstrated in the difference spectra of 5 ML and 24 ML Fe films in Fig. 4.10 and Fig. 4.11.

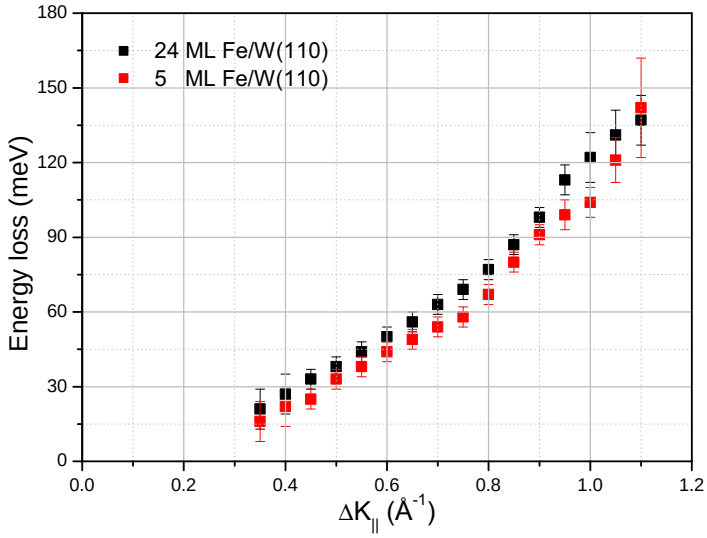

Figure 4.12: The dispersion relations for the spin wave excitations in 5 and 24 ML Fe/W(110). The data points are obtained by taking the energy positions of peak maxima in the difference spectra shown in Fig. 4.10 and Fig. 4.11.

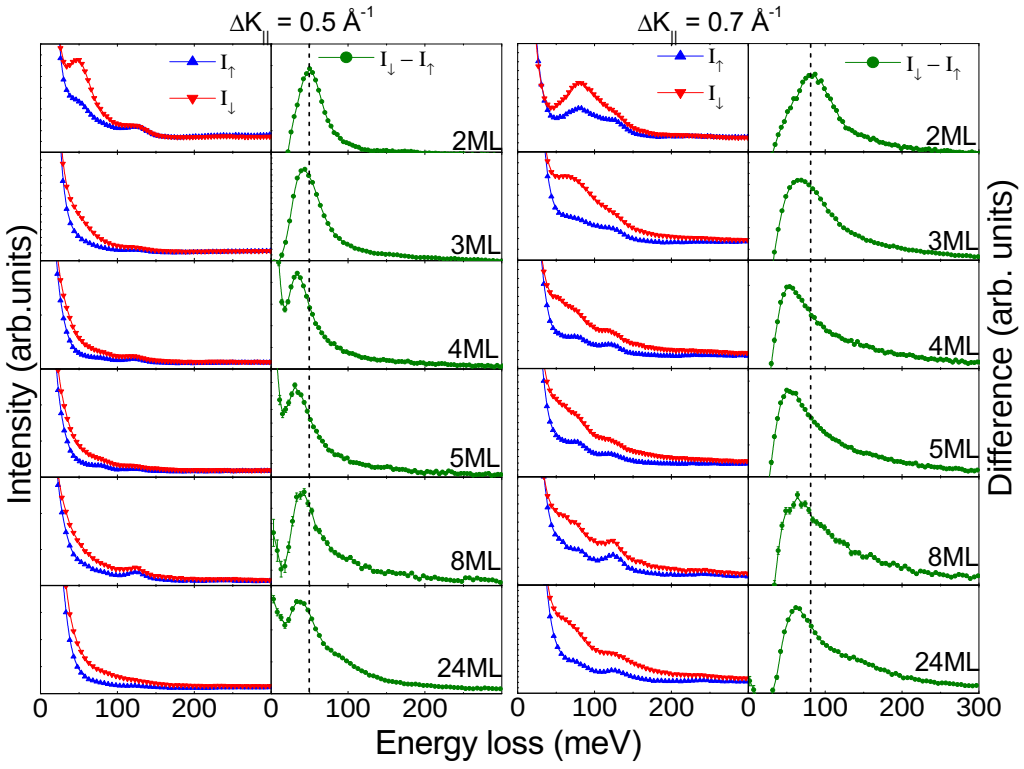

Figure 4.13: The SPEEL-spectra $I_\uparrow$ (blue up-triangle), $I_\downarrow$ (red down-triangle) and their difference (green dot) for 2 ML, 3 ML, 4 ML, 5 ML, 8 ML, and 24 ML Fe/W(110) with the wave vector transfers of 0.5 $Å^{-1}$ and 0.7 $Å^{-1}$. The dashed lines indicate the spin wave energies in 2 ML Fe/W(110). All the data are obtained using the incident energy of 4 eV with the energy resolution of about 20 meV.

Chapter 5

Discussion

In the first section of this chapter, the Heisenberg model is employed to analyze the spin waves in the Fe thin films. The exchange constants and the spin wave stiffness coefficients are obtained by fitting the experimental spin wave dispersions using the next nearest neighbor Heisenberg model. The properties of the spin waves are compared for the Fe films of different thicknesses. In the second section, the lifetime and spatial distribution of the spin waves are estimated according to the analysis of the spin wave spectra, which provides an intuitive picture of the spin waves in 2 ML Fe/W(110). Finally, the thickness dependence of the spin wave stiffness coefficients and the SPEELS spectra for 1 ML, 2 ML and 5 ML Fe/W(110) are compared with the calculations based on the itinerant electron theory [26, 27, 29].

5.1 Spin wave dispersions discussed in the Heisenberg model

In the following discussions we assume that the spin wave peaks observed in the spectra mainly consist of the surface spin wave mode. The energies determined from the peak maxima can be taken as the dispersion relation for this mode. This is supported by the calculated spectral density functions for the 5 ML Fe/W(110) film in Fig. 2.7 (a), which demonstrates that the spectra are dominated by the lowest mode. However, this assumption may be not valid for high wave vectors as shown in the spectral density function in Fig. 2.7 (b). Different modes may strongly overlap together and show a broad profile. In this case, the peak position can not be taken as the energy of the surface mode.

5.1.1 Spin waves in 2 ML Fe/W(110)

In this section the spin wave dispersion in the 2 ML Fe film is fitted by the next nearest neighbor Heisenberg (NNNH) model. The exchange parameters obtained from the fit will be discussed in relation to the domain wall width in the sample.

To reduce the number of fitting parameters in the Heisenberg model, the 2 ML Fe film are considered as the free standing film with the perfect bcc (110) structure. The lattice constant is equal to that of the W(110) surface due to the pseudomorphic growth

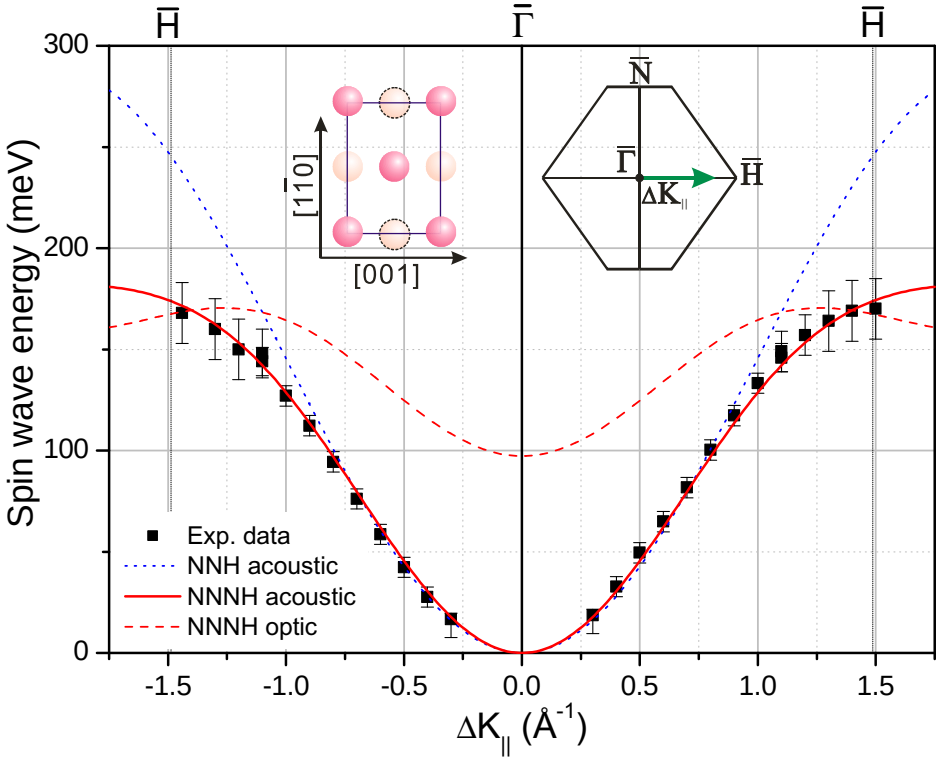

Figure 5.1: The spin wave dispersion in 2 ML Fe/W(110) (black squares) fitted by the acoustic mode of the NNNH model (red curve) with J_NS=7.6 meV and $J_{NN}S$=4.6 meV. The red dashed curve represents the optical mode of the same model. The acoustic mode of the NNH model (blue dot curve) shows a large discrepancy in the high wave vector regime. The surface lattice structure in real and reciprocal space is also schematically shown as references. The red and yellow balls represent the atoms in the first and second layer, respectively.

of the film. Assuming that the single peak in the SPEEL-spectra for 2 ML Fe/W(110) is mainly composed of the acoustic spin waves, its dispersion behavior is fitted by the dispersion curve of the acoustic mode. The effective magnetic anisotropy energy (MAE) in 2 ML Fe/W(110) is estimated to be about 1×10^6 J/m^3, which corresponds to 0.1 meV/atom [86, 88]. This is much smaller than the typical spin wave energy observed in the SPEELS experiments, which is from 20 meV to 150 meV. Therefore, the MAE will be neglected in the fitting of the spin wave dispersion.

Firstly, the nearest neighbor Heisenberg model (NNH) is applied. The acoustic mode is expressed as $\hbar\omega = 12J_NS[1-\cos(\frac{1}{2}\vec{Q}_{||}a_0)]$ (Eq. 2.12). This expression can not describe the experimental dispersion in the whole wave vector regime. The fitting curve is shown in Fig. 5.1 for $J_NS = 12$ meV. It fits the experimental results well for low wave vectors ($\Delta K_{||}$ <0.6 Å^{-1}), while there is a large discrepancy in the high wave vector regime($\Delta K_{||} > 1.0$ Å^{-1}).

A better fit throughout the entire Brillouin zone is obtained by including the exchange interaction between the next nearest neighbors. This consideration is based on the calculated exchange constants by Pajda *et al.* [35] as shown in Tab. 2.1. The exchange constant between the next nearest neighbors in bcc Fe is as large as 60%

of that between the nearest neighbors i.e., J_{NN}/J_N=0.6. This is not negligible in the description of spin waves. The spin wave dispersion of the acoustic mode considering the additional next nearest neighbors can be written in the following form (Eq. 2.16):

$$\hbar\omega = 12J_NS[1 - \cos(\frac{1}{2}\vec{Q}_{||}a_0)] + 4J_{NN}S[1 - \cos(\vec{Q}_{||}a_0)].$$

The contributions of the next nearest neighbors produce the additional term with the coefficient $J_{NN}S$. According to the calculation results in Tab. 2.1, the ratio J_{NN}/J_N = 0.6 is applied in the fitting process. The result of the fit is shown in Fig. 5.1 denoted by the red solid curve. It fits the data points very well in the whole Brillouin zone. From the fit, the exchange parameters, J_NS = 7.6±0.5 meV and $J_{NN}S$ = 4.6±0.3 meV, are obtained for the nearest and next nearest neighbors, respectively.

The exchange parameters are obtained based on the assumption of the free standing film with the perfect bcc(110) structure. In reality, the situations of the interface layer and the surface layer in the 2 ML Fe film are not identical due to the presence of the tungsten substrate [27, 97]. In comparison to the Fe atoms in the surface layer, the magnetic moment of the Fe atoms in the interface layer is reported to be 19% smaller [98]. However, this is not considered in the simple model. Furthermore, due to the hybridization between the interface layer and the substrate, the exchange parameters in the two atomic layers are expected to be rather different.

Due to the large mismatch between the lattice constants of Fe and W, the interlayer distance between the two Fe atomic layers is about 1.7 Å, much smaller than that of the tungsten lattice of 2.24 Å [18]. Therefore, the real distances between the lattice sites are different from those of the perfect bcc lattice. Because the exchange interaction is sensitive to the distance between two neighbors [35], the real exchange constants of the Fe atoms can be quite different from that obtained in the simple NNNH model. According to the STM studies on 2 ML Fe/W(110), it was observed that the domain wall orientation is anisotropic, and prefers the $[1\bar{1}0]$ direction[12, 99]. Based on this observation and the Monte Carlo simulations, it has been proposed that the effective interlayer exchange, i.e., between the center atom and the neighbors in the $[0\bar{1}0]$ and $[\bar{1}00]$ directions (the atoms marked with dashed boundary in Fig. 5.1) could be even twice as large as in-plane exchange, i.e., between the center atom and the four in-plane nearest neighbors (red balls without boundary) [100]. However, this ratio is supposed to be 0.6 in the fitting. Therefore, the exchange parameters obtained from the fit only allow for an estimation of the exchange parameters in the 2 ML Fe film. Direct comparison of these exchange parameters with the theoretical results in Tab. 2.1 has to be taken cautiously.

From the obtained exchange parameters, the spin wave stiffness D can be calculated by $D = (1.5J_N + 2J_{NN})Sa_0^2$ according to Eq. 2.18, which gives D = 206±13 meVÅ^2 for the spin waves in 2 ML Fe/W(110). Unlike the exchange parameters obtained from the fit, the spin wave stiffness is determined by the experimental dispersion curve in the low wave vector region. Its value is less influenced by the fitting models.

It is known that the exchange stiffness A can be derived from D according to the relation $A = \frac{DS}{2\Omega}$, in which Ω is the atomic volume, and S is the spin quantum number of individual atom [43]. If we take S = 1.3 and Ω = 12 Å^3 for the Fe atoms in 2 ML

Fe/W(110)[1], A = 1.8±0.1×10^{-11} J/m is obtained. This is in good agreement with the values derived from the analysis of the domain wall width in Ref. [12, 13], where A = 1.25×10^{-11} J/m and 1.82×10^{-11} J/m have been reported. It should be pointed out that the SPEELS measurements are performed at room temperature, while the domain wall analysis is based on the STM studies performed at low temperature of about 15 K. The temperature effect is not considered in our analysis. Also, the magnetization of the double layer islands is oriented out-of-plane at low temperature, while it is in-plane at room temperature. However, assuming that the exchange interaction is isotropic, the exchange stiffness, which is mainly determined by the exchange interaction, will be independent of the magnetization directions.

The Heisenberg model provides a simple picture of spin waves in 2 ML Fe/W(110). The obtained exchange parameters can be only taken as a rough estimation of the exchange parameters in the 2 ML Fe film.

5.1.2 Spin wave dispersion in 1 ML Fe/W(110)

In comparison to the spin wave excitations in 2 ML Fe/W(110), the excitations in 1 ML Fe/W(110) show rather low energies varying from 20 meV to 60 meV. In the difference spectra in Fig. 4.8, the excitation peaks for $\Delta K_{||}$ <0.5 Å^{-1} show low background in the high energy loss region as compared to the excitation peaks at low energy losses. This is similar to the spin wave excitations observed in 2 ML Fe/W(110). The width of these excitation peaks are below 100 meV. These magnetic excitations are unlikely to be the Stoner excitations, as the energy distribution of the Stoner excitations is typically in the energy range of a few eV [1, 38–40]. Moreover, a systematic shift of the peak has been observed as the $\Delta K_{||}$ changes, which implies the dispersion characteristic of these magnetic excitations. According to these considerations, the magnetic excitations in 1 ML Fe/W(110) are treated as spin waves and discussed using the Heisenberg model.

To estimate the exchange energy between the two nearest neighbors in 1 ML Fe on W(110), the NNH model is employed. For this system the spin wave dispersion is expressed as $\hbar\omega = 8J_NS[1 - \cos(\frac{1}{2}\vec{Q}_{||}a_0)]$. By fitting the experimental dispersion, the exchange parameter J_NS is obtained as 6±1 meV. A large effective magnetic anisotropy energy of about 40×10^6 J/m^3 (about 4 meV/atom) has been reported for this system [101, 102]. The inclusion of the MAE in the fitting only produces a small change of about 0.4 meV for the exchange parameter J_NS, which is within the uncertainty of the result. Hence, the effect of the MAE is not included in the discussion of exchange parameters. Assuming that the spin S is approximately 1.3 for 1 ML Fe on W(110) [98], J_NS^2 = 7.8±1.3 meV is then estimated. This value is in good agreement with the results obtained from the the analysis of domain wall width [102][2], where J_NS^2 = 7 meV is reported.

[1] S is the average value of the spins in the surface and interface Fe layers according to Ref. [98]. The atomic volume is taken from the value of bulk bcc Fe.

[2] The exchange constant J defined in Ref. [102] corresponds to $2J_NS^2$ used in this work.

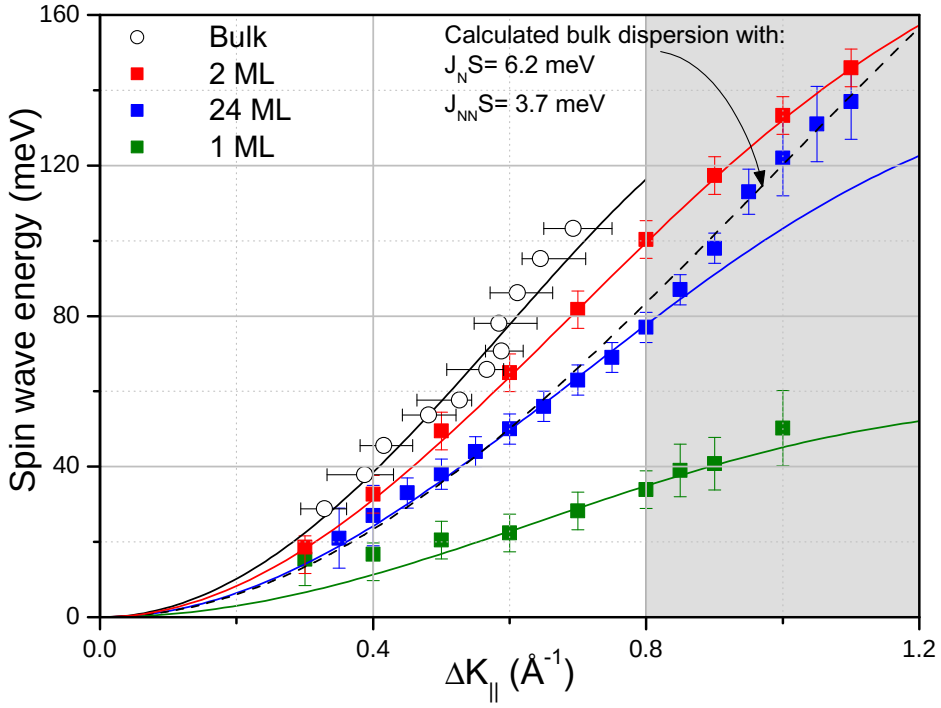

Figure 5.2: Comparison of the spin wave dispersions in the 1 and 2 ML Fe/W(110), and at the surface of 24 ML Fe/W(110). The corresponding dispersion curves (color solid lines) are the fit in NNNH model. The dispersion data in bcc bulk Fe is taken from Ref. [54]. Its dispersion curve is shown as black solid line according to the relation $E = Dq^2(1 - \beta q^2)$ with D=260 meVÅ^2 and β=0.47 Å^2 [54]. The dashed curve is a bulk dispersion calculated with the exchange parameters obtained from 24 ML Fe, which are $J_N S$=6.2 meV and $J_{NN} S$=3.7 meV.

5.1.3 Comparison of the spin wave dispersions in thin films and bulk

The spin wave dispersions for 1 ML, 2 ML and 24 ML Fe/W(110) are shown in Fig. 5.2, as well as the dispersion for bulk Fe. For 24 ML Fe/W(110) our discussion is focused on the low wave vector regime of $\Delta K_{||} \leq 0.8$ Å^{-1}, where the spin wave spectra are assumed to be dominated by the surface modes. It should be noted that the surface lattice constant in 24 ML Fe/W(110) is equal to the bulk value, and smaller than those in the pseudomorphic 1 ML and 2 ML Fe films. This gives different surface Brillouin zone boundaries, i.e., 1.49 Å^{-1} for 1 ML and 2 ML Fe/W(110), 1.64 Å^{-1} for 24 ML Fe/W(110). Also, the 3D Brillouin zone boundary in the bulk Fe is 2.19 Å^{-1} along the ΓH direction, which is much larger than those in the thin films.

As has been shown in Sec. 2.1, the spin wave dispersion can be calculated from the eigenvalues of the factor matrix in Eq. 2.19. For the 24 ML Fe film, the experimental dispersion in $\Delta K_{||}$ <0.8 Å^{-1} can be well described by the surface mode in the NNNH model with $J_N S$=6.2 meV and $J_{NN} S$=3.7 meV, as the blue solid curve shown in Fig. 5.2. The ratio J_{NN}/J_N=0.6 is also kept constant in this case. As the uncertainty of the experimental data at low wave vectors are quite large, the spin wave stiffness is obtained

from the quadratic behavior of the fitting curve, which gives D=163±10 meVÅ^2. This is smaller than D=206±13 meVÅ^2 in 2 ML Fe, and D=260 meVÅ^2 in bulk [54].

The NNNH model was also applied to fit the spin wave dispersion for 1 ML Fe. The fitting curve is shown as the green curve in Fig. 5.2. From the fitting results, the NNNH model gives $J_N S$=3.2±0.6 meV and $J_{NN} S$ = 1.9±0.4 meV, and the spin wave stiffness D is 70±15 meV according to $D = (J_N+2J_{NN})Sa^2$. Tab. 5.1 shows the fitting results in the NNNH model for 1 ML, 2 ML, and 24 ML Fe/W(110). The parameters are only for the comparison of exchange parameters in the Fe films, which can not be taken as the description of the realistic exchange interactions in the film. In Tab. 5.1, the exchange parameters for the 1 ML Fe film are two times smaller than those obtained for thicker Fe films. It may be attributed to the strong hybridization between the Fe film and the tungsten substrate. It has been shown that the magnetic moment of the Fe atoms of the monolayer supported by the substrate can be reduced by about 29% percent as compared to the free standing Fe monolayer [98]. It suggests a large reduction of the exchange interaction in 1 ML Fe/W(110). Moreover, the spin waves in 1 ML Fe/W(110) could be even strongly damped by the conduction band in W substrate as compared to those in thicker Fe films [29].

Fig. 5.2 shows that the spin wave dispersion curves in thin Fe films are lower than that in bulk. This can be attributed to the reduction of the neighboring atoms in the thin films, and the difference of the lattice constants as well. For comparison, we produce the spin wave dispersion for a bulk bcc crystal using the NNNH model based on the exchange parameters for 24 ML Fe/W(110), $J_N S$=6.2 meV and $J_{NN} S$=3.7 meV. The dispersion curve is plotted as the black dashed line in Fig. 5.2. One can see that the produced dispersion curve is evidently lower than the experimental bulk data in open circles. The produced dispersion curve is also clearly lower than bulk dispersion curve, even though the exchange parameters for 2 ML Fe/W(110), $J_N S$=7.6 meV and $J_{NN} S$=4.6 meV, were applied. This is in contrast to our observations on the spin waves in fcc and hcp Co thin films, where the exchange parameters obtained for the thin films can well describe the dispersion in bulk Co [2, 70].

For the soft spin waves dispersion in Fe thin films, the temperature effect can be excluded, since the measuring temperature is about 300 K, and quite lower than the T_C of 24 ML Fe film, which is estimated to be close to the bulk value. As the low energy electrons are very surface sensitive, the measured spin waves are localized at the surface. For 24 ML Fe film, the influence of the W substrate is assumed to be negligible. Also, the 24 ML Fe film shows a good bcc(110) surface without the dislocation network according to sharp (1×1)bcc(110) LEED spots shown in Fig. 3.12. By excluding the influence from the measuring temperature, substrate and dislocation networks, the observation in Fig. 5.2 thus indicates that the exchange parameter JS at the surface are lower than that in bulk according to the Heisenberg model [25].

It should be pointed out that the simply Heisenberg model can not take into account of the decay of the spin waves, which is obviously not negligible for the high wave vector spin waves. The effect of the decay can be observed from the significant broadening of the spin wave peaks for all the Fe films. It is then necessary to discuss the influence of the strong decay on spin wave dispersion. In the spin wave theory based on the itinerant electron model, the decay of spin waves into the Stoner excitations are expected to be more pronounced in the thin films than in bulk. Due to breakdown of

Table 5.1: The fitting parameters for the 1 ML, 2 ML and 24 ML Fe films obtained using the NNNH model. The spin wave stiffness D for the bulk Fe is taken from the neutron scattering experiments [54].

	$J_N S$(meV)	$J_{NN} S$(meV)	D(meVÅ^2)
1 ML Fe/W(110)	3.2±0.6	1.9±0.4	70±15
2 ML Fe/W(110) (acoustic mode)	7.6±0.5	4.6±0.3	206±13
24 ML Fe/W(110) (surface mode)	6.2±0.5	3.7±0.3	163±10
Bulk Fe	–	–	260

translational invariance normal to the surface, the wave vector normal to the surface are not conserved. In the thin film this breakdown of wave vector conservation opens more decay channels that is not accessible to bulk spin waves [27]. As the decay of the spin waves may also shift the spin wave energy [37], the large energy difference between the dispersion for bulk and surface may be due to the stronger decay of the spin waves at the surface.

In summary, the spin wave stiffness and the exchange parameters estimated from the spin wave dispersions for 1 ML and 2 ML Fe/W(110) are in agreement with the results obtained from the domain wall analysis. The spin wave energy in 1 ML Fe/W(110) is much lower than those observed in the thicker films, which may be due to the strong influence of the W substrate. The spin waves measured on the Fe films are also compared with the INS experiments for bulk Fe. Within the Heisenberg model, the results indicate a reduction of the exchange parameters at the Fe (110) surface. However, to describe the spin wave dispersions explicitly, the calculations based on the itinerant electron model are still needed.

5.2 Properties of spin waves in Fe thin films

In the difference spectrum, the excitation peaks give the energy distribution of the spin waves. Through the Fourier transform, the time distribution of the spin waves can be obtained from the excitation peak. It is known that the measured spin wave peaks always include the instrumental response function, which will broaden the spin wave peaks. It is assumed that the spin wave peaks resemble Lorentzian distributions in the spectra [52], and the instrumental response function is a Gaussian distribution. The spin wave peak can be estimated by fitting the experimental spin wave peaks with the convolution of a Gaussian and a Lorentzian, which is the Voigt distribution. In the fitting, the FWHM of instrumental response function, represented by the Gaussian, is kept constant as 20 meV according to the measurement resolution. The FWHM of the Lorentzian part gives the energy width of the spin wave peak, $FWHM_E$, which is shown as a function of $\Delta K_{||}$ in Fig. 5.3 (a)[3].

[3]The spin wave peaks measured for the double layer regions can be broadened due to the spin wave excitations in the triple layer islands. This effect can be seen in Fig. 4.7 (d). The width difference between the spin wave peaks in 2 ML and 1.6 ML Fe films is only about 6 meV. This does not change the analysis qualitatively.

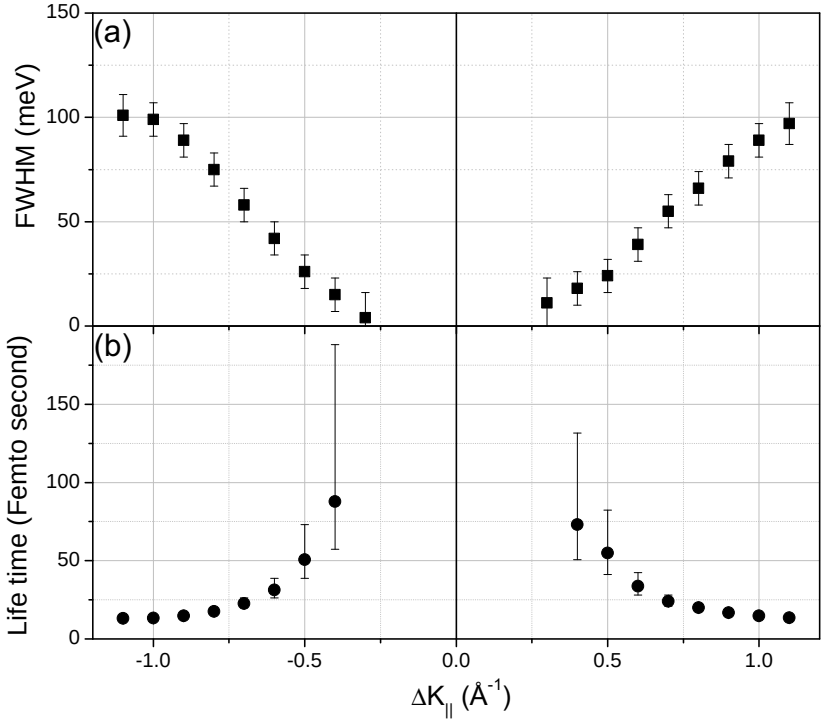

Figure 5.3: (a) The FWHM of the spin wave excitations in 2 ML Fe/W(110). The data have been deconvoluted using Voigt distribution (see text). (b) shows the lifetimes of spin waves in 2 ML Fe/W(110), which are estimated from the FWHM in (a) using Eq. 5.1. The lifetime for 0.3 $Å^{-1}$ is not shown due to the large uncertainty of the FWHM.

For a Lorentzian distribution, its Fourier transform shows an exponential decay. The lifetime of the spin waves is defined as the time that the amplitude of the spin wave drops to its e^{-1}. It can be calculated by

$$\text{Lifetime} = \frac{2\hbar}{\text{FWHM}_\text{E}}, \tag{5.1}$$

where $\hbar$ is Planck constant. Using Eq. 5.1 the lifetime of the spin wave in 2 ML Fe/W(110) is calculated up to the wave vector of 1.1 $Å^{-1}$ and shown in Fig. 5.3 (b). The lifetime of spin waves is typically shorter than 50 femto-seconds (fs) for wave vector larger than 0.5 $Å^{-1}$. Due to the experimental errors for the FWHM at low wave vector, the lifetime is estimated with large uncertainty. However, it is evident that the lifetime of the spin waves becomes longer for small wave vector spin waves because of the drop down of FWHM at the low wave vector.

For the superparamagnetic samples, such as the Fe films of 1.2 ML, 1.4 ML and 1.6 ML, the average fluctuation frequency of the magnetic islands can be estimated from the relation $\tau = \tau_0 e^{\mathrm{N}\mu_\mathrm{B}\mathrm{H_A}/2\mathrm{k_B}\mathrm{T}}$, where N is the number of the spins in the ferromagnetic block, and H_A is the effective anisotropy field [34]. $1/\tau_0$ is estimated to be about $\sim 10^{10}$ Hz [34]. $\mathrm{N}\mu_\mathrm{B}\mathrm{H_A}/2$ represents the magnetic anisotropy energy for the double layer islands. It is assumed that the double layer islands in the 1.2 ML Fe film is averagely 30 nm^2 in area and with the film thickness of 4 Å [10, 12]. With the effective

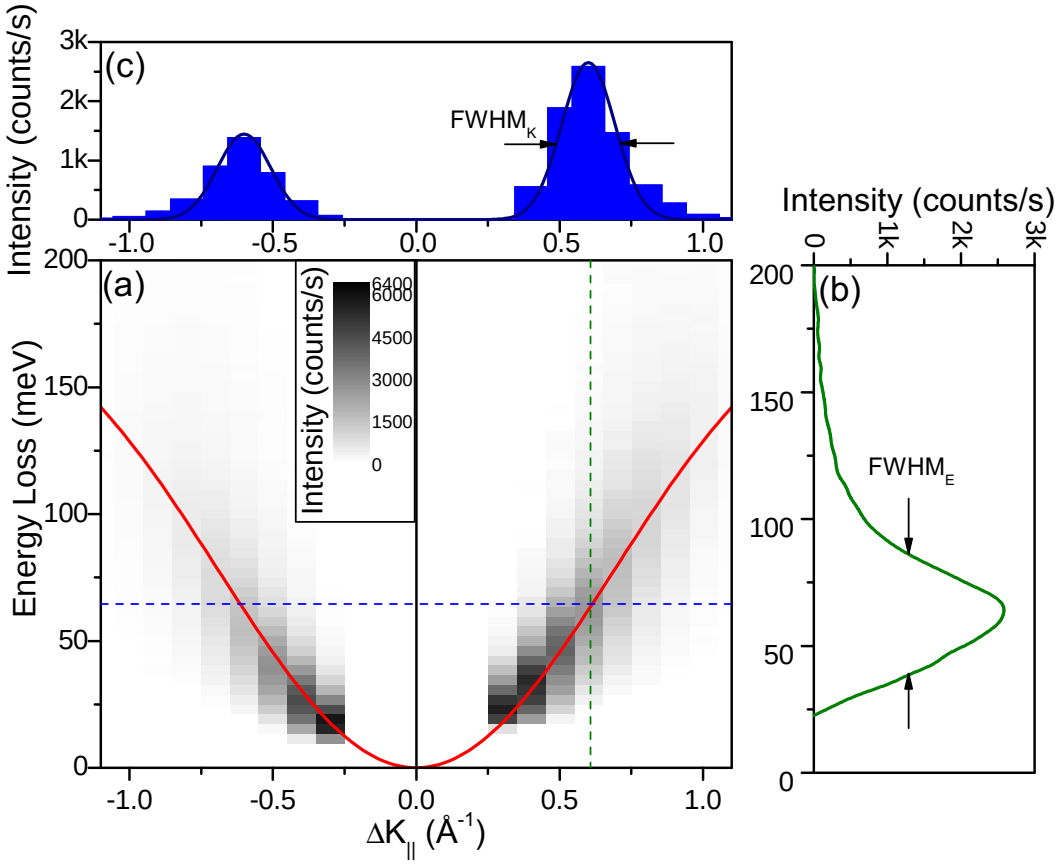

Figure 5.4: (a) The contour map of the spin wave distribution in the energy-momentum space, which is obtained from the spin wave peaks in the difference spectra in Fig. 4.2. The intensity is represented by gray scale. The red line denotes the acoustic mode in the NNNH model as has been derived in Sec. 5.1.1. Two intensity profiles at $\Delta K_{||} = 0.6$ Å^{-1}(marked by the green dashed line) and E = 65 meV (the blue dashed line) are shown in (b) and (c), respectively. The histogram shown in (b) reveals two peaks that are fitted with two Gaussian distributions (dark blue curves).

magnetic anisotropy energy 1×10^6 J/m^3[86, 88], we obtained $N\mu_B H_A/2 \approx 0.08$ eV for the double layer islands. At room temperature, the mean fluctuation time of these islands is approximately 1×10^{-9} s. It is several orders of magnitude larger than the typical spin wave lifetime. Hence, the thermal fluctuations of the magnetization in the superparamagnetic blocks are almost static for the excitation of spin waves. The spin waves excited in the superparamagnetic Fe films experience little influence by the thermal fluctuation of the magnetization.

In order to obtain the spatial distribution of the spin waves in 2 ML Fe/W(110), the spin wave intensity distribution is plotted as a contour map in the energy-momentum space in Fig. 5.4 (a). The spin wave intensity is represented by the gray scale. The distribution of spin wave intensity in the momentum space is obtained from the profile at E = 65 meV, as shown in (c). We assume that the momentum distribution is the Gaussian distribution[4], the full width at half maximum of the spin waves distribution

[4]This FWHM is also influenced by the convolution of the instrumental response function. Never-

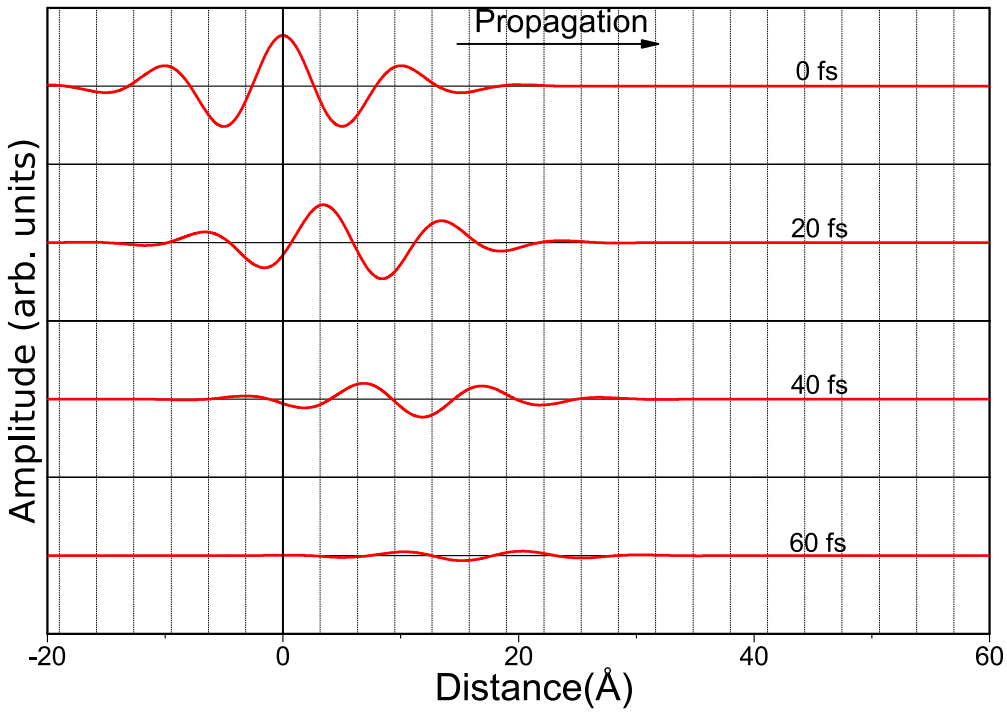

Figure 5.5: Schematic of the spin wave evolution with $\Delta K_{||}$ about 0.6 Å^{-1} in 2 ML Fe/W(110). The red cosine curves represent the amplitude of the spin wave in time and space. At t = 0, spin wave starts to propagate towards the right from x = 0. The dashed lines represent the lattice period of 3.165 Å in 2 ML Fe/W(110) along the [001] direction.

in the momentum space is obtained as $FWHM_k \approx 0.22$ Å^{-1}.

Using the Fourier transform for the Gaussian, $FWHM_{space} = 8\ln 2/FWHM_k$, the $FWHM_{space}$ of the spin wave intensity distributed in space is estimated to be 30 Å along the [001] direction. This length is much smaller than the typical size (along the [001] direction) of the double layer islands in 1.2 ML to 2 ML Fe/W(110), which is typically larger than 10 nm [8]. Thus the influence of the double layer islands in space can be neglected.

For the spin wave of $\Delta K_{||} = 0.6$ Å^{-1}, the wave length of spin wave is about 10 Å. The wave packet contains only a few oscillations in space. This is schematically illustrated in Fig.5.5 by the product of a cosine function and a Gaussian distribution corresponding to the space distribution of the spin wave. The spin wave starts to propagate at t = 0 with the maximum amplitude at x=0. After 40 fs later, the amplitude is reduced by e^{-1}. The group velocity ($v_g = dE/dq$) is derived from the slop of the dispersion curve at $\Delta K_{||} = 0.6$ Å^{-1}, which is about 0.27 Å/fs or 27 km/s. Thus, during its lifetime the spin wave packet only propagates forwards for about 1 nanometer. The phase velocity is obtained by $v_p = E/q$, which gives 16 km/s for spin waves with $\Delta K_{||} = 0.6$ Å^{-1}. It is smaller than the group velocity v_g, which indicates that the spin wave disperses slightly during the propagation (not shown in the schematic).

theless, this does not change the results qualitatively.

5.3 Comparison between the SPEELS results and calculations

In the calculation of spin waves based on the itinerant electron model, the spectral density function of spin waves can be calculated according to the electronic band structure [27]. In this method, the spin waves naturally decay into the Stoner excitations, which enables to obtain a line width for spin wave excitations in Fe thin films [27]. As has been shown in Fig. 2.7, the calculations reveal broad peaks in the spectral density functions, which, in principle, agree with the spin wave profiles observed in SPEEL-spectra. In this section, it will be shown that the experimentally determined spin wave stiffness shows similar thickness dependence as predicted by the calculation [28]. Moreover, the spin wave spectra of 1 ML, 2 ML and 5 ML Fe/W(110) are compared with the spin wave spectral density function calculated by the same model [27].

5.3.1 Thickness dependence of spin wave stiffness

As it has been discussed in Sec. 2.1, the spin wave stiffness D can be obtained from the relation $E(\vec{Q}) = D\vec{Q}_{||}^2$ at small $\vec{Q}_{||}$. Fig. 5.6 (a) shows the energies of the spin waves with $\Delta K_{||} = 0.5$ Å^{-1} and 0.7 Å^{-1} as a function of the film thickness. The spin wave stiffness D is calculated from the energy of the spin waves with $\Delta K_{||} = 0.5$ Å^{-1}. The results are shown as red dots in Fig. 5.6 (b). The effective spin wave stiffness of the Fe films has been calculated by Costa, Muniz and Mills [27, 28]. These results are also shown in Fig. 5.6 (b) (black dots) for comparison.

In Fig. 5.6 (a), the spin wave energies for $\Delta K_{||} = 0.5$ Å^{-1} and 0.7 Å^{-1} show similar thickness dependence. In principle, the relation $E(\vec{Q}) = D\vec{Q}_{||}^2$ holds for the spin waves of low wave vectors. Unfortunately, the energy of the low wave vector spin waves, e.g., $\Delta K_{||} = 0.35$ Å^{-1}, is so low that the excitation peak in the difference spectra is strongly modified by the difference of the elastic peak, which can be seen in Fig. 4.10. This causes a large uncertainty in the determination of spin wave energy. Therefore, the spin wave energy for $\Delta K_{||} = 0.5$ Å^{-1} is selected for the estimation of D value. We have checked this approach using the results for 2 ML Fe/W(110). We obtain the D value of 196 meVÅ^2, which is very close to the result 206 meVÅ^2 obtained from the NNNH model.

In Fig. 5.6 (a) the spin wave energies show a non-monotonic thickness dependence. The spin wave in 1 ML Fe film show the lowest energy, which is followed by a sudden increase at 2 ML. A minimum can be observed around 4 ML. The energy then increases slightly for the thicker films. In Fig. 5.6 (b), our experimental D values show a quite similar thickness dependence as the theoretical results except for the exchange stiffness for 1 ML Fe/W(110). This will be discussed in Sec. 5.3.2 for the comparison of the experimental spectra and calculations [29] . For the thicker films, it should be noted that the surface is not flat due to the statistical growth of Fe on W(110) [9, 10]. Therefore, the spectrum for a given thickness contains the excitations from the layers of different thicknesses. Nevertheless, the tendency of the thickness dependence of the exchange stiffness is still clearly visible.

The variation of the D values in the low thickness from 2 to 6 layers was not explained

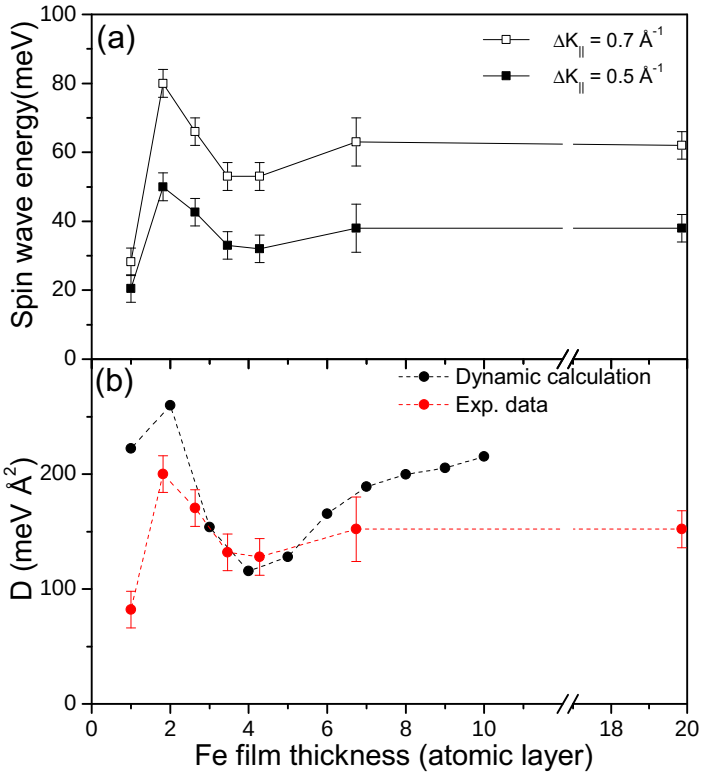

Figure 5.6: Spin wave energy and the spin wave stiffness as a function of Fe film thickness. The spin wave energies determined from Fig. 4.13 for the spin waves with $\Delta K_{||} = 0.5$ Å^{-1} (solid box) and 0.7 Å^{-1} (open box) are plotted in (a). The data for 1 ML Fe is obtained at 120 K, and those for the other thicknesses are measured at room temperature. (b) shows the spin wave stiffness calculated from the spin wave energy for $\Delta K_{||} = 0.5$ Å^{-1} (red dots). The theoretical results from Ref. [28] are shown as black dots for comparison.

in the theoretical study [28]. However, the authors stressed that the spin waves are very sensitive to the details of the electronic structure [28, 29, 37]. Due to the mismatch between the Fe film and the W substrate, as well as the hybridization of their electronic structures, the electronic structure of the Fe film may change significantly depending on the film thickness. This can be responsible for the thickness dependence of the spin waves stiffness. On the other hand, the dislocation networks are formed in the Fe films in this thickness range. The STM study demonstrated that the unit length of the network is in the range of 3∼5 nanometers [9]. This distance is just comparable to the spin wave spatial distribution as has been estimated in Sec. 5.2. Therefore, it is possible for the formation of the dislocation to cause a variation of the electronic structure in a short distance, which consequently influences the property of spin waves.

5.3.2 Spin waves in 1 ML Fe/W(110)

It has been shown in Sec. 5.1.2 that the experimentally obtained spin wave stiffness for 1 ML Fe/W(110) is lower than the theoretical value [28]. Fig. 5.7 (a) shows the

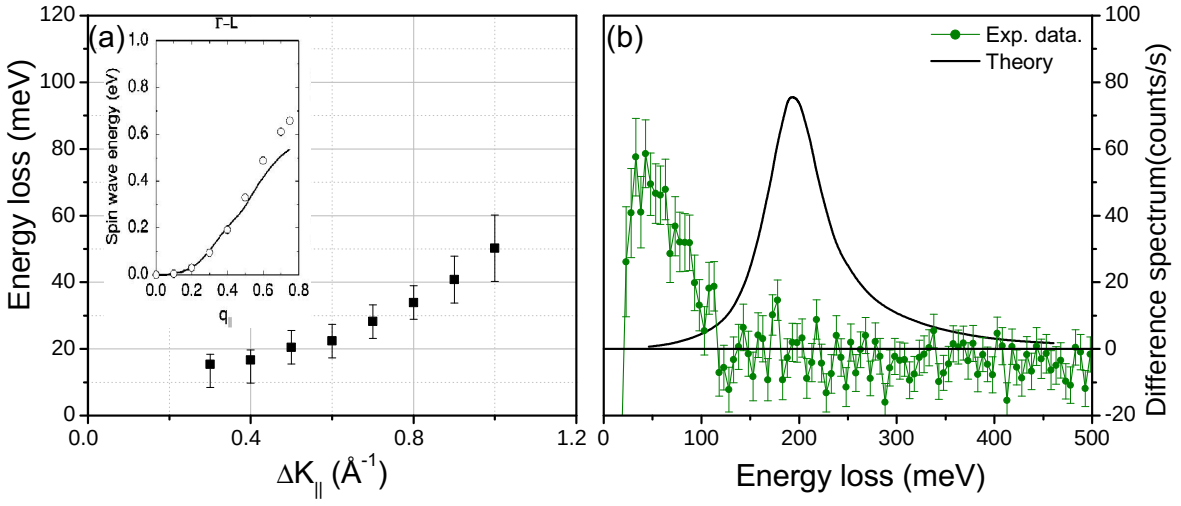

Figure 5.7: The comparison of the dispersion and the difference spectra between the experimental results and the theoretical calculation [29] for 1 ML Fe/W(110). (a) shows the spin wave dispersion obtained for 1 ML Fe/W(110) in the SPEELS experiments (filled squares). The calculated results based on the itinerant electron theory (open circles) are shown in the inset. (b) shows the experimental difference spectrum (green dots) with $\Delta K_{||} = 0.85$ Å^{-1} and the calculated spectral density function for $\vec{Q}_{||}$=0.79 Å^{-1} (black curve). It is obvious that the experimental spin wave energy is much smaller than that predicted in the theory.

comparison of the dispersion relations obtained from the SPEELS experiments and the calculation [29]. The calculated spin wave energies are much larger than the experimental results for all measured $\Delta K_{||}$. For example, the spectral density function shows the energy of about 200 meV at reduced wave vector of 0.4 (0.79 Å^{-1}), while the experimental data reveal that the magnetic excitation energy is only about 35 meV at $\Delta K_{||} = 0.8$ Å^{-1}. Direct comparison of the difference spectrum for $\Delta K_{||} = 0.85$ Å^{-1} and the calculated one for $\vec{Q}_{||} = 0.79$ Å^{-1} is shown in Fig. 5.7 (b). It is evident that the spin wave peak in the experimental spectrum is much lower than that in theory. It should be noted that the calculation are done for the ground state at 0 K, while the experiments are done at 120 K. To estimate the influence of the temperature we extrapolate the MOKE signal of 1 ML Fe film from 120 K to 0 K in according to Ref. [5]. The increase of the magnetic moment is estimated to be about 30%, which is expected to give an enhancement of spin wave energy within the same amount. However, this temperature effect can not explain the large energy discrepancy.

The extremely narrow domain wall width about 0.6±0.2 nm has been reported for 1 ML Fe in the STM study [101]. Accordingly, a very large effective anisotropy is proposed for this system. The Mössbauer spectroscopy also shows a reduction of the magnetic hyperfine field in the interface Fe layer in comparison to the upper Fe layers, which suggest a severe influence of the tungsten substrate [4]. Hence, the reduction of the spin wave energy in 1 ML Fe/W(110) implies a more complicated situation in this system, where the spin dynamics is still not completely understood so far.

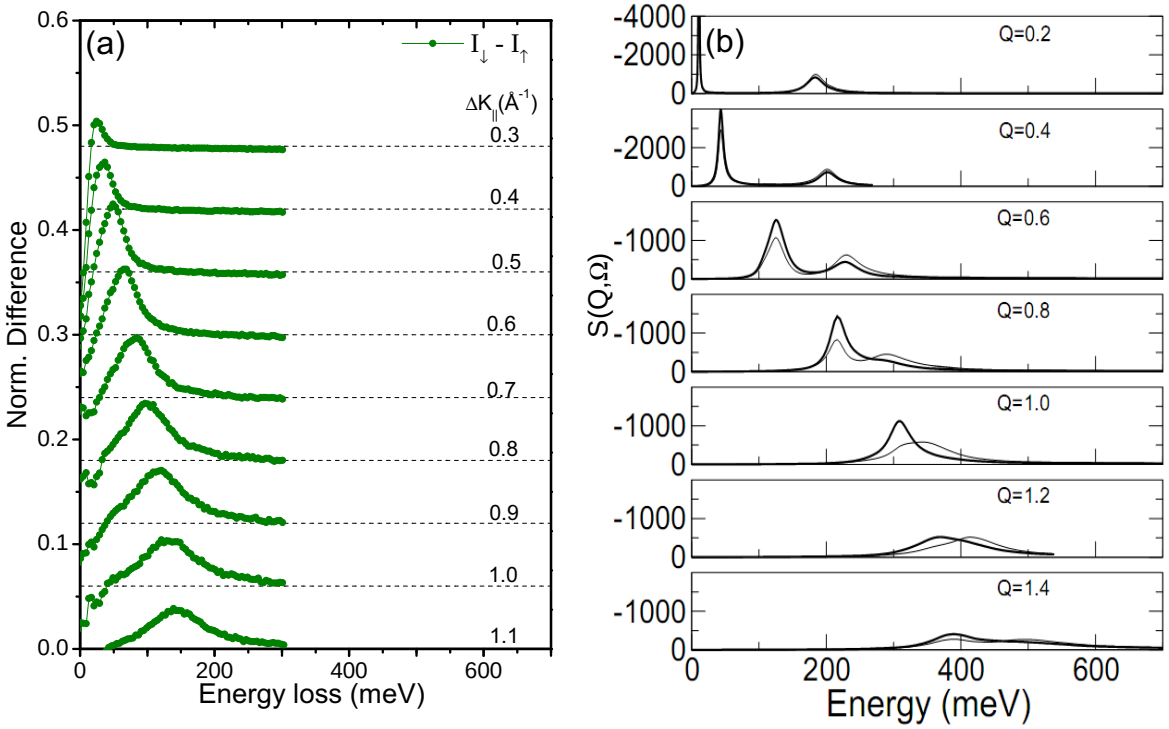

Figure 5.8: The comparison between the difference spectra obtained in the SPEELS measurements and the spectral density functions calculated in Ref. [27] for 2 ML Fe/W(110). (a) shows the experimental difference spectrum (green dots) for $\Delta K_{||}$ from 0.3 Å^{-1} to 1.1 Å^{-1}. To shorten the measuring time and reduce the surface contaminations during the experiments, the energy loss is only scanned up to 300 meV. Nevertheless, measurements with larger energy loss range up to 500 meV had been performed, which show no spin-dependent excitations between 300 meV and 500 meV. (b) The calculated spectral density functions S(Q,Ω) of the spin wave features for the Fe bilayer on W(110) in the surface layer (thick lines) and in the interface layer (thin lines).

5.3.3 SPEEL-spectra of 2 ML Fe/W(110)

Recently, the calculations for the spin waves in 2 ML Fe/W(110) have been performed based on the full itinerant electron theory [26]. Fig. 5.8 (b) shows the spectral density functions for the surface Fe layer (thick lines) and interface one (thin lines) for the wave vectors from 0.2 Å^{-1} to 1.4 Å^{-1}. Two excitation peaks can be clearly distinguished in the spectra for Q $<$ 0.6 Å^{-1}, which merge into a single broad peak for Q $>$ 1.0 Å^{-1}. This is similar to the behavior of the acoustic and optical dispersion curves in the Heisenberg model, which also cross each other at about Q = 1.0 Å^{-1} as shown in Fig. 2.4.

For comparison, the normalized difference spectra are shown in Fig. 5.8 (a). The excitation peaks in the experimental spectra show similar Loretzian shape as the calculated ones in Fig. 5.8 (b). However, only single excitation peak can be observed in the experimental difference spectrum. The energy loss range from 300 meV to 500 meV had been also checked in other SPEELS measurements, which show no spin dependent excitations. The domination of the spin wave excitations can be directly observed in

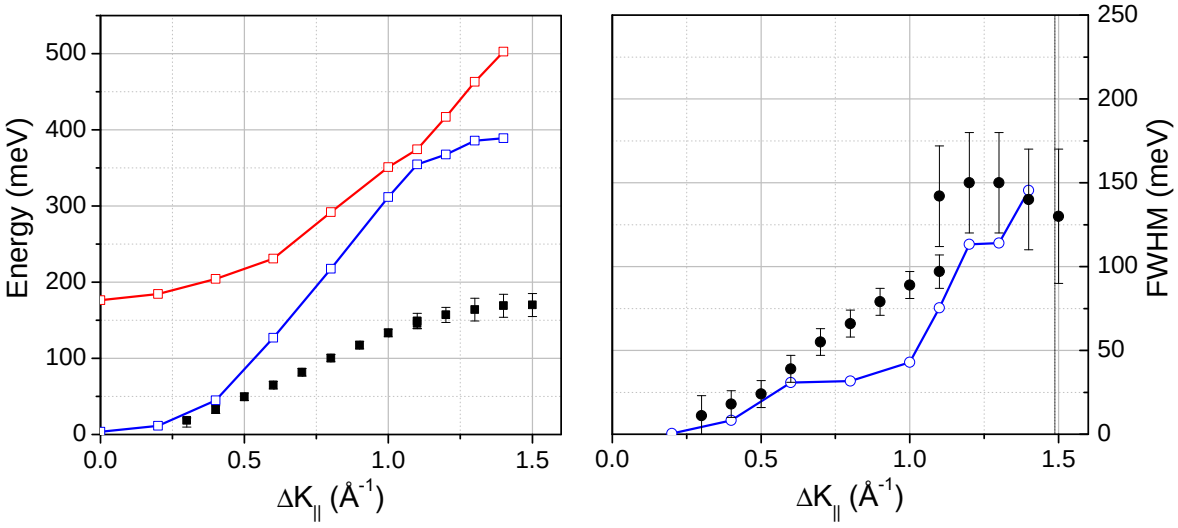

Figure 5.9: The comparison between the SPEELS measurements and the theoretical results [27] for the spin wave dispersion (a) and peak width (b) in 2 ML Fe/W(110). The red and blue squares in (a) show the effective spin wave dispersion relations obtained from the full itinerant electron theory. The black squares are the spin wave dispersion obtained in the SPEELS experiments. In (b), the theoretically generated peak widths (red dots) are compared with the experimental ones (black dots). Good agreement the experimental data and the calculations can be observed in the low wave vector region ($\Delta K_{||} < 0.4$ Å^{-1}).

the $I_{\downarrow}$ and $I_{\uparrow}$ spectra in Fig. 4.2. For the spectra measured for $\Delta K_{||} < 0.7$ Å^{-1}, the intensities in the higher energy loss regions are very low as compared to the pronounced spin wave peaks. This feature demonstrates that the excitation probability of Stoner excitations are very low as compared to the spin wave excitations in the measured energy loss range. It has been mentioned that the spectral density functions calculated in Ref. [27] and Ref. [26] can not account for the Stoner excitations, but can be taken as a good description for the spin wave excitations [27, 37]. Thus, the relatively low Stoner background in the experimental spectra enable the comparison between the experimental and theoretical results.

The peaks in the experimental difference spectra reveal lower energies than those calculated for the same wave vectors. This can be seen from the Fig. 5.9 (a), in which the effective dispersion relations from the calculations are compared with the experimental dispersion curve. The blue and red symbols represent the two peak positions of the low and high modes in the spectral density functions in Fig. 5.8 (b). The calculation gives the exchange stiffness D = 230 meVÅ^2 [26], which is close to the experimental result of about 206 meVÅ^2. Better agreement is expected for the low temperature, considering that the measuring temperature is 300 K, which is already about 66% of the Tc for 2 ML Fe/W(110). However, large discrepancy can be observed in the high wave vector region for Q > 0.5 Å^{-1}. It was pointed out that it is possible to make the large wave vector modes in the calculation closer to the experimental data, while the spin wave stiffness will softens by roughly the same amount [26]. Therefore, a satisfactory agreement of both the exchange stiffness and the large wave vector spin waves can not be obtained

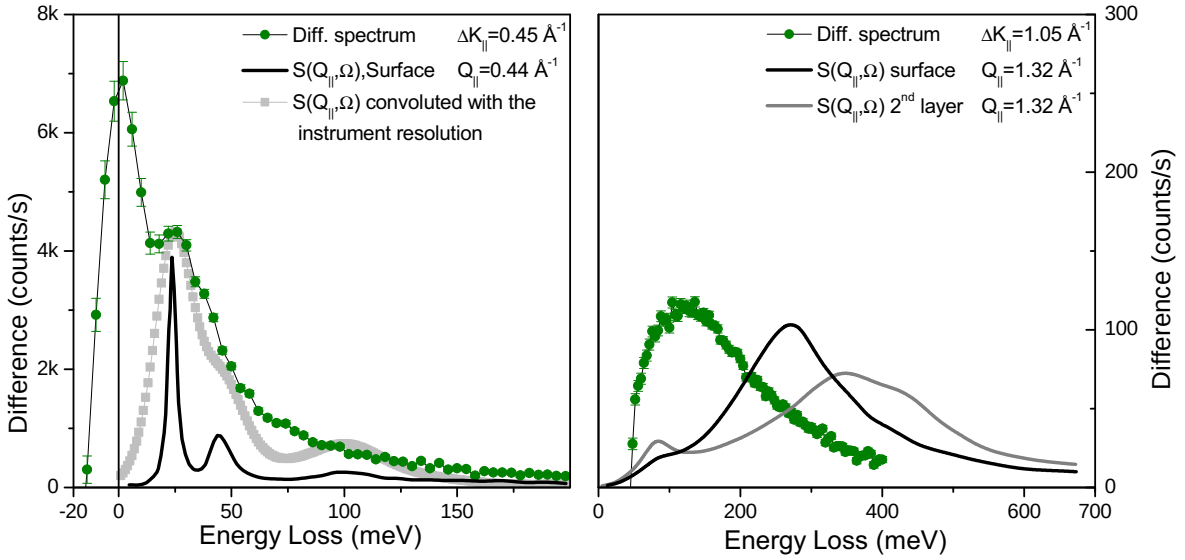

Figure 5.10: The comparison between the difference spectra obtained in the SPEELS measurement and the spectral density functions calculated for 5 ML Fe/W(110) [27]. (a) shows the experimental difference spectrum (green dots) for $\Delta K_{||}$=0.45 Å^{-1}, and the spectral density function (black curve) in the surface layer for $Q_{||}$=0.44 Å^{-1}. The gray curve is the convolution of the density function and the instrumental response function (a Gaussian distribution with FWHM=18 meV), which shows a good agreement with the experimental result. (b) shows the difference spectrum (green dots) for $\Delta K_{||}$=1.05 Å^{-1}, and the spectral density functions in the surface layer (black) and the layer underneath (gray curve) with $Q_{||}$=1.32 Å^{-1} are presented for comparison.

so far [26].

The FWHM of the excitation peaks in the experimental and calculated spectra are compared in Fig. 5.9 (b). Quite good agreement can be observed for Q < 0.6 Å^{-1}. Due to the overlap of the two modes at about Q = 1.0 Å^{-1}, the FWHM of the lower mode in the calculated spectra are difficult to be defined [26]. Large uncertainties also exist in the experimental data for high wave vector data. Therefore, the comparison for large wave vectors is not recommended.

5.3.4 SPEEL-spectra of thicker Fe films

The experimental difference spectra for 5 ML Fe/W(110) with $\Delta K_{||}$ = 0.45 Å^{-1} and 1.05 Å^{-1} are shown in Fig. 5.10 (a) and (b), respectively. For the difference spectrum in Fig. 5.10 (a), the spin wave peak is rising up significantly at the energy loss of about 25 meV. The spectral density function is denoted by the black solid curve below the experimental spectrum. It is taken from the calculation for a 5-layer Fe film on W(110) for the wave vector of 0.44 Å^{-1}, as has been shown in Fig. 2.7 (a). Assuming that the electrons are mainly sensitive to the top most layer, only the spectral density function of the surface layer is taken for comparison [27].

In the spectral density function (Fig. 2.7 (a)), the first mode is found at about 24 meV. The second one shows a lower intensity at 44 meV, and is well separated

from the first mode. The energy of the first mode is consistent with the spin wave energy observed in the experimental spectrum. However, the peak of first mode shows much narrower width than the spin wave peak in the experimental difference spectrum. The broadening of the experimental peak may be due to the convolution with the response function of the SPEEL-spectrometer, whose energy resolution is 18 meV. To see this effect, the spectral density function is convoluted by a Gaussian distribution with FWHM = 18 meV. The resulted curve is scaled and shown in Fig. 5.10 (gray curve). After convolution, the second one becomes the shoulder of the first mode. The shape of the convoluted spectrum agrees very well with the spin wave peak in the experimental difference spectrum[5]. The observation suggests that the asymmetric spin wave peaks may be attributed to the excitation of the high energy spin wave modes. It also agrees with the assumption made at the beginning of this chapter, that the spin wave peak is dominated by the lowest spin wave mode for the low wave vector transfers, and the peak position mainly represents the energy of this lowest mode.

Above discussion shows that the spin wave peaks could be strongly broadened due to the finite energy resolution of the spectrometer. Technically, it is possible to use a higher energy resolution, e.g. 10 meV, to show the details of the multi-peak excitations. However, due to the statistical growth mode of the Fe on W(110), the film of 5 ML actually consists of the regions of the thickness varying from 3 to 7 atomic layers. As has been shown in Fig. 5.6, the variation of the spin wave energy is about 14 meV for these films. It may again blur out the expected multi-peak spectrum.

The experimental results and the theoretical spectra for high wave vector spin wave $Q_{||} = 1.32$ Å^{-1} are shown in Fig. 5.10 (b), in which the spectral density function for the surface layer and the layer beneath are presented (black and gray curves). Because the in-plane wave vector transfer of 1.32 Å^{-1} can not be reached with the incident electron energy of 4 eV, the experimental spectrum of slightly smaller wave vector $\Delta K_{||} = 1.05$ Å^{-1} is chosen for comparison. The spin wave has a maximum at 120 meV. The spin wave with a higher wave vector $\Delta K_{||} = 1.17$ Å^{-1} had been measured in our previous work, which also shows the peak at 120 meV [23]. However, in the spectra density function for the surface layer (black solid curve), the broad peak is centered at a much large energy of 270 meV. A sudden change of the spin wave peak position from 120 meV to 270 meV is unlikely, when $\Delta K_{||}$ increases from 1.05 Å^{-1} to 1.32 Å^{-1}. There is a large difference between the experimental spectrum and the spectral density function for the topmost atomic layer. However, as shown in Fig. 5.10 (b), the spectral density function for the second layer from the surface (marked as s-1 in Fig. 2.7 (b)) shows a clear peak at about 80 meV, which is near to the experimental value. This peak may contribute to the spectrum observed experimentally.

According to the Heisenberg model, the number of the spin wave modes increases with the film thickness. This can be seen from the dispersion curves calculated for the two-layer and twenty-layer slabs in Figs. 2.4 and 2.5. When the number of modes increases, the dispersion curves become denser, and the energies of all the spin wave modes are more close to each other. In the spectral density function, the distinct spin wave peaks can be taken as the eigenmodes in the Heisenberg model, which are broadened by the damping [27, 37]. Thus, the discussion based on the Heisenberg model

[5]The peak at zero energy loss is due to the difference of the elastic peaks in the $I_\uparrow$ and $I_\downarrow$ spectra. It can be described by an additional Gaussian peak, which is not shown here.

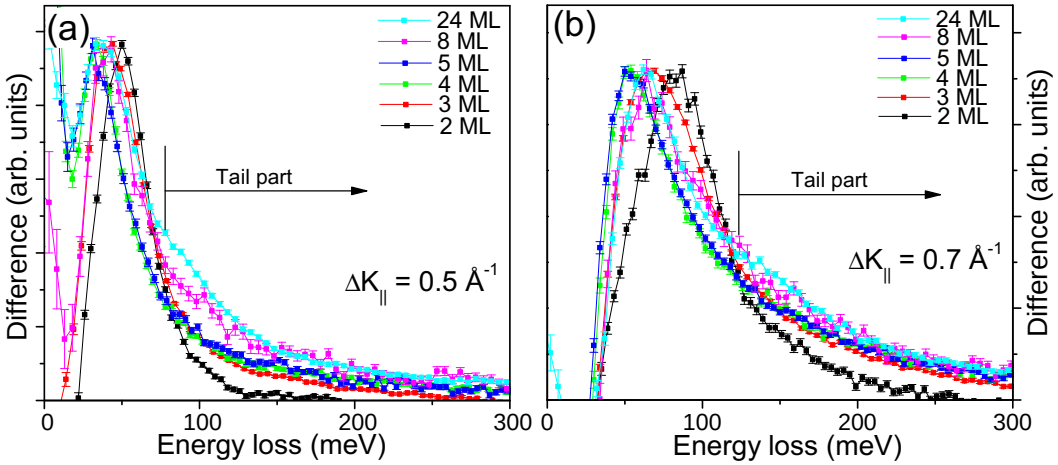

Figure 5.11: Broadening of the spin wave peaks observed for the Fe films of different thicknesses. The difference spectra are taken from Fig. 4.13 for $\Delta K_{||} = 0.5$ Å^{-1} (a) and 0.7 Å^{-1} (b). To compare the weight of the "tail" part, the experimental difference spectra are artificially scaled to have the same maxima of the peaks. The weight of the tail part is enhanced as the film thickness increases, which can be qualitatively explained as the increase of the contribution of the higher energy modes.

can be qualitatively applied for the spin wave peaks in the spectral density functions. For the thicker films, there are more spin wave modes emerging under the foot of the dominant peak of the first mode, and contributing a "tail" to this peak. Therefore, the intensity ratio between the tail part and the first mode will be larger as the film thickness increases.

Fig. 5.11 (a) and (b) show the experimental difference spectra for $\Delta K_{||} = 0.5$ Å^{-1} and 0.7 Å^{-1}, respectively, for the Fe films of the thicknesses from 2 ML to 24 ML. To demonstrate the increase of the "tail" part, the difference spectra are scaled to have their spin wave peak maxima in the same height. In Fig. 5.11, we again see that the energy of spin wave peaks shifts as the film thickness changes, which has been shown in Fig. 5.6 (a). In the energy range of 100∼200 meV in Fig. 5.11 (a), the thicker Fe films show clearly the higher "tail" parts in the spectra. This can be observed in higher energy region marked by "tail" part in Fig. 5.11 (a) and (b). According to the discussion above, the tail parts are attributed to the excitation of the high energy modes. They become more dense in energy for the thicker films, and thus give more contribution to the "tail". Another mechanism responsible for the enhancement of the "tail" part is related to the Stoner excitations. The probability to excite Stoner excitations may become higher for the thicker films. In this case, the theoretical calculations considering both spin wave excitation and Stoner excitation are needed to precisely describe the experimental spectra.

In this section, the experimental results obtained from SPEELS are compared with the theoretical calculations based on the itinerant electron theory. In general, the broad features of the spin wave peaks observed in the SPEELS experiments agree with the theoretical prediction [27, 28, 37, 50, 52]. A non-monotonic thickness dependence for the spin wave stiffness D is observed for the Fe thin films on W(110), which is in good

agreement with the theoretical calculations. This also indicates that the theory can give a good description for the energy of the spin waves with low wave vectors. For 5 ML Fe/W(110), the spin wave profile in the experimental difference spectrum can be well described by the spectral density function with the energy resolution of the spectrometer. Base on this observation, the asymmetric spin wave peaks observed for thick Fe films may be resulted from the excitations of the high energy spin wave modes. All above observations demonstrate that the capability of the calculations for spin waves based on the itinerant electron theory. However, for large wave vectors, the energies of the spin wave peaks predicted by the theory are all higher than the experimental results. Larger discrepancy can be observed for the Fe thin films on W(110).

Chapter 6

Conclusions and outlook

Using the spin-polarized electron energy loss spectroscopy, we have studied the high wave vector spin waves in the ultra thin Fe films on W(110). The clear dispersion relation of the spin waves in 2 ML Fe/W(110) is observed. The SPEELS studies of the Fe films thinner than 2 ML reveal that the spin waves originate mainly from the double layer regions. The measured dispersion can be described by the next nearest neighbor Heisenberg model up to the Brillouin zone boundary. The derived exchange stiffness A is in good agreement with the results obtained from the domain wall width analysis [12, 13]. The broadening of the spin wave peaks in the spectra implies that spin waves are strongly confined in the double layer Fe islands. The lifetime of the high wave vector spin waves in the 2 ML Fe film is shorter than 50 fs. For the wave vector 0.6 $Å^{-1}$, the spatial distribution does not exceed a few nanometers.

Magnetic excitations with the energy changing from 20 meV to 60 meV are observed in 1 ML Fe/W(110) at low temperature, which also show the dispersion behavior. The observation shows that the spin waves are severely damped. The low energy and relatively broad peaks may be due to the strong influence of the substrate.

In comparison to our previous studies of 5 ML Fe/W(110), this work reveals more details of the spin wave excitations in the low energy loss region. The thickness dependence of the spin wave stiffness changes non-monotonically with respect to film thickness, which agrees very well with the theoretical calculations based on the itinerant electron theory [28]. The experimental spectrum for the low wave vector transfer can be well described by the spectral density function [27]. The asymmetric spin wave peak may be attributed to the excitation of the higher energy mode spin waves.

In this work, we have successfully observed the spin wave excitations in the Fe films on W(110), and showed how the properties of the spin waves change with the film thickness. However, there are still open questions of great interest. A explanation for the large discrepancy observed for 1 ML Fe/W(110) between the experimental data and the theory is still needed. It is also interesting to have the comparison between the SPEEL-spectra and spectral density functions for the state close to the Brillouin zone boundary.

For 1 ML and 2 ML Fe/W(110), it is worthy to explore for the spin wave dispersion in the $[1\bar{1}0]$ direction, along which the exchange stiffness is expected to be four times higher than that along [001] [28]. As a different system, the SPEELS study of the Fe(001) surface is important as a comparison of present work. A softer spin wave dispersion

is expected for this system, because of lower number of the nearest neighbors at the surface.

Bibliography

[1] M. Plihal, D. L. Mills, and J. Kirschner, Phys. Rev. Lett. **82**, 2579 (1999).

[2] R. Vollmer, M. Etzkorn, P. S. Anil Kumar, H. Ibach, and J. Kirschner, Phys. Rev. Lett. **82**, 147201 (2003).

[3] M. Przybylski and U. Gradmann, Phys. Rev. Lett. **57**, 1152 (1987).

[4] M. Przybylski, I. Kaufmann, and U. Gradmann, Phys. Rev. B **40**, 8631 (1989).

[5] H. J. Elmers, G. Liu, and U. Gradmann, Phys. Rev. Lett. **63**, 566 (1989).

[6] B. Hillebrands, P. Baumgart, and G. Güntherodt, Phys. Rev. B **36**, 2450 (1987).

[7] H. J. Elmers, J. Hauschild, H. Höche, U. Gradmann, B. H, D. Heuer, and U. Köhler, Phys. Rev. Lett. **73**, 898 (1994).

[8] H. J. Elmers, J. Hauschild, H. Fritzsche, G. Liu, and U. Gradmann, Phys. Rev. Lett. **75**, 2031 (1995).

[9] H. Bethge, D. Heuer, C. Jensen, K. Reshöft, and U. Köhler, Surf. Sci. **331-333**, 878 (1995).

[10] C. Jensen, K. Reshöft, and U. Köhler, Appl. Phys. A **62**, 217 (1996).

[11] O. Pietzsch, A. Kubetzka, M. Bode, and R. Wiesendanger, Phys. Rev. Lett. **84**, 5212 (2000).

[12] A. Kubetzka, O. Pietzsch, M. Bode, and R. Wiesendanger, Phys. Rev. B **63**, 147407 (2001).

[13] A. Kubetzka, O. Pietzsch, M. Bode, and R. Wiesendanger, Phys. Rev. B **67**, 020401 (2003).

[14] M. Bode, K. von Bergmann, O. Pietzsch, A. Kubetzka, and R. Wiesendanger, J. Magn. Magn. Mater. **304**, 1 (2006).

[15] K. von Bergmann, M. Bode, and R. Wiesendanger, J. Magn. Magn. Mater. **305**, 279 (2006).

[16] D. Sander, R. Skomski, C. Schmidthals, A. Enders, and J. Kirschner, Phys. Rev. Lett. **77**, 2566 (1996).

[17] D. Sander, A. Enders, and J. Kirschner, Europhys. Lett. **45(2)**, 208 (1999).

[18] H. L. Meyerheim, D. Sander, R. Popescu, J. Kirschner, P. Steadman, and S. Ferrer, Phys. Rev. B **64**, 045414 (2001).

[19] R. Popescu, H. L. Meyerheim, D. Sander, J. Kirschner, P. Steadman, O. Robach, and S. Ferrer, Phys. Rev. B **68**, 155421 (2003).

[20] J. Schäfer, D. Schrupp, E. Rotenberg, K. Rossnagel, H. Koh, P. Blaha, and R. Claessen, Phys. Rev. Lett. **92**, 097205 (2004).

[21] J. Schäfer, M. Hoinkis, E. Rotenberg, P. Blaha, and R. Claessen, Phys. Rev. B **72**, 155115 (2005).

[22] J. Schäfer, M. Hoinkis, E. Rotenberg, P. Blaha, and R. Claessen, Phys. Rev. B **75**, 092401 (2007).

[23] R. Vollmer, M. Etzkorn, P. S. Anil Kumar, H. Ibach, and J. Kirschner, J. Magn. Magn. Mater. **272-276**, 2126 (2004).

[24] R. Vollmer, M. Etzkorn, P. S. Anil Kumar, H. Ibach, and J. Kirschner, Thin Solid Films **464-465**, 42 (2004).

[25] W. X. Tang, Y. Zhang, I. Tudosa, J. Prokop, M. Etzkorn, and J. Kirschner, Phys. Rev. Lett. **99**, 087202 (2007).

[26] R. B. Muniz, A. T. Costa, and D. L. Mills, Proc. of the 6th IEEE symp. on Metallic Multilayers 2007, in press (2007).

[27] A. T. Costa, R. B. Muniz, and D. L. Mills, Phys. Rev. B **68**, 224435 (2003).

[28] R. B. Muniz, A. T. Costa, and D. L. Mills, J. Phys.: Condens. Matter **15**, S495 (2003).

[29] R. B. Muniz and D. L. Mills, Phys. Rev. B **66**, 174417 (2003).

[30] M. Shimizu, Rep. Prog. Phys. **44**, 329 (1981).

[31] C. Kittel, *Introduction to Solid State Physics, seventh edition*, John Wiley and Sons Inc., New York Chichester Brisbane Toronto Singapore, 1996.

[32] J. R. Dutcher, Linerar and nonlinear spin waves in Magnetic films and superlattices, page Chap. 6, World Scientific, Singapore New Jersey London Hong Kong, 1994.

[33] D. Sander, J. Phys.: Condens. Matter **16**, R603 (2004).

[34] J. Stöhr, *Magnetism, From Fundamentals to Nanoscale Dynamics*, Springer series in solid-state sciences 152, Springer Verlag, Berlin Heidelberg, 2006.

[35] M. Pajda, J. Kudrnovský, I. Turek, V. Drchal, and P. Bruno, Phys. Rev. B **64**, 174402 (2001).

[36] F. Keffer, H. Kaplan, and Y. Yafet, American Journal of Physics **21**, 250 (1953).

[37] A. T. Costa, R. B. Muniz, and D. L. Mills, Phys. Rev. B **70**, 054406 (2004).

[38] H. Hopster, R. Raue, and R. Clauberg, Phys. Rev. Lett. **53**, 695 (1984).

[39] J. Kirschner, Phys. Rev. Lett. **55**, 973 (1985).

[40] D. Venus and J. Kirschner, Phys. Rev. B **37**, 2199 (1988).

[41] J. Kirschner, D. Rebenstroff, and H. Ibach, Phys. Rev. Lett. **53**, 698 (1984).

[42] J. C. Slater, Phys. Rev. **52**, 198 (1937).

[43] C. Herring and C. Kittel, Phys. Rev. **81**, 869 (1951).

[44] C. Herring, Phys. Rev. **87**, 60 (1952).

[45] C. Herring, in *Exchange interactions among itinerant electrons*, edited by G. T. Rado and H. Suhl, page Vol. IV of Magnetism, Academic Press, New York London, 1966.

[46] L. Udvardi, L. Szunyogh, K. Palotás, and P. Weinberger, Phys. Rev. B **68**, 104436 (2003).

[47] J. F. Cooke, J. W. Lynn, and H. L. Davis, Phys. Rev. B **21**, 4118 (1980).

[48] M. Plihal and D. L. Mills, Phys. Rev. B **58**, 14407 (1998).

[49] H. Tang, M. Plihal, and D. L. Mills, J. Magn. Magn. Mater. **187**, 23 (1998).

[50] A. T. Costa, R. B. Muniz, and D. L. Mills, Phys. Rev. B **69**, 064413 (2004).

[51] A. T. Costa, R. B. Muniz, and D. L. Mills, Phys. Rev. B **74**, 214403 (2006).

[52] A. T. Costa, R. B. Muniz, and D. L. Mills, Phys. Rev. B **73**, 054426 (2006).

[53] J. A. Blackman, T. Morgan, and J. F. Cooke, Phys. Rev. Lett. **55**, 2814 (1985).

[54] H. A. Mook and R. M. Nicklow, Phys. Rev. B **7**, 336 (1973).

[55] D. McKenzie Paul, P. W. Mitchell, H. A. Mook, and U. Steinberger, Phys. Rev. B **38**, 580 (1988).

[56] T. Balashov, A. F. Takács, W. Wulfhekel, and J. Kirschner, Phys. Rev. Lett. **97**, 187201 (2006).

[57] S. Demokritov, B. Hillebrands, and A. Slavin, Phys. Rep. **348**, 441 (2001).

[58] B. Heinrich and J. A. C. Bland, *Ultrathin Magnetic Structures II*, Springer Verlag, Berlin Heidelberg New York, 1994.

[59] R. E. Camley, T. S. Rahman, and D. L. Mills, Phys. Rev. B **23**, 1226 (1981).

[60] M. Farle, Rep. Prog. Phys. **61**, 755 (1998).

[61] G. Shirane, R. Nathans, H. A. Steinsvoll, O. andAlperin, and S. J. Pickart, Phys. Rev. Lett. **15**, 146 (1965).

[62] J. W. Lynn, Phys. Rev. B **11**, 2624 (1975).

[63] J. P. Wicksted, P. Böni, and G. Shirane, Phys. Rev. B **30**, 3655 (1984).

[64] T. G. Perring, A. T. Boothroyd, D. McK. Paul, A. D. Taylor, R. Osborn, R. J. Newport, J. A. Blackman, and H. A. Mook, J. Appl. Phys. **69**, 1895 (1991).

[65] M. Yethiraj, R. A. Robinson, D. S. Sivia, J. W. Lynn, and H. A. Mook, Phys. Rev. B **43**, 2565 (1991).

[66] C. K. Loong, J. M. Carpenter, J. W. Lynn, R. A. Robinson, and H. A. Mook, J. Appl. Phys. **55**, 6219 (1984).

[67] H. Ibach, D. Bruchmann, R. Vollmer, M. Etzkorn, P. S. Anil Kumar, and J. Kirschner, Rev. Sci. Instrum. **74**, 4089 (2003).

[68] R. Vollmer, M. Etzkorn, P. S. Anil Kumar, H. Ibach, and J. Kirschner, J. App. Phys. **95**, 7435 (2004).

[69] M. Etzkorn, P. S. Anil Kumar, R. Vollmer, and J. Kirschner, Surf. Sci. **566-568**, 241 (2004).

[70] M. Etzkorn, P. S. Anil Kumar, W. X. Tang, Y. Zhang, and J. Kirschner, Phys. Rev. B **72**, 184420 (2005).

[71] M. Etzkorn, *Spin waves with high energy and momentum in ultrathin Co-films studied by spin-polarized electron energy loss spectroscopy*, Dissertation.

[72] M. R. Vernoy and H. Hopster, Phys. Rev. B **68**, 132403 (2003).

[73] A. Zangwill, *Physics at Surface*, Cambridge University Press, 1988.

[74] D. P. Pappas, K. P. Kämper, B. P. Miller, H. Hopster, D. E. Fowler, C. R. Brundle, A. C. Luntz, and Z. X. Shen, Phys. Rev. Lett. **66**, 504 (1991).

[75] M. Getzlaff, J. Bansmann, J. Braun, and G. Schönhense, Z. Phys. B **104**, 11 (1997).

[76] H. Hopster, Journal of Electron Spectroscopy and Related Phenomena **98-99**, 17 (1999).

[77] H. Ibach and D. L. Mills, *Electron energy loss spectroscopy and surface vibrations*, Academic Press, New York London Paris, 1982.

[78] R. Feder, *Polarised electrons in surface physics*, World Scientific, Singapore, 1985.

[79] J. Kessler, Polarized Electrons, in *Springer series on Atoms and Plasmas, secound edition*, edited by G. Ecker, P. Lambropoulos, and H. Walther, Springer Verlag, Berlin Heidelberg New York Tokyo, 1985.

[80] R. Feder and J. Kirschner, Surf. Sci. **103**, 75 (1981).

[81] M. Plihal, D. L. Mills, H. J. Elmers, and U. Gradmann, Phys. Rev. B **51**, 8193 (1995).

[82] D. Venus, S. Cool, and M. Plihal, Surf. Sci. **446**, 199 (2000).

[83] A. M. Baró and W. Erley, Surf. Sci. **112**, L759 (1981).

[84] D. L. Mills, Phys. Rev. B **34**, 6099 (1986).

[85] U. Gradmann and G. Waller, Surf. Sci. **116**, 539 (1982).

[86] W. Weber, A. Bischof, R. Allenspach, C. H. Back, J. Fassbender, U. May, B. Schirmer, R. M. Jungblut, G. Güntherodt, and B. Hillebrands, Phys. Rev. B **54**, 4075 (1996).

[87] J. Hauschild, U. Gradmann, and H. J. Elmers, App. Phys. Lett. **72**, 3211 (1998).

[88] T. Dürkop, H. J. Elmers, and U. Gradmann, J. Magn. Magn. Mater. **172**, L1 (1997).

[89] K. Wagner, N. Weber, H. J. Elmers, and U. Gradmann, J. Magn. Magn. Mater. **167**, 21 (1997).

[90] I. G. Baek, H. G. Lee, H. J. Kin, and E. Vescovo, Phys. Rev. B **67**, 075401 (2003).

[91] C. H. Back, C. Würsch, A. Vaterlaus, U. Rumsperger, U. Maler, and D. Pescia, Nature **378**, 597 (1995).

[92] M. J. Dunlavy and D. Venus, Phys. Rev. B **69**, 094411 (2004).

[93] B. A. Joyce, P. J. Dobson, J. H. Neave, K. Woodbridge, J. Zhang, P. K. Larsen, and B. Bôlger, Phys. Rep. **348**, 441 (2001).

[94] N. Weber, K. Wagner, H. J. Elmers, J. Hauschild, and U. Gradmann, Phys. Rev. B **55**, 14121 (1997).

[95] J. Hong and D. L. Mills, Phys. Rev. B **59**, 13840 (1999).

[96] X. Tao, D. P. Landau, T. C. Schulthess, and G. M. Stocks, Phys. Rev. Lett. **95**, 087207 (2005).

[97] T. Andersen and W. Hübner, Phys. Rev. B **74**, 184415 (2006).

[98] X. Qian and W. Hübner, Phys. Rev. B **60**, 16192 (1999).

[99] A. Kubetzka, M. Bode, O. Pietzsch, and R. Wiesendanger, Phys. Rev. Lett. **88**, 057201 (2002).

[100] E. Y. Vedmedenko, A. Kubetzka, K. von Bergmann, O. Pietzsch, M. Bode, J. Kirschner, H. P. Oepen, and R. Wiesendanger, Phys. Rev. Lett. **92**, 077207 (2004).

[101] M. Pratzer and H. J. Elmers, Phys. Rev. Lett. **87**, 127201 (2001).

[102] M. Pratzer and H. J. Elmers, Phys. Rev. B **67**, 094416 (2003).

Acknowledgment

I would like to express my deepest gratitude to my supervisor, Prof. Dr. Jürgen Kirschner for his continuous guidance and support throughout this work.

Many thanks go to Dr. WenXin Tang for his guidance in the starting of my experimental work, and the pleasant collaboration.

I wish my appreciate to Dr. Jacek Prokop for the helpful suggestions, discussions and the warm encourage during this work.

Thanks also go to Dr. Ioan Tudosa for the pleasant collaboration and the stimulated discussions.

I would like to thank Dr. Markus Etzkorn for his warm help in the starting of my study.

I also thank Prof. Dr. P. S. Anil Kumar for very helpful discussions on the SPEELS experiments.

I would like to thank P. Buczek, Dr. C. L. Gao, S. Wedekind and A. Tange for the discussions on physics and the help in experiments. My thanks also go to Dr. J. Henk, Dr. D. Sander, Dr. L. Sandratskii, Dr. A. Winkelman, Dr. G. Rodary, Dr. F. Schumann, Prof. Dr. W. Wulfhekel and Prof. Dr. H. J. Elmers, Prof. Dr. X. F. Jin, Prof. Dr. H. F. Ding, Prof. Dr. Y. Z. Wu for the fruitful discussions, and helpful suggestions.

My thanks go to Mr. H. Engelhard, Mrs. H. Menge, F. Helbig, the mechanical and electrical workshop for the high quality professional technique support.

I would like to thank my mentor Dr. A. Heilmann and Dr. N. Pinna for the helpful advices on my study. I also thank all the members in the International Max Planck Research School, who let me learn a lot in various scientific fields. My special thank go to our coordinator, Dr. M. Kaempfe for her warm help during my study in IMPRS.

I wish my **herzliches Dankeschön** to the colleagues in the administration, Ms. M. Witzig, Ms. B. Frankenstein, and Mr. D. Hoehl for the warm help in the last stage of this work.

I appreciate all MPI colleagues for the good and friendly working atmosphere. I feel lucky to be a member in this institute.

My deep thanks finally go to my parents and my wife Zhen Tian.

Eidesstattliche Erklärung

Ich erkläre hiermit, dass ich keine anderen als die von mir angegebenen Quellen und Hilfsmittel zur Erstellung meiner Dissertation verwendet habe. Den benutzten Werken wörtlich oder inhaltlich entnommene Stellen sind als solche gekennzeichnet.

Yu Zhang

Halle (Saale), February 2009

Curriculum vitae

First Name	Yu
Family Name	Zhang
Date of Birth	November 14, 1977
Place of Birth	Hebei, China
Nationality	P. R. China
E-mail	zhangyu@mpi-halle.de

EDUCATION

Sep. 1996 - Jul. 2000	Tsinghua University (Beijing, China) Department of Environmental Science and Engineering Bachelor of Engineering
Sep. 2001 - Jan. 2003	Tsinghua University (Beijing, China) Department of Environmental Science and Engineering Master of Engineering
Jan. 2003 - Jul. 2004	Palmer and Turner Consultants Ltd. (Shanghai, China) Assistant Engineer
Since Sept. 2004	Max-Planck Institute of Microstructure Physics and Martin-Luther-Universität Halle-Wittenberg Ph. D. candidate (Supervisor: Prof. Jürgen Kirschner)

Yu Zhang

Halle (Saale), February 2009